

## MASTER

### Thermal performance of an Evacuated Tube Collector during dynamic conditions of a Direct Multi-Pass Solar System

van Delft, P.

*Award date:*  
2021

[Link to publication](#)

#### **Disclaimer**

This document contains a student thesis (bachelor's or master's), as authored by a student at Eindhoven University of Technology. Student theses are made available in the TU/e repository upon obtaining the required degree. The grade received is not published on the document as presented in the repository. The required complexity or quality of research of student theses may vary by program, and the required minimum study period may vary in duration.

#### **General rights**

Copyright and moral rights for the publications made accessible in the public portal are retained by the authors and/or other copyright owners and it is a condition of accessing publications that users recognise and abide by the legal requirements associated with these rights.

- Users may download and print one copy of any publication from the public portal for the purpose of private study or research.
- You may not further distribute the material or use it for any profit-making activity or commercial gain



Department of Mechanical Engineering  
Research Group Energy Technology

Master Thesis

# Thermal performance of an Evacuated Tube Collector during dynamic conditions of a Direct Multi-Pass Solar System

*Experimental research*

Pim van Delft  
ID: 0819192

Thesis supervisor TU/e:  
Dr. ir. Camilo C.M. Rindt

Supervisor Conico Valves B.V.:  
Ir. Nico van Ruth

Eindhoven, Wednesday 3<sup>rd</sup> March, 2021



# Abstract

This research focuses on designing, building and commissioning of a new experimental set-up to conduct experimental research into the dynamic behaviour of the multi-pass mode of the DMP Solar System. In this system a Thermo-Differential Valve is included, which is developed by Conico Valves B.V.

The new experimental set-up has been commissioned successfully and is able to capture the dynamic behaviour of the multi-pass mode and complies with the requirements of ISO 9806:2017.

After the experimental set-up has been built, experiments were conducted to determine the thermal- and optical efficiency of an evacuated tube collector during single- and multi-pass mode. Also the total thermal efficiency of the entire system is evaluated for single- and multi-pass mode.

Furthermore a theoretical model is developed to give more insight in the switching behaviour of the Thermo-Differential Valve.



# Foreword

Because of my good experience with experimental set-ups during my internship, I was looking for a graduation project that included the designing, building, and analyzing of an experimental set up. Ideally, I would like to work on a project that concerned sustainability, which is my other great interest. With help from my supervisor, Camilo van Rindt (TU/e), I found this specific opportunity at the company Conico Valves B.V., with whom I collaborated for this master thesis project. I am grateful for this opportunity and experience.

During my Thesis, I received great help and support from many people. I would especially like to thank the following people. First of all, I would like to thank Martin Huijzer for his help with programming in Labview and for practical information regarding measurement equipment. For experience with thermocouple calibration on the other hand, I have had some great support from Theo de Groot. I also have to thank him for help with design of the electrical control cabinet. ( I have never seen a more neat electrical cabinet before).

Furthermore, I would like to give a huge thank you to Henri Vliegen for always being ready with endless help and a ton of practical knowledge! I am grateful for the help with all the components that needed to be machined in the workshop and also for your support in ordering all 800 components. Highlight was the blockade to ensure that the lab door remained closed (see figure 1) in order to maintain a steady ambient temperature. Even in times of Corona, he was ready to help you every moment of the day wherever he could.

I would also like to thank my supervisor Camilo Rindt for guiding the project/guiding me during this project. Camilo supported me a lot, gave me a lot of helpful feedback and is always thinking in possibilities.

I am also thankful for the collaboration with Nico van Ruth. He helped me with important design choices and shared his experience about solar collector systems and test methods which really supported my project.

Finally, I would like to thank Eva van Hattum (my girlfriend), for supporting me through this entire process.

Thank you all,

Pim



Figure 1: Blockage created by Henri in order to keep the door closed.

# Contents

<b>Contents</b>	<b>v</b>
<b>1 Introduction</b>	<b>2</b>
1.1 Direct Multi-Pass Solar system . . . . .	2
1.1.1 Operation modes of the DMP Solar system . . . . .	3
1.2 Problem definition & research question . . . . .	3
1.3 Research Plan and Project Objectives . . . . .	6
1.3.1 New experimental set-up . . . . .	6
1.3.2 Experimental Research . . . . .	6
<b>2 Solar Collector Test Methods</b>	<b>8</b>
2.1 Evacuated Tube Collector with heatpipe . . . . .	8
2.2 Steady State Test Method . . . . .	9
2.2.1 Drying-out heat pipes . . . . .	11
2.3 Dynamic Test Method . . . . .	11
2.3.1 Quasi-dynamic test method . . . . .	11
2.3.2 Dynamic test method . . . . .	11
2.4 Test Method DMP Solar System . . . . .	12
<b>3 Experimental set-up</b>	<b>14</b>
3.1 Design requirements . . . . .	14
3.2 Original Experimental Set-up . . . . .	15
3.2.1 Piping and Instrument diagram . . . . .	15
3.2.2 Solar simulator . . . . .	16
3.2.3 Sensors original set-up . . . . .	16
3.2.4 Dimensions evacuated tube collector . . . . .	17
3.2.5 Additions to original set-up . . . . .	17
3.3 Design Experimental Set-up . . . . .	18
3.3.1 Design storage tank . . . . .	18
3.3.2 Thermo-Differential Valve . . . . .	21
3.3.3 Design Solar Circuit . . . . .	22
3.3.4 Design Cooling Circuit . . . . .	23
3.3.5 Layout of the set-up . . . . .	24
3.4 Measurement Equipment new set-up . . . . .	26
3.4.1 Thermocouples . . . . .	26
3.4.2 Flowmeters . . . . .	26
3.4.3 Instrument Control and Data Acquisition . . . . .	28
3.5 Stability Testing Process Parameters . . . . .	28
3.6 Calibration . . . . .	30
3.6.1 Calibration thermocouples new set-up . . . . .	30
3.6.2 Calibration remaining sensors . . . . .	31
3.7 Uncertainty Measuring Equipment . . . . .	32
3.7.1 Pyranometer . . . . .	32
3.7.2 Flowmeters . . . . .	33
3.7.3 Thermocouples . . . . .	34
3.7.4 Temperature difference . . . . .	35
3.7.5 Comparison with ISO 9806 . . . . .	35

<b>4</b>	<b>Experimental Research</b>	<b>36</b>
4.1	Multi-pass . . . . .	36
4.1.1	Method . . . . .	36
4.1.2	Measuring procedure . . . . .	39
4.1.3	Results Process Temperatures . . . . .	40
4.1.4	Thermal Efficiency Total System . . . . .	43
4.1.5	Optical Efficiency Collector . . . . .	44
4.1.6	Uncertainty Analysis Optical Efficiency . . . . .	47
4.1.7	Results temperature distribution in evacuated tubes . . . . .	49
4.2	Single-pass . . . . .	50
4.2.1	Method . . . . .	50
4.2.2	Measuring procedure . . . . .	50
4.2.3	Additional experiment temperature distribution in evacuated tubes . . . . .	52
4.2.4	Results Optical efficiency . . . . .	52
4.2.5	Uncertainty analysis . . . . .	53
4.2.6	Results temperature distribution in evacuated tubes . . . . .	53
4.3	Single-Pass vs Multi-Pass . . . . .	56
4.3.1	Thermal efficiency of the total system . . . . .	56
4.3.2	Optical Efficiency . . . . .	57
4.3.3	Temperature distribution in evacuated tubes . . . . .	58
<b>5</b>	<b>Thermo-Differential Valve</b>	<b>59</b>
5.1	Thermo Differential Valve . . . . .	59
5.1.1	Switching moment . . . . .	59
5.1.2	Switching time . . . . .	60
5.2	Experimental results . . . . .	66
<b>6</b>	<b>Conclusions and Recommendations</b>	<b>68</b>
6.1	Conclusions . . . . .	68
6.2	Recommendations for future research . . . . .	69
	<b>Appendix</b>	<b>70</b>
<b>A</b>	<b>Additional Literature Review</b>	<b>71</b>
A.1	Additional literature review regarding steady-state testing . . . . .	71
A.2	Additional literature review Quasi-dynamic test method . . . . .	72
A.3	Dynamic test method . . . . .	73
A.3.1	Dynamic test method: one-node approach . . . . .	73
A.3.2	Dynamic test method: multi-node approach . . . . .	74
<b>B</b>	<b>Additional Results</b>	<b>77</b>
B.1	Additional Results Multi-Pass Mode . . . . .	77
B.2	Results Process Parameters . . . . .	79
B.3	Thermal efficiency collector . . . . .	80
<b>C</b>	<b>TRNSYS Output</b>	<b>83</b>
<b>D</b>	<b>Calibration Results</b>	<b>85</b>
<b>E</b>	<b>Uncertainty analysis</b>	<b>88</b>
E.1	Type A uncertainty (Random error) . . . . .	88
E.2	Type B uncertainty (Systematic error) . . . . .	88
E.3	Combined standard uncertainty of measured values . . . . .	89
E.4	Error propagation . . . . .	89
E.5	Expanded uncertainty . . . . .	89

---

E.6	Standard combined uncertainty of derived quantities . . . . .	90
E.6.1	Fluid properties . . . . .	90
E.6.2	Massflow . . . . .	90
E.6.3	Aperture area . . . . .	90
E.6.4	Thermal efficiency collector . . . . .	90
E.6.5	Ambient temperature . . . . .	90
E.6.6	Mean temperature . . . . .	91
E.6.7	Reduced temperature . . . . .	91
E.6.8	Optical efficiency . . . . .	91
<b>F</b>	<b>Solar Keymark Certificate</b>	<b>92</b>
<b>G</b>	<b>Heat Exchanger Performance</b>	<b>95</b>
<b>H</b>	<b>Mechanical Construction Details</b>	<b>101</b>
<b>I</b>	<b>Additions to original set-up</b>	<b>110</b>
I.1	Extra by-pass line to determine thermal effective capacity . . . . .	110
I.2	Connection with original set-up . . . . .	111
<b>J</b>	<b>Instrumentation specifications</b>	<b>112</b>
J.1	Specifications OPTIFLUX 4100 - DN6 . . . . .	112
J.2	Calibration Certificate Pyranometer . . . . .	113
J.3	Pump Curve . . . . .	114
<b>K</b>	<b>Difficulties experimental set-up</b>	<b>115</b>
K.1	Thermal efficiency vs. reduced temperature Multi-pass mode (Not Correct) . . . . .	115
K.2	End of lifetime lamps solar simulator . . . . .	117
<b>L</b>	<b>Data Acquisition with LabVIEW</b>	<b>118</b>
<b>M</b>	<b>Bill of Materials</b>	<b>119</b>

# Nomenclature

Symbol	Description	Unit
$\alpha_x$	The specified accuracy	-
$\alpha_i$	The convective heat transfer coefficient in the tube side	W/m <sup>2</sup> K
$\alpha_o$	The convective heat transfer coefficient at the tank side	W/m <sup>2</sup> K
$\Delta T$	Temperature difference	°C
$\Delta h$	Switching height TDV	m
$\Delta T_{TDV,min}$	Minimum temperature difference TDV	°C
$\Delta t_{cycle}$	Total cycle time	s
$\Delta t_{charging}$	Total charging time	s
$\delta$	The tube thickness	m
$\eta_0$	Optical efficiency	-
$\eta$	Instantaneous thermal efficiency	-
$\eta_{th}$	Thermal efficiency	-
$\lambda$	Conduction coefficient	W/mK
$\rho$	Density	kg/m <sup>3</sup>
$\rho_2$	Density at the temperature of the tank T2	kg/m <sup>3</sup>
$\rho_w$	Density of the water in the tank	kg/m <sup>3</sup>
$\tau_i$	Timeconstant of the integrator action	min
$\tau_d$	Derivative of the derivative action	min
$a_1$	Linear heat loss coefficient collector	
$a_2$	Quadratic heat loss term collector	
$A_a$	Aperture area	m <sup>2</sup>
$A$	Area	m <sup>2</sup>
$A_c$	Cross sectional area	m <sup>2</sup>
$c_p$	Specific heat	J/kgK
$C$	Effective thermal capacity of the collector	J/K
$c$	Specific heat capacity	J/kgK
$c$	Centre point of the housing of the TDV	-
$D_i$	Internal diameter	m
$E$	Total energy gain	J
$F'$	Collector efficiency factor	
$F_R$	Heat removal factor [-]	
$F_{b,float}$	Buoyancy force experienced by the float	N
$F_{b,tube}$	Buoyancy force experienced by the tube	N
$F_m$	Gravitational forces	N
$f_l$	Friction factor for laminar flow	-
$f_t$	Friction factor for turbulent flow	-
$f_{trans}$	Friction factor for transitional flow	-

Symbol	Description	Unit
f	Centre point of the float	-
G	Solar irradiance	W/m <sup>2</sup>
g	Gravitational constant	m/s <sup>2</sup>
H	Height of the coil	m
$K_c$	Gain	
$K_{vs}$	Flow coefficient	m <sup>3</sup> /h
k	The coverage factor	-
L	Length	m
$M_p$	Moment balance around point p	Nm
$\dot{m}$	Massflow	kg/s
m	Mass	kg
$m_{liq,tot}$	The total mass of liquid inside the actuator	kg
Nu	Nusselt number	-
$P_{v,1}$	Vapor pressure in the container	Pa
$P_{v,2}$	Vapor pressure in the float	Pa
$P_{friction(v_tube)}$	Pressure drop inside the tube	Pa
p	Pivot point	
$Q_v$	Flowrate	m <sup>3</sup> /h
$\dot{Q}$	Thermal Power	W
$\dot{Q}_{c,i}$	Thermal power input collector	W
$\dot{Q}_{c,o}$	Thermal power output collector	W
$\dot{Q}_t$	Thermal power over tank	W
$\dot{Q}_{loss}$	Heat loss piping	W
R	Thermal Resistance	K/W
r	Moment arm	m
$R_a$	Rayleigh number	-
$R_e$	Reynolds number	-
S	Sensitivity	
T	Temperature	°C
T*	The reduced temperature difference	m <sup>2</sup> K/W
$T_1$	Tank 1	°C
$T_2$	Tank 2	°C
$T_{1,min}$	Required minimum inlet temperature of the TDV	°C
t	Centre point of the tube	-
$t_1$	Start of the cycle	s
$t_2$	End of charging	s
$t_3$	End of the cycle	s
$T_c$	Temperature condensor	°C
U	Overall heattransfer coefficient	W/m <sup>2</sup> K
U	Voltage	V
u	uncertainty	-
$\dot{V}$	Flowrate	L/min
V	Volume	m <sup>3</sup>
v	Velocity	m/s
$\bar{x}$	Arithmetic mean	-

<b>Index</b>	<b>Description</b>
a	Ambient
av	Average
act	Actual
amb	Ambient
b	the collector
c	Center point / collector
c,in	Collector in
c,out	Collector out
exp	Expected
float	Float TDV
f	Fluid
G	Gross
HP	Heat Pipe
high	High temperature zone
hem	Hemisfeer
in	inlet collector
low	Low temperature zone
liq tube	Mass liquid tube
liq float	Liquid float TDV
liq, trans	Transferred liquid TDV
l	Liquid
ln	Logarithmic mean
m	Mean
out	Outlet collector
o	Outer
p	Absorber plate
red	Reduced
req	Required
setup	Experimental setup
t	Tank
tube	Tube TDV
th	Thermal
tot	total
usefull	Usefull thermal power
u	Usefull
u	usefull

---

<b>Acronym</b>	<b>Description</b>
BV	Ball valve
CV	Control valve
CFD	Computational Fluid Dynamics
DMP	Direct Multi-Pass
ETC	Evacuated Tube Collector
EMV	Electric Mixing Valve
FM	Flowmeter
HTF	Heat Transfer Fluid
ICS	Integral Collector Storage
M.	Measurement
MCV	Manual Control Valve
MD	Measuring Day
MLR	Multi Linear Regression
MP	Multi-Pass
PID	Proportional-Integral-Derivative
P&ID	Piping and instrument diagram
PWM	Pulse-Width Modulation
PV	Photovoltaic
PMP	Pump
SS	Steady State
SP	Single-Pass
TC	Thermocouple
TDV	Thermo-Differential Valve
TRN	Thermal Resistance Network



# Chapter 1

## Introduction

### 1.1 Direct Multi-Pass Solar system

Conico Valves B.V. developed a unique Direct Multi-Pass (DMP) Solar System for domestic hot water preparation. Each component in this system is shortly explained in the next sections. This DMP Solar System can be used in combination with heat pumps and biomass systems, but is also suited for use as a pré-heater for an existing boiler.

The DMP Solar system owes his name to two specific system characteristics. The first one is that it is a direct system, which implies that the storage tank is directly connected to the solar circuit and no extra heat exchanger is necessary. The second characteristic is that the Heat Transfer Fluid (HTF), in the solar circuit passes the Evacuated Tube Collector (ETC) multiple times, until the temperature of the HTF is slightly higher than the temperature of the storage tank. At this moment a Thermo-Differential Valve (TDV) opens and the hot water enters the upper part of storage tank (the auxiliary zone). The HTF in this system is water.

The main advantage of this 'multi-pass' system is that the solar circuit always provides the right temperature to the auxiliary zone of the storage tank at high flowrates. This water can directly be used for domestic heating, so no extra heating is necessary.

Figure 1.1 shows a schematic overview of main components of the system. More details about the ETC, the tank and the pump can be found in chapter 3. The TDV is explained in chapter 2 and the electrically controlled 3-way valve, including check valve at the inlet are not explained, since it is not integrated in the experimental set-up.

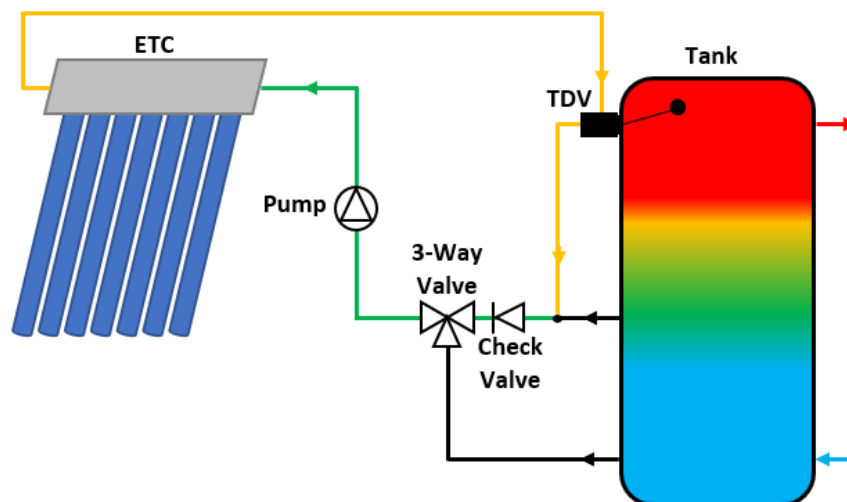


Figure 1.1: Schematic overview of the DMP Solar System

Conico Valves B.V. strives for the highest collector efficiency. Therefore, they developed algorithms for different operation modes of the DMP Solar System. Some of these modes are: anti-frost mode, start-stop mode, single-pass mode and multi-pass mode. Especially, in the multi-pass mode the

ETC tend to have a high efficiency. This is because a continuous high flow rate increases the heat transfer coefficient in the manifold, which increases collector efficiency. The idea of the DMP Solar System is to always maintain a high continuous flow rate and to prevent standing still.

### 1.1.1 Operation modes of the DMP Solar system

The working principle of the DMP Solar System can be explained best by going through one charging cycle of the storage tank during the period between sunrise and sunset of one specific day in the year. As explained in the previous section there are four operation modes that can be activated during the charging process. These operation modes will be explained below [28].

#### 1. Anti-frost mode

If there is no solar irradiation and the outside temperature is below 0°C the anti-frost mode is activated. The system periodically by-passes some of the hot water from the storage tank over the collector, in order to prevent that the collector and piping gets frozen.

#### 2. Charging in start-stop mode

At sunrise, the solar irradiation is relatively low, thus in this period start-stop mode activates. During this mode the system periodically switches between continuous flow and zero flow, to ensure the ETC has enough time to heat up water to a high temperature. Start-stop mode, instead of continuous flow, increases the collector efficiency during sunrise.

#### 3. Charging in single-pass mode

When the temperature in the solar circuit becomes higher than the temperature at the bottom of the storage tank, the three-way valve opens to the bottom, resulting in charging the storage tank continuously. During this mode the ETC is passed one single time. This continuous operation mode is also known as 'conventional' charging, since this is the same principle as a conventional solar collector system. In general, this requires a low flowrate to obtain an outlet temperature which is high enough to charge the tank.

#### 3. Charging in multi-pass mode

When the solar irradiation is high enough, the pump switches to continuous flow and if the inlet temperature of the TDV is lower than the storage tank temperature, the TDV by-passes the storage tank and the HTF passes multiple times through the solar circuit. As a result, the temperature of the HTF increases each cycle and when the inlet temperature of the TDV is higher than the auxiliary zone of the storage tank the TDV opens and the hot water enters the storage tank. Simultaneously, water from the middle of the storage tank returns to the ETC, resulting in a lower temperature in the solar circuit. When the colder flow reaches the TDV again, the TDV closes and the multi-pass cycle starts again. This cycle is repeated multiple times, until the auxiliary zone of the storage tank is homogeneously at a hot temperature.

#### 4. Again charging in single-pass mode

When the auxiliary zone and the middle of the storage tank are homogeneously at a hot temperature, the auxiliary zone is heated to a target temperature in single-pass mode in order to lift the entire auxiliary zone to a higher temperature level.

When the target temperature is reached, the 3-way valve switches and now cold water from the bottom of the tank returns to the ETC. The lower return temperature causes also a lower supply temperature, so the TDV switches and the flow bypasses the storage tank. However, the supply flow now enters the storage tank in the middle instead of returning it to the collector. This results in heating the supplementary zone of the storage tank.

## 1.2 Problem definition & research question

When the multi-pass system is in operation, see figure 1.1, the ETC operates under dynamic conditions. This is caused by the working principle of the TDV, as explained in the previous

section. Each time when the required temperature is reached the TDV opens and hot water enters the storage tank. Simultaneously, cold water exits the storage tank and is then pumped to the ETC. When the process temperature becomes lower than the required temperature, the TDV closes and the water is then pumped again to the ETC. This cycle repeats itself, until the process temperature becomes higher than the required temperature and the TDV opens again. More information about the switching behaviour of the TDV is presented in chapter 5. Due to these multiple cycles the system shows a dynamical behaviour. An example of this dynamical behaviour can be seen in figure 1.2. This data is retrieved from a random logging of Conico Valves by at a random day, with an unknown flowrate, so this figure is only included to show an example of the principle of the dynamical behaviour. As can be seen these temperatures show a periodic stair shaped pattern. If the periodic step change in inlet temperature, the flow rate and the irradiation stay constant, this pattern can be repeated infinitely long.

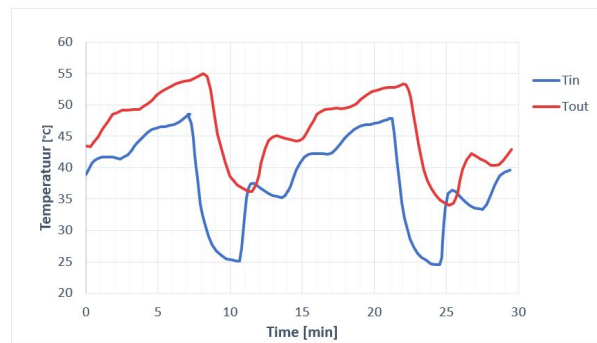


Figure 1.2: The in- and outlet temperatures show the dynamical behaviour of the multi-pass system.

The most important advantage of the multi-pass system is that only water with a specific 'hot' temperature is able to enter the storage tank. In this way, the incoming water approximately has the same temperature as the temperature layer in the storage tank, so no mixing occurs. Another advantage is that there is always 'hot' water available in the top layer of the storage tank.

However, there are some phenomena that can occur during the dynamic conditions in the multi-pass system, which may have a negative impact on the collector efficiency, as mentioned by Degenhart. One phenomenon is the drying out of the heat pipes and the second phenomenon is the temperature overshoot:

- According to Degenhart [9] there exists two performance limitations for heat pipes. The first one is the entrainment limit and the second one is the dry-out limit. If one of these limits is exceeded the heat-pipe can 'dry-out'. The entrainment limit may occur when the relative speed between vapor and condensate in the heat pipe is so high that the vapor forces the condensate upwards. In normal operation the function of the condensate is to transport heat, so if the condensate can not flow down to the bottom of the heat-pipe then heat transport is limited. This may result in increase in temperature at the middle- and bottom of the heat pipe (in this case the lower part of the evaporator is dry). The dry-out limit can be reached when the operating temperature is so high that there is not enough condensate available to transfer the heat (lower part of the evaporator is dry). The drying out of heat pipes can most likely occur when the TDV opens and the cold water from the storage tank flows through the manifold during the first cycle (it might be possible that it also occurs at successive cycles). At this moment the thermal power of the heat pipe  $Q_{HP}$  rises tremendously and extra water in the heat pipes evaporate. If in this case the entrainment limit is reached, the lower part of the evaporator may dry-out, resulting in a higher temperature of the absorber and more heat losses to the environment.

To maintain the efficiency as high as possible, it is desired that this period of drying out is

short as possible. This might be done by increasing the flow rate, since the total time of this thermal power peak shortens. However, by increasing the massflow, also the thermal power rises. It seems that a trade of has to be made and therefore experimental research is required.

- The temperature overshoot can occur slightly before the TDV is starting to close. This overshoot results in an increase in the average collector temperature and so has negative influence on the collector efficiency.

Therefore, it is desirable that these phenomena occur as little as possible to achieve the highest collector efficiency.

As described in the previous section, Degenhart determined, among other things, the collector efficiency during steady state conditions and during start-stop mode. However, the main operation mode of the DMP Solar System is the multi-pass mode, which shows unsteady behaviour. Especially the dynamic behaviour of the system during this mode is still unclear. Currently, Conico Valves B.V. can not perform accurate performance calculations on yearly basis (yearly energy gain), since the collector efficiency and other collector parameters during the dynamic conditions are still unclear. Therefore, the focus of this research is to investigate the thermal efficiency of the multi-pass system experimentally and to compare these results with single pass measurements.

As a result, the following research question can be formulated:

*What is the thermal performance of the collector and the total system, during the dynamic conditions of the multi-pass system, and what is the difference compared to a single-pass system?*

## 1.3 Research Plan and Project Objectives

In order to answer the research question properly a research plan is presented in this chapter. Also the experimental- en theoretical method are be presented.

As can be observed, the research question consists mainly of experimental research. Namely, the experimental determination of the thermal performance of single- and multi-pass mode. However, also a small part of this research will cover the switching behaviour of the TDV. All research parts will discussed separately in the next section and the corresponding objectives are elaborated. The objectives are presented in the form of sub-questions or as tasks and are numbered.

### 1.3.1 New experimental set-up

For the experimental part a new set-up need to be built. With the current set-up some slow dynamic conditions can be simulated, but no periodic step change of the inlet temperature can be applied. The periodic step change of the inlet temperature causes a fast transient response of the system and especially this periodic fast response can not be simulated with the current set-up. This means that the real dynamic behaviour of the multi-pass system can not be captured. Therefore, it is highly important that a new set-up will be designed and built, in order to capture the dynamic behaviour of multi-pass system. The following objective can be formulated as:

1) *Designing and building an experimental set-up, which can run the multi- and single-pass mode and can measure the dynamic behaviour of all process parameters.*

When the experimental set-up is built, experiments will be conducted to determine the thermal performance of the system. During the experiments the influence of the flowrate, the periodic step change in inlet temperature and the solar irradiation on the thermal efficiency will be investigated.

### 1.3.2 Experimental Research

When the new test setup is built, measurements on this test setup should be conducted in order to experimentally determine the thermal performance of the system, during the dynamic conditions of the multi-pass system. A measure of the thermal performance is the thermal efficiency. It is desirable that drying-out of the heat pipes and a temperature overshoot occur as little as possible to achieve the highest collector efficiency. Therefore, the following objective can be proposed:

2) *Measuring all process parameters in order to determine the thermal efficiency during multi-pass mode.*

For this objective it can also be investigated what the optimal operation condition is to achieve the highest thermal efficiency. The thermal efficiency, namely, depends on a number of process parameters, for example: the flowrate ( $\dot{V}$ ), the inlet temperature of the collector ( $T_{in}$ ) and the solar irradiation ( $G$ ). During multi-pass mode  $T_{in}$  depends, among other things, on the low- and high temperature zone of the tank ( $T_{low}$  and  $T_{high}$  respectively), which is explained in 4.1.1. The definition of the thermal efficiency is explained in chapter 2. This research focuses on the variation of flowrate, irradiance, and the temperature difference between  $T_{low}$  and  $T_{high}$  ( $\Delta T_t$ ), which is explained in chapter 4.

In order to make a comparison between the operation modes single- and multi-pass also single pass measurements should be conducted. Degenhart conducted steady state measurements at different operation conditions, but since the experimental set-up is different it is more reliable to make a comparison with the same set-up. This rises the following objective:

3) *Measuring all process parameters in order to determine the thermal efficiency during single-pass mode.*

The driving force behind the multi-pass mode is the TDV. To have a better understanding of the working principle of this valve a theoretical model needs to be developed in order to calculate

the switching temperatures and switching times for opening and closing the valve. With the experimental set-up it is possible to compare the theoretical model with experimental results. Therefore, the final objective of this research can be formulated as followed:

4) *Creating a theoretical model to obtain more insight in the switching behaviour of the TDV.*

The ultimate goal for Conico Valves bv is to integrate such a model in a simulation tool such as TRNSYS to accurately predict the switching behaviour and to improve the model accuracy. However, for the scope of this research the development of the theoretical model is only meant to have a better understanding of the working principle and to compare these results with available test results. The next step is to validate this model on larger scale, before it can be implemented in a simulation tool.

## Chapter 2

# Solar Collector Test Methods

### 2.1 Evacuated Tube Collector with heatpipe

Before the test methods will be presented a short description of the solar collector is given in this section to have more insight in the working principle. In this research a evacuated tube collector with heatpipes is evaluated (type Sydney). For simplicity the evacuated tube collector with heat pipe is called 'solar collector' in this thesis. This solar collector is equipped with heat pipes to transfer the heat to the the HTF inside the manifold.

Figure 2.1 shows an overview of all main components of the solar collector on the left hand side and an overview of the working principle of the heat pipe is presented on the right hand side.

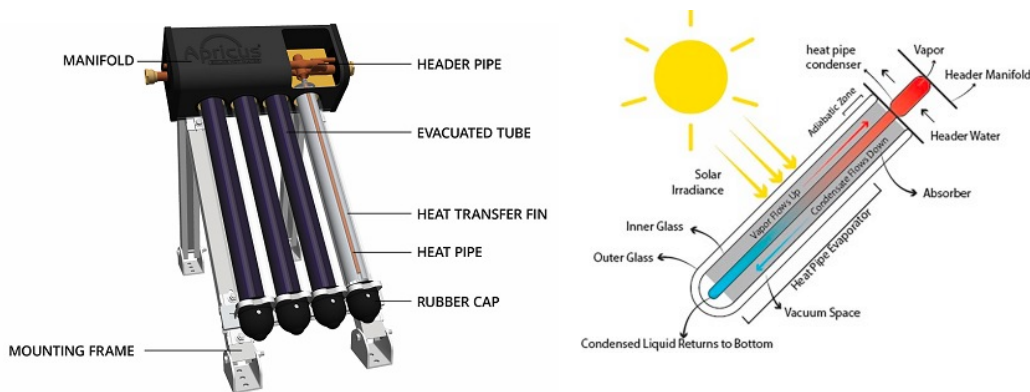


Figure 2.1: General description of the components of an evacuated tube collector with heat pipes. At the right hand side the working principle of the heat pipe is presented.

The solar collector is equipped with a cylindrical absorber, which is coated at the inner glass of the evacuated tube. When solar irradiance enters the evacuated tube, the absorber heats up and the heat is transported via an aluminum fin to the heat pipe. The heatpipe consists of an evaporator and a condenser. The evaporator has close contact with the aluminum fin and the condenser is mounted in a header pipe inside the manifold. After the heat is transported to the evaporator, vapor is starting to form inside the evaporator, which is forced upwards due to a thermosyphon principle. Then the vapor is cooled in the condenser and when all latent heat is extracted, condensate starts to form. The condensate flows down due to gravity and the cycle starts again. In the end of the cycle, the heat which is extracted from the condenser is absorbed by the water in the heater pipe, resulting in an increase in outlet temperature of the collector. Figure 2.2 shows a cross sectional overview of the evacuated tube and the manifold to clarify the working principle.

The manifold is an aluminum case, which is insulated with a thick layer of glass wool to reduce heat losses. The inner layer of the evacuated tube consist of vacuum, which also minimizes the heat losses.

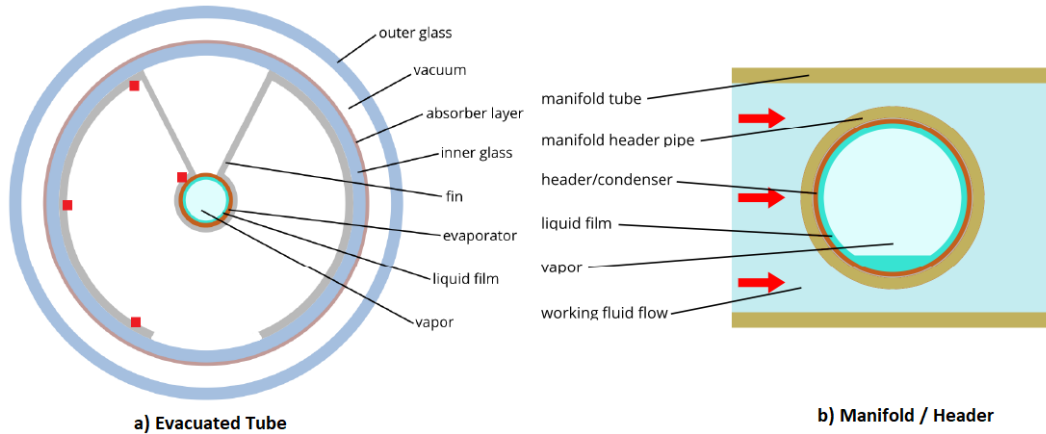


Figure 2.2: a) A cross sectional overview of the evacuated tube. b) A cross sectional overview of the manifold. The four red marks on the fin represent thermocouple positions and are explained in section 3.2 (Source: Degenhart [9])

## 2.2 Steady State Test Method

Degenhart already conducted some experiments of the start-stop mode [9], which is dynamic behaviour. He also conducted experiments in steady state conditions. The main goal of his research was to find the (optical) efficiency of an ETC for different operating conditions. The research of Degenhart was a continuation on the work of M.A. van Duijnhoven [10]. The results of both researchers are presented below.

Van Duijnhoven investigated the efficiency of the collector, which is used in the DMP Solar System, under different conditions during steady-state by conducting experimental research. In this research the optical efficiency was considered, which is a good measure of the collector performance, assuming the collector is at ambient temperature. Van Duijnhoven concluded that three parameters influences the (optical) efficiency, namely: massflow, inlet temperature and solar irradiation. He also concluded that by increasing the inlet temperature the efficiency of the collector decreases.

Because the collector parameters had been determined incorrectly by van Duijnhoven, R.B. Degenhart performed experiments with a constant inlet temperature again. He increased accuracy by using a broader range of inlet temperatures.

The test setup of van Duijnhoven is improved by Degenhart with the recommendations of van Duijnhoven. Furthermore, PID controlled valves, a new chiller, a particle filter and a by-pass are added to the test setup. However, to determine the efficiency of the multi-pass system another experimental set-up need to be built, including a storage tank with TDV. Degenhart also added 24 thermocouples inside one vacuum tube in order to monitor the temperature distribution during the experiments.

The main goal of the research of Degenhart was to use the collector parameters  $a_1$  and  $a_2$  of the Hottel-Whiller-Bliss equation, see equation (2.7), in order to determine  $\eta_0$ . The main theory of the Hottel-Whiller-Bliss equation will be explained shortly below.

First the thermal efficiency ( $\eta_{th}$ ) of the collector is calculated by dividing the thermal power output of the collector ( $\dot{Q}_{c,out}$ ) by the thermal power input ( $\dot{Q}_{c,in}$ ). Were  $\dot{Q}_{c,out}$  is defined by the massflow ( $\dot{m}$ ), specific heat ( $c_p$ ) and the temperature difference over the collector ( $\Delta T_c$ ), see equation (2.2).  $\dot{Q}_{c,in}$  is specified by the total incoming solar irradiance ( $G$ ) and the aperture area



of the collector ( $A_a$ ), see equation (2.1).

$$\dot{Q}_{c,in} = GA_a \quad (2.1)$$

$$\dot{Q}_{c,out} = \dot{m}c_p\Delta T_c \quad (2.2)$$

Finally,  $\eta_{th}$  can be calculated with equation (2.3).

$$\eta_{th} = \frac{\dot{Q}_{c,out}}{\dot{Q}_{c,in}} = \frac{\dot{m}c_p\Delta T_c}{GA_a} \quad (2.3)$$

Degenhart used the Hottel-Whillier-Bliss equation in his work, which is a reduced form of the instantaneous thermal efficiency of conventional flat plate collectors and ETCs in the terms of design parameters [8], see equation (2.4).

In the collector efficiency analysis described in the thesis of Degenhart [9] the model assumes that the entire tube is at mean fluid temperature  $T_{mean} = \frac{1}{2}(T_{in} + T_{out})$ . This is also according to the European standards (e.g. EN 12975-2: 2006) [21].

$$\eta = F' \left( \tau_{og}\alpha_{abs} - U_L \frac{T_m - T_a}{G} \right) \quad (2.4)$$

Where, the collector efficiency factor ( $F'$ ) is the ratio of the actual collector useful heat output compared to the useful heat output if the absorber would be at mean fluid temperature. The definition can be found in the thesis of Degenhart [9]. It is also known as the effectiveness of a collector as a heat exchanger [8].  $U_L$  is called the collector heat loss coefficient and is often given by the manufacturer, however, it is highly important that this parameters is not constant for ETCs.  $\tau_{og}$  and  $\alpha_{abs}$  are the transmittance coefficient of the outer glass of the evacuated tube and the absorption coefficient respectively.

The first 3 parameters in equation (2.4) represent the optical efficiency, see equation (E.17), and the product  $F'U_L$  is related to heat loss of the ETC. The latter term can be rewritten to another form including the linear heat loss coefficient ( $a1$ ) and the quadratic heat loss term ( $a2$ ), see equation (2.6) [27]. According to Degenhart [9]  $a1$  represents mostly convection loss and  $a2$  represents mostly convection and radiation loss.

$$\eta_0 = F'\tau_{og}\alpha_{abs} \quad (2.5)$$

$$F'U_L = a1 + a2(T_{mean} - T_{amb}) \quad (2.6)$$

Finally, the most practical form of the Hottel-Whillier-Bliss equation can be obtained by substituting equation (E.17) and (2.6) in equation (2.4):

$$\eta = \eta_0 - a1 \frac{(T_{mean} - T_{amb})}{G} - a2 \frac{(T_{mean} - T_{amb})^2}{G} \quad (2.7)$$

Degenhart performed one experiment to acquire  $a_1$  and  $a_2$ . During steady-state Degenhart assumed that parameters  $a_1$  and  $a_2$  are constant, regardless of the chosen flow rate or irradiation. This is a valid assumption that is covered in the book of Kalogirou [21]. According this experiment it turned out that  $\eta_0 = 0,7502$ ,  $a_1 = 1,908 \pm 0,5686$  and  $a_2 = 0,0226 \pm 0,0182$ . These values were in reasonable accordance with the parameters provided by the Solar Keymark certificate of

the collector, see figure F.1. After  $a_1$  and  $a_2$  are determined, the optical efficiency is experimentally determined for different continuous flow rates. According to these experiments it can be concluded that  $\eta_0$  increases when the flow rate increases. For flow rates higher than 4 L/min, the optical efficiency seems to converge to a approximately 0.77. Also a large drop in efficiency could be observed when the flow rate is below 0.5 L/min. These findings are also supported by the CFD model.

Additional literature review of steady state test methods can be found in appendix A.1.

### 2.2.1 Drying-out heat pipes

Degenhart showed also that the decrease of  $\eta_0$  seemed to be proportional to the dry-out of the heatpipes. At low tilt angles it turned out that  $\eta_0$  is up to 10% lower at high irradiation (PV800) comparing to low irradiation (PV200). This is due to the extra load that is put on the heat pipes. An important recommendation to prevent dry-out is is not using a tilt angle below 10° for a 24mm condensor.

He also concluded that the decrease in  $\eta_0$  is caused by drying-out of the bottom of the heatpipe. Drying out of the heat pipes can be observed when the thermocouples, which are mounted on the heatpipe, show a large jump in temperature.

## 2.3 Dynamic Test Method

### 2.3.1 Quasi-dynamic test method

NEN-EN-ISO 9806-2017 also proposed a quasi-dynamic test method, but this is more intended to capture the dynamic behaviour when the solar irradiation and solar incidence angle are varying during a day between sunrise and sunset. This means slow variations in ambient conditions. No method is proposed for a varying inlet temperature for instance. Therefore, it can be concluded that this method is not suitable for multi-pass mode. However, one method is described to determine the effective thermal capacity. In further research it might be interesting to determine this value. However, this value cannot be used in TRNSYS since there only the thermal capacity of the fluid is used in the thermal model. This means that a new thermal model in TRNSYS need to be developed. More information about this quasi-dynamic method can be found in appendix A.2. More information about TRNSYS can be found in section 2.4.

### 2.3.2 Dynamic test method

In appendix A.3 an overview of all available dynamic test methods presented. These are complicated methods which also requires to develop a completely new thermal model (in TRNSYS). The development of a completely new thermal model does not fall within the scope of this research. This literature review was conducted in order to have a total overview off all available test methods and can be used in a possible continuation of this research for further research.

The following techniques are presented:

- One-node approach
- Multi-node approach
- Filtering technique with least square method
- Laplace transform technique
- Improved Transfer function Method

## 2.4 Test Method DMP Solar System

The main goal of Conico Valves is to accurately predict the yearly energy gain of DMP Solar System. Preferably with TRNSYS, because they already conducted a lot of research into this simulation tool. Currently, Jiang [19] already developed a model of the DMP Solar System in TRNSYS, with a Type 538 evacuated tube collector. Currently, the collector coefficients are implemented, which are obtained by steady state experiments (Either determined by Solar Keymark or by Degenhart [9]). However, during multi-pass mode these coefficients may be different. The input parameters of this model are for example the optical efficiency  $\eta_0$ ,  $a_1$  and  $a_2$ . It is also possible to specify the thermal capacity of the fluid inside the collector. More information about the effective thermal capacity in TRNSYS can be found in appendix C.

### Future research

In ideal situation the TRNSYS model need to be validated with experimental results of multi-pass system. This can be realized with an extensive collector parameter analysis. After the collector parameter analysis, it can be concluded whether or not this original TRNSYS model is capable to accurately predict the yearly energy gain of the DMP Solar System. If it turns out that this model can not be used for accurately prediction the yearly energy gain, for example because the thermal capacity it a limited factor, more research need to be conducted in order to develop a transient model with correct effective thermal capacity. Section A.3 presents all possible dynamic test methods which are available.

### Focus current research

This research focuses only on experimental research an not to validate the TRNSYS model with experimental results. It focuses on designing and building of an experimental set-up to conduct measurements on the single- and multi-pass mode. Then the dynamic behaviour of the multi-pass mode is investigated. Furthermore, this research focuses on the determination of the thermal- and optical efficiency of the collector and of the total thermal efficiency of the entire system. Also a comparison is made between the total thermal efficiency of the entire system for single-pass mode and multi-pass mode. Below the experimental method is described briefly. All details are described in section 4.2.1 and 4.1.1.

### Thermal efficiency collector

In single-pass mode the thermal efficiency of the collector can simply be calculated with equation 2.3, because it is a steady state condition. It is important to emphasise that this equation only can be used during steady state conditions, since no transient term is included. For transient conditions; therefore, equation (A.15) need to be used, which includes transient terms. However, this is a very complicated function to determine the thermal efficiency and the effective thermal capacity of the collector needs to be accurately known. Therefore, this is a very unpractical way to measure the thermal efficiency of a system, which may involve high uncertainties. Therefore, it is decided to measure the thermal efficiency of the multi-pass mode with constant  $T_{low}$  and  $T_{high}$ , resulting in identical consecutive cycles over time. When identical consecutive cycles over time can be obtained, all process temperatures at the start of the cycle are equal to the process temperatures at the end of the cycle, resulting in a semi-steady state condition: The process within one cycle is transient, but since this cycle can be repeated identically this can be seen as steady state. Now, the thermal efficiency can also be calculated with equation 2.3.

### Collector coefficients

As mentioned before, Degenhart determined these collector coefficients for single-pass steady state conditions. First, he determined  $a_1$  and  $a_2$  and assumed that these coefficients are always constant. With this assumption he determined the optical efficiency as function of flowrate.

Since the multi-pass mode can be measured in steady state condition, also the collector coefficients might be determined as being steady state. So a similar procedure can be executed. As a result the collector coefficients of the multi-pass mode can be seen as steady state collector coefficients during dynamic conditions of the multi-pass mode. The main advantage is that these coefficients

might be used in TRNSYS in order to calculate the yearly energy gain of the collector.

This research focuses on the determination of the optical efficiency and not on the determination of the collector coefficients  $a_1$  and  $a_2$ , since there is a limited amount of time to conduct experiments. During this research it is, therefore, decided to use the same  $a_1$  and  $a_2$ , which are determined by Degenhart. This means that the optical efficiency can be obtained by rewriting equation (2.7), see 2.8.

$$\eta_0 = \eta + a_1 \frac{(T_m - T_a)}{G} + a_2 \frac{(T_m - T_a)^2}{G} \quad (2.8)$$

Or written in a different form, with  $T_{red}$ , see equation (2.9) and (2.10):

$$\eta_0 = \eta + a_1 T_{red} + a_2 G T_{red}^2 \quad (2.9)$$

$$T_{red} = \frac{T_m - T_a}{G} \quad (2.10)$$

For the optical efficiency it is of high importance what the definition of the mean collector temperature is. In this research the mean temperature of the collector is evaluated as the mean temperature of the in- and outlet of the collector, see (2.11).

$$T_m = \frac{T_{c,out} - T_{c,in}}{2} \quad (2.11)$$

For all measurements it is tried to let  $T_{red}$  as close as possible to 0 to reduce the uncertainty of the correctness of the assumed parameters  $a_1$  and  $a_2$ . In future research more experiments can be conducted in order to determine  $a_1$  and  $a_2$  for the multi-pass mode. Then it can also be interested to conduct research if these parameters are constant for different flowrates and irradiances.

#### **Thermal efficiency total system**

For the determination of the thermal efficiency of the total system, more information about sensor positions is required. Therefore, this method is included in section 4.1.1.

# Chapter 3

## Experimental set-up

In this chapter the design strategy of the test-setup is discussed. First, the design requirements will be presented. Then, the design of the experimental setup and the design choices of each component will be discussed. Finally, some re-designs are presented to have more insight in the rationale behind the design choices.

### 3.1 Design requirements

The first step in the design process is to determine the design requirements. According to these requirements the entire design of the test setup is realized. Together with Conico Valves bv. a list of requirements is composed. The main requirements are presented below:

1. The test setup needs to handle the operation modes single-pass and multi-pass.
2. During multi-pass mode the system needs to generate identical consecutive cycles, in order to achieve steady state.
3. Process parameters such as flow rate, charging temperature ( $T_{high}$ ) and return temperature ( $T_{low}$ ) have to be set by the user of the set-up and have to be controlled automatically.
4. All process parameters such as flow rate and temperature have to be monitored accurately to measure the dynamic behaviour of the multi-pass mode.

More detailed requirements about the process parameters can be found in table 3.1. The range of the flowrate is partly based on ISO 9806:2017, but also based on experience of Conico Valves bv. ISO 9806:2017 suggests a massflow of 0.02 kg/s per gross collector area ( $m^2$ ) for steady state testing. The gross collector area of the test setup is  $4.49/3 = 1.50 m^2$ , which results in a flowrate of 1.80 L/min. The gross collector area is obtained from the Solar Keymark certificate in appendix F. Since the amount of tubes in the test setup is 10 instead of 30, the gross collector area is divided by 3. For testing the multi-pass mode, which is at higher flowrates, it is assumed that doubling the flowrate should be high enough. Therefore, 4 L/min is required as maximum flowrate. As can be seen in table a maximum flowrate of 10 L/min; therefore, this requirement is met.

In table 3.2 the required accuracy or uncertainty and maximum allowed deviation during experiments is presented. Also the actual realized uncertainty is presented. These requirements are obtained from ISO 9806:2017 [1] and are meant for steady state testing. Since multi-pass experiments are not the same steady state as mentioned in this norm, some parameters such as  $T_{in}$  and  $T_{out}$  can not be met, thus these requirements are meant for single-pass measurements.

Table 3.1: Requirements of process parameters and what is actually realized.

Process Parameters	Requirements	Realization
$\dot{V}$ [L/min]	0.1 - 4.0 L/min	0.1 - 10.0 L/min is realized
$T_{low}$	30 - 80 °C	10 - 80 °C is realized
$T_{high}$	10 - 60 °C	10 - 80 °C is realized

Table 3.2: Required accuracy or uncertainty and maximum allowed deviation during experiments. Also the actual realized uncertainty is presented.

Process Parameter	Max deviation	Required Accuracy
$\dot{V}$ [L/min]	$\pm 1\%$	std. uncertainty $< \pm 1\%$
G	$\pm 50$ [W/m <sup>2</sup> ]	Class 1 pyranometer or better; ISO 9060
$T_{in}$	$\pm 0.1$ °C	see $\Delta T$
$T_{out}$	$\pm 0.4$ °C	see $\Delta T$
$\Delta T$	$\pm 0.5$ °C	Accuracy $< 1\%$ std. uncertainty $< 0.05$ °C
$T_{amb}$	$\pm 1.5$ °C	std. uncertainty $< 0.5$ °C

How these requirements are met will be explained in section 3.3 in detail. Also the design choices of each component will be explained.

## 3.2 Original Experimental Set-up

### 3.2.1 Piping and Instrument diagram

The original experimental set-up is designed and optimised by other students for steady-state measurements. The piping and instrument diagram of this set-up is presented in figure 3.1. The part outlined with a red dashed line represent the original part and the rest represents the new part (DMP set-up). The original set-up is only used to transport cold water from the chiller to the new test set-up. To ensure that cold water from the chiller can be transported to the new DMP set-up two extra T-pieces, 2 ball valves and 2 flexible tubes of 4 meter are added, see also appendix I.2.

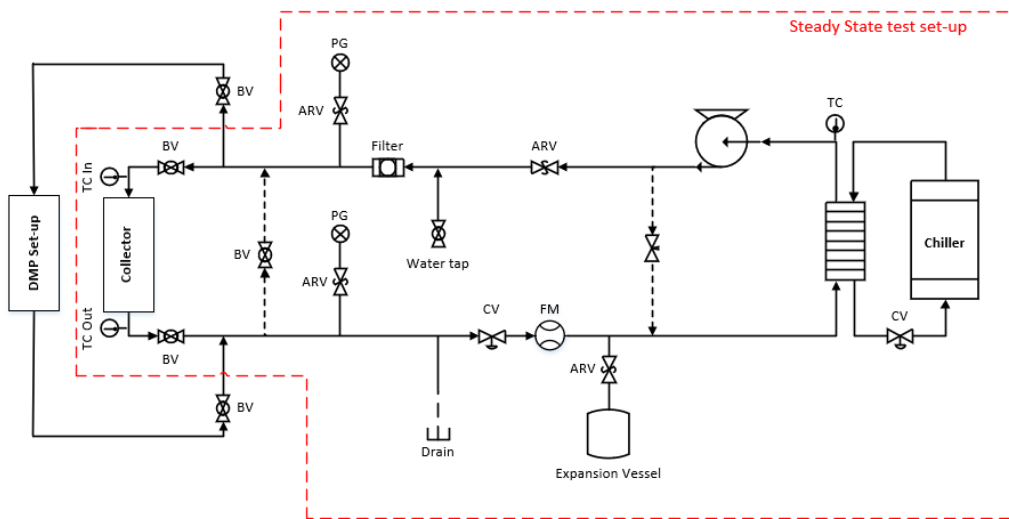


Figure 3.1: Piping and instrument diagram of the steady-state set-up.

### 3.2.2 Solar simulator

The solar simulator is designed by the company Eternal Sun. It is a type LA110200 Large Area Solar Simulator. It has 4 settings, namely: PV200, PV800, PV1000 and ST1000. The spectra of PV200, PV800 and PV1000 are designed to supply  $200 \text{ W/m}^2$ ,  $800 \text{ W/m}^2$  and  $1000 \text{ W/m}^2$  in de PV spectrum (400-1100nm). However, it also supplies irradiance at higher wavelengths; therefore, the pyranometer measures a higher irradiance. The ST1000 setting is designed to supply  $1000 \text{ W/m}^2$  over the entire spectrum; therefore, the pyranometer measures  $1000 \text{ W/m}^2$ . To make a comparison it decided to only use the PV settings, because these settings have a variation in irradiance and the ST setting has only 1 setting. Furthermore, it is decided not to compare the ST1000 with the PV settings, since these spectra are built up differently.

At the bottom of the solar simulator a polymer sheet is applied to spread the light and represent the cold sky. The solar simulator is calibrated at a distance of 10 cm from the cold sky, according to IEC 60904-9.

### 3.2.3 Sensors original set-up

The ambient sensors (thermocouple type K) and the pyranometer of the original set-up are also used for this research. The position of these sensors are presented in figure 3.2. The pyranometer is placed at a distance of 10 cm from the solar simulator, which is the same distance as for the evacuated tubes. Furthermore, the ambient sensors are placed in small open tubes, covered with aluminium foil to protect them from radiation energy. The thermocouples on the left- and right hand side are placed approximately 10 cm from the outer tubes. The upper and lower sensors are placed on both ends of the solar simulator.

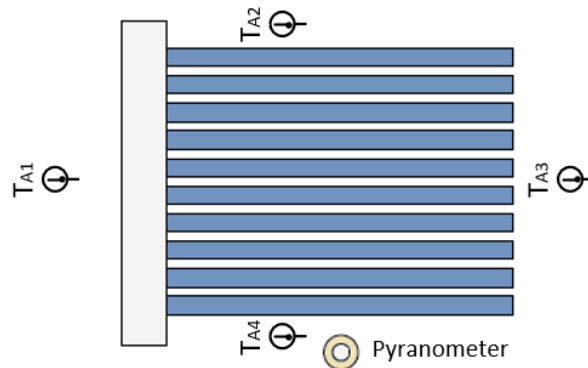


Figure 3.2: Measuring positions of the ambient temperature sensors and the pyranometer around the solar collector

To obtain more insight in the temperature distribution inside an evacuated tube Degenhart installed 22 thermocouples on the fin and 2 thermocouples on the condenser. It is important to emphasise that these thermocouples are installed in the first tube of the collector, which is as close as possible to the collector inlet.

10 thermocouples are placed close to the evaporator and 10 thermocouples were placed close to the absorber (see also figure 2.2 for further explanation of the position). Thermocouple T1 is placed at the bottom of the heat-pipe and T3 is expected to be at the same height as the top of the liquid pool. Since the distance between the thermocouples of the absorber and the evaporator are approximately the same, the thermal resistance for each thermocouple pair is also the same. This also means that the temperature difference of a thermocouple pair is linearly related to the radial heat flux in the fin.

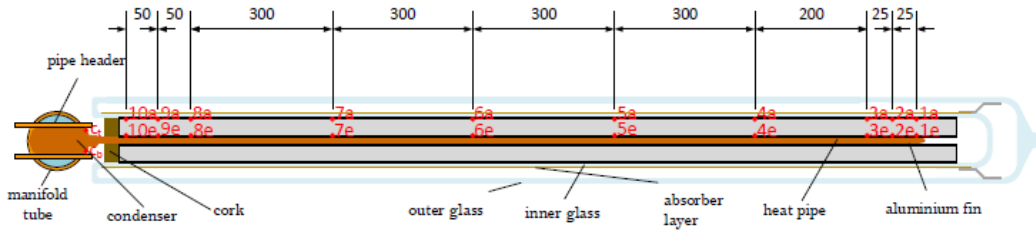


Figure 3.3: Thermocouple positions inside the first evacuated tube. Source: Degenhart [9]

One thermocouple is installed at the top of the condenser (Tct) and one is installed at the bottom of the condenser (Tcb).

At position 8 two additional thermocouples (T8b and T8c) were installed, see figure 2.2. These thermocouples were mounted in the middle and at the end of the fin respectively. Unfortunately T8b was broken at the beginning of this research. It is decided not to replace this thermocouple since the set-up is very fragile. These thermocouples were mounted in order to capture the gradient along the tangential direction of the aluminum fin.

### 3.2.4 Dimensions evacuated tube collector

The collector consists of 10 evacuated tubes. Since the specifications are only available for a configuration with 30 tubes, all dimensions should be divided by three, see figure F.1. This results in an aperture area ( $A_a$ ) of  $2.78/3 = 1.50 \text{ m}^2$  and a gross area of  $2.78/3 = 0.93 \text{ m}^2$ .

### 3.2.5 Additions to original set-up

Some practical changes to the original set-up are applied to improve it. In this section 1 example is given, the rest can be found in appendix I.

#### Extra insulation manifold

The manifold of the collector has space for 16 evacuated tubes; however, only 10 tubes are used for the measurements. This means that there are 6 empty holes for potential condensers. During the measurements of Degenhart [9], these holes were partly covered with some paper towel. However, still some copper of the manifold was visible, which means that the collector had more heat losses than in reality. For this research those 6 holes are filled with Rockwool and are then also covered with an extra layer of 8 cm thick Rockwool, to ensure high quality insulation, see figure 3.4.



Figure 3.4: Insulation of the empty manifold holes

Also the piping between the manifold and the thermocouples at the in- and outlet of the collector are properly insulated. This was not the case during the measurements of Degenhart.



### 3.3 Design Experimental Set-up

Keeping in mind the requirements of section 3.1 a experimental set-up is designed to perform single- and multi-pass measurements. The design is presented in the form of a piping and instrument diagram (P&ID), see figure 3.5. The design of the solar circuit, the cooling circuit and the storage tank are presented in the following sections. A multi-pass experiment can be run via TC4 and de TDV and a single-pass experiment can be run via TC5 (the top of the tank).

TC22 is not presented in this figure, but this thermocouple can measure the ambient temperature around the set-up. Please keep in mind, that this sensor is not meant to measure the ambient temperature around the solar collector.

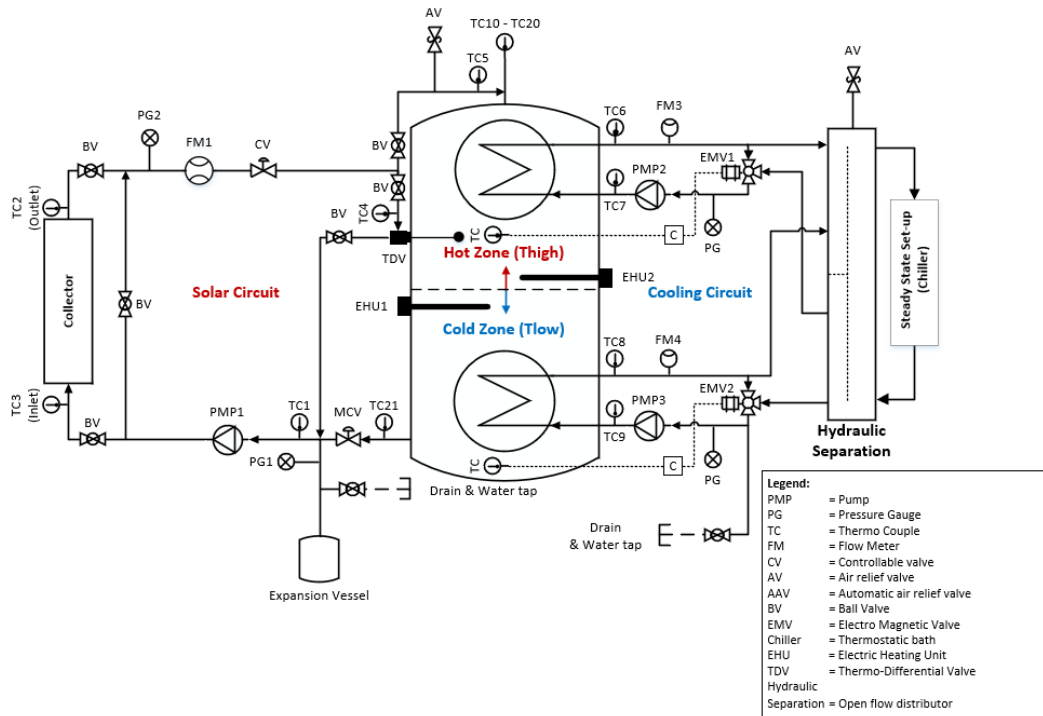


Figure 3.5: Piping and instrument diagram of the set-up.

#### 3.3.1 Design storage tank

As mentioned in the later section no storage tank is needed for single-pass mode, simply because the Thermo-Differential Valve (TDV) is not included in the system. This valve needs to be mounted at the inlet of a storage tank. Conico Valves develops different types of TDV's; therefore, it is required that all types can be tested in this set-up in the future. The length of the tube of the float can be varied up until approximately 50 cm. For this research a TDV with tube length of approximately 50 cm is used. Therefore, a minimum tank diameter of 0.5 m is required.

In order to achieve a steady state condition, very steady consecutive cycles needs to be generated by the set-up. This means that the supply temperature for the collector and the injection temperature of the tank needs to be constant during a measurement day. This can only be obtained when the lower part of the tank remains constant, for a constant supply temperature and when the higher part of the tank, where the TDV is inserted, remains constant to ensure a constant injection temperature. Those parts of the tank are called the low temperature zone ( $T_{low}$ ) and the high temperature zone ( $T_{high}$ ) of the tank. The heat from the solar collector is added at the high

temperature zone  $T_{high}$ . When hot water is being injected, at the same time, cold water from  $T_{low}$  is forced out of the tank, which lowers the thermocline inside the tank. The heat that is added to the tank needs to be cooled in order to remain constant temperatures of  $T_{high}$  and  $T_{low}$ .

### Helically Coiled Heat Exchangers

It is decided to use 2 helically coiled heat exchangers, that are able to control the temperature of both zones. The tank and the helically coiled heat exchangers are delivered by the supplier TWL, since Conico Valves has close contact with this company. TWL has a standard catalogue and has standard helically coiled heat exchangers for certain tank diameters. To reduce the costs of the tank and the heat exchangers it is decided to choose a standard solution rather than a custom made design. A calculation program is developed to calculate the performance of the heat exchangers. The performance of both heat exchangers is calculated in Appendix G. It turned out that the lower helically coil is the most critical one. However, it still has a design margin (overcapacity) of 38.9% when using a  $T_{low}$  of 10°C and a maximum capacity of the collector. It can be concluded that both heat exchangers are suitable for the application.

### Heaters

In normal operation the storage tank is already at a certain temperature before an experiment is started at the beginning of the day. The tank only cooled down slightly to the environment. In this case the heaters need to heat up just a few degrees. However, it might be possible that the another tank temperature is needed for a certain type of experiment. It is estimated that a charging speed of 20°C per hour is desirable. In this case it takes approximately 30-90 minutes to heat up the top part of the tank with 10-30 degrees at the start of the day. As a result, 2 heaters are required with a capacity of 3 kW each. The top part of the tank has a content of 214 Liter and it is calculated that these heaters can heat this volume of water with 24.4°C per hour. In practice it turned out that this was approximately 22.5°C per hour. The heaters are delivered by the company TWL.

### Height Storage Tank

The height of the storage tank is determined by the height of the helically coiled heat exchangers and some minimum required distances between components. The minimum required distance between the heaters and another component is 10-15 cm and the minimum required distance between the TDV and another component is estimated to be 15 cm, since the float has a range of 10 cm between open and closed position. All positions of the connections are based on these requirements. As a result, the total dimensions can be found in figure H.2. This is a technical drawing made by the company TWL and it also includes all specifications of the materials.

### Positions Thermocouples

Temperature measurements inside the tank are important to understand the how the cooling circuit needs to operate in order to control the temperatures of the zones in the tank. Figure 3.6 shows all positions of the thermocouples. In total 10 thermocouples (Type T, with diameter 3mm) are added to give more inside in the temperature distribution inside the tank. TC13, TC14 and TC15 can measure the temperature around the float of the TDV. TC16, TC17 and TC18 are added to to give more insight on the thermocline inside the tank. The most important sensors are TC14 and TC20, because those sensors are used for the PID controllers of the Electric Mixing Valves (EMV) to control the both temperature zones of the tank. Sensors TC10, TC11, TC12 and TC19 are added to gave more information about the temperatures around the helically coiled heat exchangers.

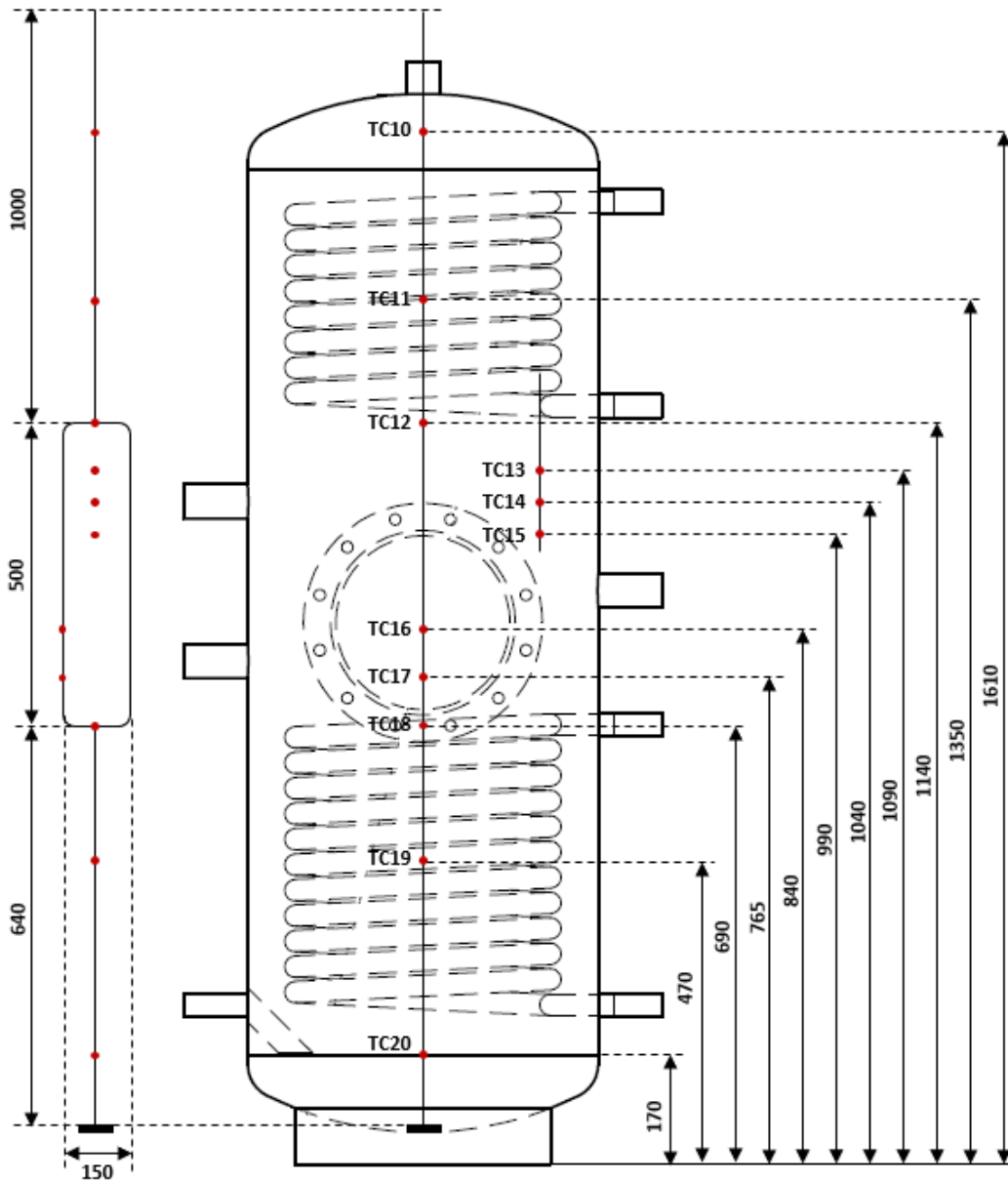


Figure 3.6: Positions of the thermocouples inside the tank. On the left hand side the stainless steel construction to mount the thermocouples is illustrated.

All sensors are inserted via the top of the tank, via a special devise developed by the company TC-Direct. This devise can guide 10 thermocouples through one tank connection, which is also leak tight. Because the top connection, the heaters and the TDV are placed in the centre of the tank, a steel construction is developed to guide all thermocouples to its correct position. This construction is presented on the left hand side of figure 3.6. This construction is inserted via a DN250 flange, mounted on the back of the tank. This construction is mounted on the bottom of tank with a strong magnet to hold it in place. The dimensions of the thermocouple construction is presented in figure H.10 in the appendix.

### 3.3.2 Thermo-Differential Valve

In this section the working principle of the Thermo-Differential Valve (TDV) will be explained. Chapter 5 also includes a theoretical approach of the switching moment and the switching time of the TDV. Furthermore, some experimental results are presented at the end of chapter 5, this section in order to compare these with the theoretical approach.

#### Working Principle

Directly at the inlet port of the storage tank a TDV is installed. This is a three-way switching valve, with 1 inlet and 2 outlets. It switches the flow direction based on the temperature difference between the inlet of the TDV and the temperature inside the storage tank. In figure 3.7 the working principle of the TDV is illustrated. As can be seen in this figure, the TDV consists of an actuator which consist of two main parts: a float, which is inserted into the storage tank and a small container, which is located inside the housing of the valve. The float and the container are connected with a thin tube and is filled with a working fluid (partly liquid phase and partly vapour phase). The type of working fluid and its properties are confidentially, therefore no data about this is included in this thesis.

The upper part of figure 3.7 shows the closed position of the TDV and in this case the temperature of the inlet of the TDV is lower than the tank temperature. In this case all liquid has been forced inside the container and therefore the float has risen upward. In closed position the water is by-passing the tank

The lower part in this figure shows the open position of the TDV and in this case the temperature of the inlet of the TDV is higher than the temperature inside the storage tank. In this case all liquid has been forced inside the float and therefore the float has sunk downwards. In open position the storage tank will be charged with hot water.

More about the thermodynamics and mechanics of the TDV will be explained in chapter 5.

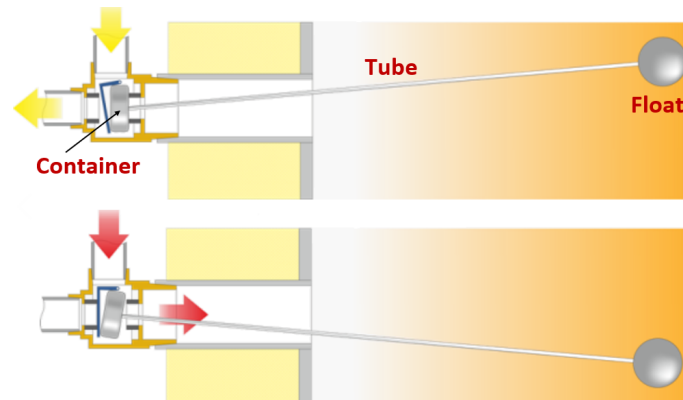


Figure 3.7: The working principle of the TDV in a cross-sectional perspective. The upper part shows the closed position (by-passing the tank) and the lower part shows the open position (charging the tank).

### 3.3.3 Design Solar Circuit

The solar circuit consists of supply- and a return line for the solar collector. Components with a high thermal inertia, such as a flowmeter and control valve are placed in the return line of the collector. This is desired to ensure that the cold water of the tank remains as cold as possible during the first loop, such as in normal domestic situations where no flowmeter and control valve are needed. So a more realistic situation is obtained.

A multi-pass experiment can be run via TC4 and the TDV and a single-pass experiment can be run via TC5. During multi-pass mode the water can either be injected into the storage tank or can be by-passed back to the collector. Another by-pass is added to by-pass the collector, just for practical purposes.

#### Valves

A manual control valve (MCV) is mounted in order to equalize the pressure drop of the by-pass line and the supply line. The valve is of the type STAD DN15 and has a wheel which can be manually adjusted to set the Kv-value. The ball valves (BV) are included to close a by-pass line, to switch between single- and multi-pass mode and to close the system when the collector is disconnected.

Furthermore a control valve (CV) is added to the solar circuit to control the flow accurately. This valve is an electro magnetic valve (EMV) of Siemens (MXG461B15-3) with a Kv- value of 3.0. This valve, is normally used as 3 way valve, but one side can be blocked and it can be operated like a regular flow control valve. This valve has a fast positioning time ( $<2$  s) and a very high resolution stroke (1 : 1000), due to its magnetic actuator. The control signal can be varied between 0-10V. To select a Kv-value the entire pressure drop of the set-up is calculated on fitting level. It turned out that the control valve needs to ensure a pressure drop of 3720 Pa at 6 L/min (max desired flowrate). With software of Bronckhorst a minimum Kv-value of 1.84 is calculated. Since the MXG461B15 control valves can be supplied with a Kv-value of 0.6, 1.5 or 3.0 m<sup>3</sup>/h, Kv-value of 3.0 m<sup>3</sup>/h is selected for this application.

The Thermo-Differential Valve is explained in section 5.

#### Pump

The pump in the old set-up has a maximum head of 4m and could supply a maximum flowrate of 4 L/min; therefore, it is decided to choose more powerful pump. For this application a pump of the type Wilo Yonos PARA ST15/7 PWM2 has been selected, which has a maximum head of 7m and is widely used in domestic hot water preparation system. One advantage of this pump is that the flow can be controlled via a Pulse-width modulation (PWM) signal. This signal can be varied between 0 and 100%, which changes the speed of the pump between 800 and 4660 rpm. The pump curve can be found in figure J.2 in the appendix. As can be observed, the pump curve changes lowers when increasing the PWM signal.

#### Sensors

Thermocouples (TC's) are added in order to measure the process temperatures. TC5 and TC21 measures the in- and outlet temperature of the tank and TC3 and TC2 measures the in- and outlet temperature of the collector respectively. TC4 measures the inlet temperature of the TDV and TC1 measures the temperature right after the by-pass line.

A flowmeter is mounted to measure the flowrate accurately. More information of these sensors can be found in section 3.4.

#### Piping

For all piping 22 mm copper is used in order to reduce the pressure drop in the in both circuits. In the old test set-up the pressure drop was problematic, so 22 mm is used for practical purposes. For the flexible tubes, tubes with a diameter of 11 mm are used. The supply line for the collector has a length of 295 mm and the return line of the collector has a length of 120 mm.

All piping is insulation with armaflex or thermaflex with a thickness of 13mm and conduction

coefficient of 0.04 W/mK.

### Auxiliary Components

An expansion vessel is installed to compensate for the pressure variations. The size of the vessel is calculated by software of Flamco. Also an air relief valve is installed at the top of the tank and a water tap and drain is installed in the lowest pipeline.

### 3.3.4 Design Cooling Circuit

The minimum supply temperature of the chiller is 5°C. The water in the cooling circuit needs to flow across approximately 12 meters of piping and flows across the old set-up with a lot of components which are not insulated. This means that the water is heated up by its surroundings, resulting in a minimum supply temperature of the tank of approximately 9°C. The lowest process temperature of this set-up is therefore 10°C.

### Hydraulic Separator

Since only one chiller is available and two different supply temperatures are required it is decided to create 2 cooling loops in order to control the temperatures  $T_{low}$  and  $T_{high}$  inside the tank. The supply water of the chiller needs to be divided over those two cooling loops. This is realised by using an hydraulic separator. The working principle is illustrated with a cross-sectional overview in figure 3.8. It is recommended that the flowrate of the chiller supply line is equal or higher than the flowrate of the combined supply lines of both cooling loops.

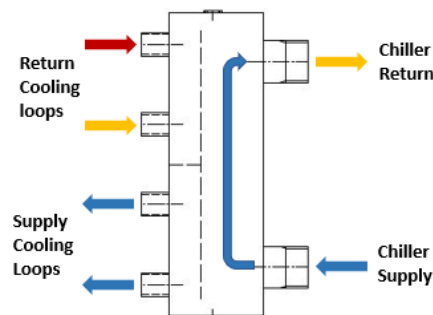


Figure 3.8: Cross sectional overview of the hydraulic separator

### Mixing Valves

In each cooling loop a electronic mixing valve (EMV) is added, which is able to control the temperature of each cooling loop to a desired value. The valves are the same type as for the control valve in the solar circuit, but with different Kv-value. The upper cooling loop has a MXG461B15-0.6 type mixing valve with a Kv-value 0.6 m<sup>3</sup>/h and the bottom cooling loop has a MXG461B15-1.5 with a Kv-value of 1.5 m<sup>3</sup>/h. Since the cold water supply of the upper cooling loop is very low, the lowest Kv-value is selected. With a Kv-value of 0.6 m<sup>3</sup>/h a maximum flowrate of 7.5 L/min is calculated. For the bottom cooling loop a flowrate of 10 L/min might be necessary; therefore, it is decided to choose a Kv-value of 1.5 m<sup>3</sup>/h, resulting in a maximum flowrate of 16.8 L/min.

### Sensors

For each heat exchanger a sensor is placed to monitor the in- and outlet temperature. Also a flow indicator is used in each cooling loop to monitor the flowrate. More information of these sensors can be found in section 3.4

### Auxiliary Components

No expansion vessel is needed in the cooling loops, since the old set-up already consists of an expansion vessel. The extra liquid content of the new set-up will not be a problem. An air relief

valve is installed at the highest point of the hydraulic separator, so air is able to collect there. A water drain is installed at the lowest pipeline. Water can be filled via the old set-up.

### 3.3.5 Layout of the set-up

When all components were selected a layout of the set-up is made on scale, which is presented in figure 3.10 and figure 3.11. The frame is built with standard 40 mm Hepco profiles, see figure H.6. With this type of profile a maximum deflection of 1.3 mm is realised in the critical beams below the storage tank, see figure H.7. All dimensions can be found in figure H.1. The back panels, where all component are mounted on, are made of Trespa panels. The dimensions of the panels are presented in figure H.11.

The total set-up is mounted on wheels. The wheels are supplied by Hepco, but unfortunately the wheels could not be mounted directly on the frame; therefore, 8 base plates are designed and manufactured in the workshop, see figure H.3 and H.4.

To mount the piping on the Trespa panels, spacers are designed out of thick PVC plates. In total 30 spacers are machined in the workshop, see figure H.9 for the dimensions. The hydraulic separator is mounted with 2 L shaped profiles and 2 clamping straps, see figure H.8.

The flanges for the flowmeters are manufactured in the workshop, see figure H.5 for the dimensions.

Furthermore an electric spacial is designed together with Theo de Groot, the position of this electric spacial is on the right hand side of the set-up, see figure H.1. The layout of the electric spacial is illustrated in figure 3.9.

Finally, the total bill of materials is presented in figure M.1, M.2 and M.3 in the appendix. In total approximately 800 components are used in this set-up.



Figure 3.9: Layout of the electric spacial.



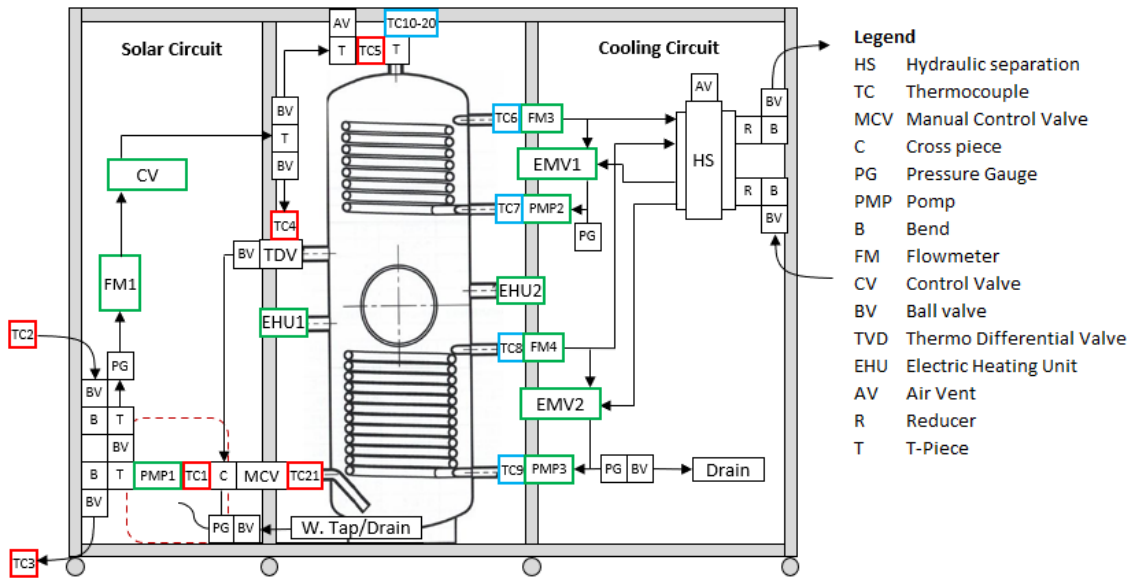


Figure 3.10: Layout of the set-up. All components are illustrated on scale.



Figure 3.11: Layout of the realized set-up.



## 3.4 Measurement Equipment new set-up

### 3.4.1 Thermocouples

In order to capture the dynamic behaviour it is of crucial importance to use thermocouples with a very fast reaction time. For TC1-TC5 and TC21 it is; therefore, decided to use class 1, type-T thermocouples with a 0.5 mm tip. The shaft of this thermocouple is still 3 mm, for practical purposes, but a potseal is used to create a 0.5mm tip. The tip also has a grounded junction to halve the reaction time. The reaction time is defined as the time it takes for the thermocouple to reach 62.3% of the end value, if the thermocouple is submerged from air into boiling water. The supplier TC-Direct specifies a reaction time of 0.03 seconds. For safety this value is multiplied by 5 to be 100% sure that a thermocouple reaches its final value within a certain amount of time. As a result it is expected that these thermocouple reach its final value within 0.15 seconds.

Thermocouples TC1-TC5 and TC21 are inserted in a channel-to-channel isolated thermocouple input module, the NI 9212. The temperature input module has 4 modes, each with a certain temperature measurement accuracy. This measurement accuracy is also specified as the measurement sensitivity according to the datasheet of the NI9212 module [16]. In general, the measurement sensitivity is a function of noise and it represents the smallest change in temperature that the sensor can detect:

- High-resolution: 0.01°C (1.8 Hz)
- Best 50 rejection: 0.02°C (7.1 Hz)
- Best 60 rejection: 0.02°C (8.3 Hz)
- High-speed: 0.05°C (95 Hz)

A trade-off has been made between sampling rate and accuracy. For this set-up there is a high requirement regarding the accuracy. Therefore, it is decided to use the high resolution mode, which result in a measurement accuracy of 0.01°C and a maximum sampling rate of 1.8 Hz for the thermocouple input module.

For TC6-TC20, standard type-T thermocouples are used and are inserted in a temperature input module NI9214.

Currently one complex problem exists in the labVIEW programming. It is only possible to log all compact DAQ's with the same sampling frequency of 1 HZ. Martin Huijzer knows to solve this problem, but this will take a few working days solve. This could be implemented in the future if a higher sampling frequency is desirable. For now a sampling frequency of 1 second is assumed to be fast enough.

### 3.4.2 Flowmeters

#### Solar Circuit

The required accuracy for measuring the flowrate is  $\pm 1$  %. It is decided to choose a flowmeter of the supplier KROHNE, since they produce flowmeters with very high accuracies in combination with a large flow range.

The measuring principle is based on measuring a Voltage which is proportional to the flow velocity in the measuring tube. The water can be seen as a electrically conductive fluid and it flows through an electrically insulated pipe through a magnetic field. This magnetic field is generated by a pair coils [23]. Then inside the fluid, a voltage  $U$  is generated and this signal voltage is picked off by electrodes and is proportional to the mean flow velocity.

In general it holds that the higher the accuracy the higher the price; therefore, a trade-off between accuracy an costs has been made. The selection of the flowmeter in the solar circuit is done based on the minimum and maximum flow of the setup. For multi-pass measurements this is 1-4 L/min,

which is based on the experience of Conico Valves b.v. and for single-pass measurements this is approximately  $>0.3$  L/min. Thus, the accuracy need to be  $<1\%$  between 0.3-4 L/min.

First, the selection has been done manually, by conduction research in all available datasheets of KROHNE. Out of this research it can be concluded that the OPTIFLUX4000 with signal converter IFC100 (i.e. OPTIFLUX4100) is the cheapest flowmeter that satisfies the requirements. Later this selection is confirmed by KROHNE itself, which uses advanced selection software. The output of the software can be found in appendix J.1 and the datasheet of the OPTIFLUX4000 and the IFC100 signal converter can be downloaded from the website of KROHNE [23] [22]. The general specifications are provided in table 3.3.

Also selections of the cheaper variant OPTIFLUX1000 have been made, but in this series the minimum diameter is DN10 instead of DN6. As a result, this type is more suitable for higher flowrates. According to the selections from the software of KROHNE, it turned out that the accuracy is 1.3% at 0.5 L/min, which does not meet the requirements.

Table 3.3: Specifications of the flowmeters in the solar circuit

Flowmeter	Type	Nominal Size	Range	Typical accuracy
[-]	[-]	[-]	[L/min]	[%]
FM1	OPTIFLUX4100	DN6	0,1-10	0,4
FM2	OPTIFLUX4100	DN6	0,1-10	0,4

Furthermore, it is highly important to emphasise that the flowmeter is currently programmed for flowrates between 0.1 and 10 L/min; however, this might be changed in the settings to 0 and 20 L/min if this is necessary in the future. It is recommended to contact KROHNE if this need to be adjusted.

Currently one flowmeter (FM1) is installed in the solar circuit to measure the flowrate. However, a second flowmeter was installed in the by-pass line of the tank to observe the switching moment of the TDV. Because of three main reasons this flowmeter is removed for the main experiments on the multi-pass system. The first reason is that the pressure drop caused by the flowmeter, influences the switching behaviour of the TDV. The second reason is that the measuring tube and the flanges of the flowmeter have a very large thermal inertia, which causes more damping in the temperature response during multi-pass mode. More damping results in flattening out the characteristic 'stair form' of the multi-pass system, which is not desired.

### Cooling circuit

The accuracy of the flowmeters in the cooling circuit are not important, since these flowrates are not necessary in the calculations and the flowrate is not needed for the PID controller to control the temperature. However, it can be useful for the user to have an indication of the flow inside the circuit.

The only requirement for this flowmeter was that it gives a current as output signal, since it needs to fit in the input module NI9203. This module was freely available at the TU/e, so this reduces the costs. Flowmeters of the type LVB-XX-A from supplier Bronckhorst meet this only requirement; therefore, it is decided to purchase these flowmeters at Bronckhorst.

Table 3.4: Specifications of the flowmeters in the cooling circuit

Flowmeter	Type	Nominal Size	Range	Accuracy ( $<0,5\dot{V}_{max}$ )	Accuracy ( $\geq0,5\dot{V}_{max}$ )
[-]	[-]	[-]	[L/min]	[L/min]	[%]
FM3	LVB-06-A	DN6	0,5-10	0,1	$< 2$
FM4	LVB-10-A	DN10	2-40	0,4	$< 2$

### 3.4.3 Instrument Control and Data Acquisition

The pumps and the heaters are inserted in a digital out module NI9472, the control valve and the electric mixing valves are inserted in a voltage out module NI9263 and all flowmeters are inserted in a analog in module NI9203.

The temperature input module NI9214 is connected to 1 slot NI CompactDAQ and the rest of the input modules are inserted in a 4 slots NI CompactDAQ. A CompactDAQ is a data acquisition platform and can be connected to a PC with LabVIEW. LabVIEW is a data acquisition program and with this program it is possible to analyze, visualize and log the measurement data. In LabVIEW there is also the possibility to control process parameters with a PID controller. Figure L.1 shows the front panel, which is designed in LabVIEW. The block diagram (back-panel) is not included.

## 3.5 Stability Testing Process Parameters

In this section the stability of the flowrate, irradiance and process temperatures are presented. Since the process temperatures are not constant, this stability is checked with consecutive steady state cycles. The stability of the flowrate and the irradiance are compared with the max deviation according to ISO 9806:2017. For the flowrate a maximum deviation of 1 % is required and for the irradiance a maximum deviation of  $50 \text{ W/m}^2$  is required. Figure 3.12 shows the stability of flowrate, with the red solid lines as 1% lower and upper bound. For each flowrate and irradiance 600 samples over a period of 10 minutes is taken; however, these signals can be hold for the entire measuring day.

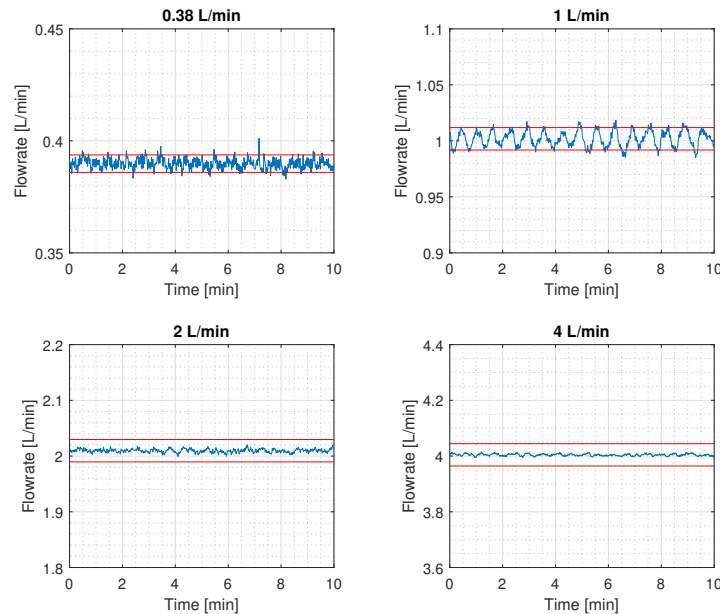


Figure 3.12: Stability flowrates of single- and multi-pass mode.

As can be observed, the flowrate falls within the limits. At lower flowrates some peaks cross the bounds, but this effect is assumed to be negligible.

Figure 3.13 shows the stability of the irradiance. As can be observed, the signal never exceeds the limits, so this requirement is also met.

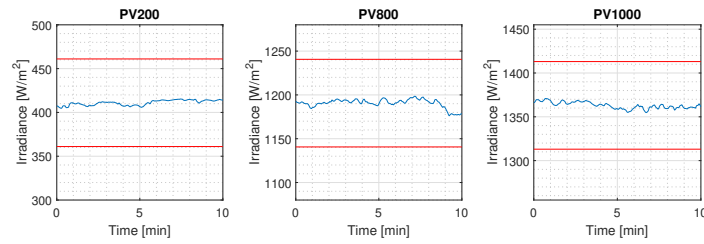


Figure 3.13: Stability irradiance of all PV settings

Finally, the stability of the consecutive steady state cycles is shown in figure 3.14. A total period of 1 hour is used. As can be seen all cycles are identical, so it can be concluded that this set-up is able to handle consecutive steady state cycles.

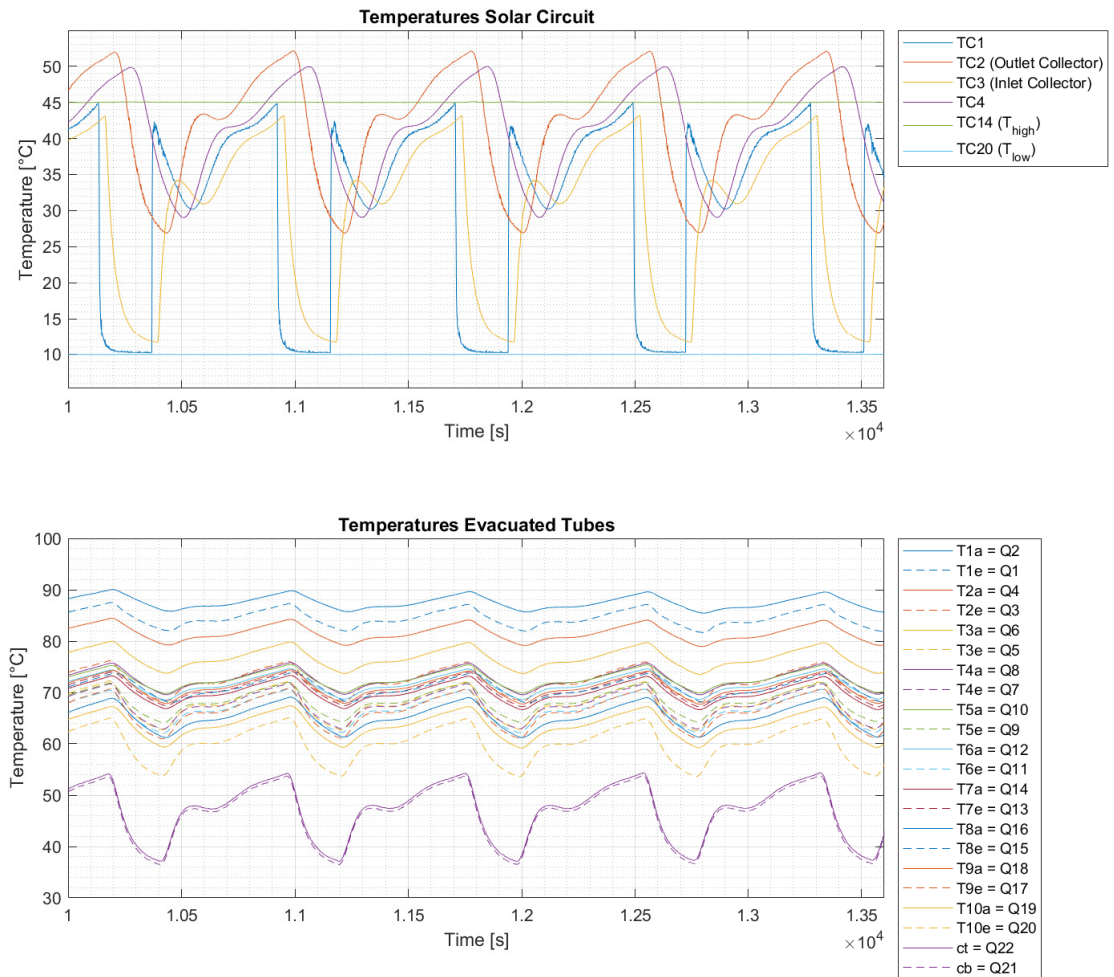


Figure 3.14: Stability consecutive steady state cycles during 1 hour

## 3.6 Calibration

When performing temperature measurements it is important to take into account the uncertainties of the total set-up. The total uncertainty of the set-up is composed by different errors, as explained in section 3.7. A large amount of the total uncertainty is caused by systematic errors in the set-up. This error can rise significantly in one measurement chain, because all uncertainties of each component in the measuring chain needs to be added. Each component has its own accuracy that contributes to the total systematic error.

To reduce the total uncertainty, it is necessary to minimize the systematic errors. This can be realized by proper calibration. After calibration the total systematic error is reduced to the systematic error of the calibration set-up.

### 3.6.1 Calibration thermocouples new set-up

For the calibration of all thermocouples a thermostatic bath is used. The thermostatic bath can control the average temperature inside the bath very accurately in the range between ambient temperature and 90°C. Is also used a pump to circulate the water, to ensure that the bath is at a homogeneous temperature. According to Van Duijnhoven [10] and Degenhart [9] the homogeneity of thermal bath is 0.1°C. The thermostatic bath is filled such that the heating element is submerged entirely and that the pump doesn't pump air bubbles.

All thermocouples are bundled together as close as possible and are subsequently submerged in the water approximately 5cm deep. As mentioned in section 3.4.1 TC1-TC5 and TC21 are connected to a NI9212 module and TC6-TC20 are connected to a NI9214 module. In addition, a calibrated thermocouple (Type-K) is added to the thermocouple bundle and is used as reference temperature. This calibrated thermocouple is connected to a readout device (Memocal 2000).

The program that is used for the calibration is NI MAX. This is a software tool that provides access to the NI hardware and is connected to LabVIEW. So after the calibration is performed and the calibration is enabled, LabVIEW uses the calibrated values automatically, so no additional data manipulation is necessary. A standard calibration procedure of NI MAX is used corresponding to the settings of the input module. This means that a standard sampling frequency of 1.8 Hz, with a total amount of samples of 9 is used. NI MAX uses linear interpolation instead of using a linear trendline of all datapoints.

The calibration points that are used can be found in table X D.2, D.3 D.4 and D.5. In these tables, the coefficients for the linear trendline and the  $R^2$  are also given. For 0°C a thermos bottle with ice water is used. And for the other temperatures, the temperature of the thermostatic bath is set to the desired value. Each time 15 minutes have to we waited in order to stabilize the thermostatic bath.

The in-homogeneity of the thermostatic bath is assumed to be 0.05°C, see section 3.7 for further explanation. Therefore, some calibration points can be deviate slightly from the linear trendline. For all cases the  $R^2$  is higher or equal to 0.999, which means that reliability of each fit is very high.

However, the influence of the in-homogeneity of the thermostatic bath can be observed better when subtracting 2 thermocouple. In figure 3.15 the uncalibrated in- outlet temperatures of the collector are subtracted from each other. Subtracting 2 linear lines, should also result in a linear line. This trend can clearly be observed in figure 3.15. However, at 0°C, 80°C and 90°C the temperature difference's of the uncalibrated thermocouples deviate more from the linear trendline then the other measuring points. It can be concluded that the in-homogeneity of the thermal bath is higher at these temperatures. Still it is in the same order of magnitude as an expected inhomogeneity of 0.05°C.

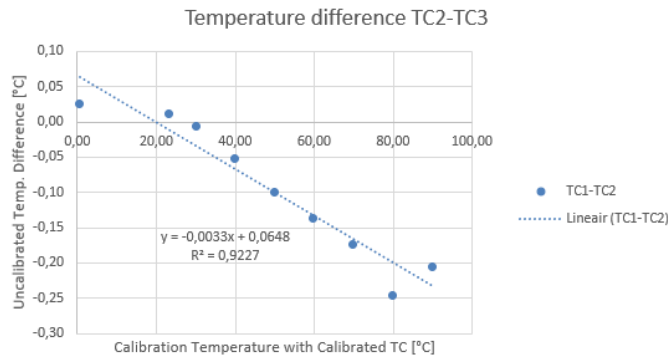


Figure 3.15: Calibration data of temperature difference of the in- (TC3) and outlet (TC2) collector

### Recommendation

During the calibration procedure it turned out that the thermocouples with 0.5mm tip are very sensitive to temperature fluctuations. Therefore, it is highly important to close the lid of the bath and to seal the gaps with aluminum tape in order to maintain a very constant temperature and to reduce the heat losses to the environment. Finally, to reduce the inhomogeneity it is recommended to place the thermocouple bundle as deep as possible, far away from the heater.

Also the water mixed with ice tend to have a larger inhomogeneity than the thermostatic bath. This is also recently observed by a lab technician Theo the Groot. His findings are not yet published, but he observed that the temperature near the ice fluctuates. He recommends to use a large amount cold water from the fridge at approximately 1°C.

## 3.6.2 Calibration remaining sensors

### Thermocouples old set-up

The thermocouples which were already present in the current set-up are calibrated by Degenhart [9]. These sensors are the ambient temperature sensors and the thermocouples inside one evacuated tube. The calibration procedure is performed with the same thermostatic bath, but in this time there was no calibrated thermocouple available; therefore, the internal sensor of the thermostatic bath was used.

### Flowmeters

The flowmeters in the solar circuit (FM1 and FM2) are calibrated by the supplier (KROHNE). The accuracy of the flowmeters are function of flow velocity and is specified in table J.1 in the appendix. The calibration certificates are stored in the Lab at a safe place.

The calibration procedure is based on direct volume comparison. The accuracy limits of electromagnetic flowmeters are typically the result of the combined effect of linearity, zero point stability and calibration uncertainty.

The flowmeters in the cooling circuit (FM3 and FM4) are also calibrated by the supplier (Bronckhorst). As mentioned in section 3.4.2, the accuracy of these flowmeters is irrelevant and thus no calibration report is available.

### Pyranometer

The calibration report of the pyranometer can be found in figure J.2 in the appendix and is based upon indoor side by side comparison.

## 3.7 Uncertainty Measuring Equipment

In this uncertainty analysis the uncertainties of the measuring equipment of the experimental set-up are analysed. The analysis is done by taking into account Type A and Type B uncertainties. A Type A uncertainty is also known as the random error and can be determined statistically. A type B uncertainty is also known as a systematic error and is characterised by the measuring instruments. The latter can be determined according the specifications of the measuring instruments. The calculation method of type A and Type B uncertainties are presented in section E.1 and E.2 of appendix E.

In addition, there are uncertainties which can not be quantified in most cases. Such uncertainties depend on the quality of the testing method. For example, the measurement of the ambient temperature. This temperature is determined by taking the average of 4 sensors at different locations. It is assumed that these 4 sensors represent the true ambient temperature around the collector, but it might be that is not entirely correct. These uncertainties are not incorporated in the uncertainty analysis, unless it is stated specifically. In cases this type of uncertainty is excluded, it is assumed that the testing method, which is based on ISO 9806, is reliable enough.

It is highly important to define which confidence interval is needed for a certain type of uncertainty. In general there exists a standard combined uncertainty, which has a confidence interval of 68.3% and an expanded combined uncertainty, which has a confidence interval of 95.5%. In some research these two types of uncertainties are being confused with one another. Even the ISO 9806 does not explicitly state which confidence interval is required. However, in research concerning measurements to solar collectors the expanded combined uncertainty is almost always used. This is among other things confirmed by Kratzenberg et al. (2006) [5], Mathioulakis et al. (1999) [3] and Van den Heuvel (2018) [15]. Based on these findings it is decided to use the expanded uncertainty in this research. Degenhart (2020) [9] also states that a confidence interval of 95.5% is required; however, he only uses a this confidence interval for the random error and the uncertainty of the pyranometer, for all other uncertainties he uses the standard combined uncertainty with 68.3% confidence interval. Therefore, it might be that some uncertainties in this research are higher.

The total uncertainty of all derived quantities, for example the thermal efficiency, are analysed in section 4.1.6 and 4.2.5; the calculation method of the derived quantities are presented in appendix E.

### 3.7.1 Pyranometer

For measuring the irradiance of the solar simulator a pyranometer of the type Kipp & Zonen CM11 is used. The pyranometer is provided with a thermal detector which responds to the total amount of incoming radiant energy. First, the radiant energy is absorbed by a black painted disk. Second, the heat which is generated flows through a thermal resistance to the body of the pyranometer, which acts as heat sink. Then, the temperature difference across the thermal resistance is converted into a voltage ( $U$  in  $\mu\text{V}$ ). Finally, this voltage is sent to a voltage input module NI9212. This module is normally used to read a voltage of a thermocouple, but can also be used to read a voltage from other measurement instruments. In NI MAX the voltage is translated into an irradiance ( $G$ ) using a sensitivity ( $S$ ) of  $4.99 \mu\text{V}/\text{W}/\text{m}^2$ , see equation (3.1):

$$G = \frac{U}{S} \quad (3.1)$$

All contributing uncertainties of the pyranometer will be explained briefly and are presented in table 3.5. The standard combined uncertainty and the expanded combined uncertainty are calculated by using equation (E.4) and (E.7) respectively.

In the calibration certificate of the pyranometer it is stated that the expanded uncertainty due to random effects and the systematic error of the calibration set-up is  $\pm 1.29\%$ . These systematic

errors are for example: directional response, tilt response, offset due to long wave radiation, offset due to changes in ambient temperature, non linearity and spectral selectivity [34]. It is also stated that expanded uncertainty of the calibration procedure (calibration by comparison with a reference pyranometer) is equal to  $\pm 0.5\%$ .

In the manual of the pyranometer it is stated that the transducer of the pyranometer is drifting over time, which means that the sensitivity of the pyranometer may change  $\pm 0.5\%$  per year. Therefore, it is highly recommended that the pyranometer will be calibrated each year. Since the pyranometer is calibrated 1.5 year ago, this uncertainty is assumed to be 1.5 times higher, resulting in an accuracy of  $\pm 0.75\%$ .

The accuracy of the input module is only specified in degree Celsius and not in voltage, since this module normally is being used for thermocouples. In order to determine the accuracy in  $\text{W/m}^2$ , the accuracy is converted back into a voltage [V] en then again converted into  $\text{W/m}^2$  with equation 3.1. This method is used in accordance with lab technicians. The measurement accuracy of this input module is typical  $\pm 0.39^\circ\text{C}$  for a type T thermocouple. According to the reference table of this type thermocouple [30] the sensitivity is  $\cdot 10^{-3} \text{ V}/^\circ\text{C}$  at  $20^\circ\text{C}$ . By using both sensitivities, the accuracy in  $\text{W/m}^2$  can be calculated, resulting in an accuracy of  $\pm 3.13 \text{ W/m}^2$ . The same procedure is done for the resolution of the input module, which specified as  $0.01^\circ\text{C}$  and can be converted into  $0.08 \text{ W/m}^2$ .

The pyranometer is placed on one position next to the solar collector at 10cm distance of the solar simulator. The solar simulator does not give a perfect uniform irradiance; therefore, one measuring position of the irradiance does not perfectly represent the actual irradiance. Therefore, an extra uncertainty regarding the non-uniformity is included. In the calibration report of the solar simulator the the non-uniformity is given for each setting: 4.36% for the PV200 setting is, 1.51% for the PV800 setting and 1.81% for the PV1000 setting.

Table 3.5: Uncertainties of the pyranomator at settings PV200 ( $407 \text{ W/m}^2$ ), PV800 ( $1186 \text{ W/m}^2$ ) and PV800 ( $1365 \text{ W/m}^2$ )

Type uncertainty	Accuracy	Divisor	$u$ PV200 [ $\text{W/m}^2$ ]	$u$ PV800 [ $\text{W/m}^2$ ]	$u$ PV1000 [ $\text{W/m}^2$ ]
Random effects and systematic error	1,29 %	2	2,63	7,65	8,80
Calibration by comparison	0,5 %	2	1,02	2,97	3,41
Long term drift	0,75 %	$\sqrt{3}$	1,76	5,14	5,91
Voltage input module	$3,13 \text{ W/m}^2$	$\sqrt{3}$	1,80	1,80	1,80
Resolution	$0,08 \text{ W/m}^2$	1	0,08	0,08	0,08
Non-uniformity	4,36 / 1,51 / 1,81%	$\sqrt{3}$	10,25	10,34	14,26
<b>Standard combined uncertainty</b>			10,92	14,28	18,19
<b>Expanded combined uncertainty</b>			21,84	28,56	36,38

### 3.7.2 Flowmeters

The accuracy of flowmeters FM1 and FM2 are specified by KROHNE. In section J.1 an overview of all specifications for the total flow range is presented. Table 3.6 shows the uncertainties for the main operating flow rates.

Flowmeters FM1 and FM2 are inserted in an NI9203 analog input module. The systematic error



of this input module is eliminated by translating the output signal. This is done by monitoring the flowrate when there was no flow. The output signal should be 0 L/min in this case; however, it is observed that there was a minimum offset of  $-1.33 \cdot 10^{-3}$  L/min. Therefore, the output signal was translated with  $1.33 \cdot 10^{-3}$  L/min in positive direction in order to eliminate the offset.

The repeatability of the flowmeters FM1 en FM2 is  $\pm 0.1\%$ .

Table 3.6: Standard combined uncertainties and expanded combined uncertainties of the flowrate.

Flowrate	Accuracy	Divisor	$u_{std}$	$u_{exp}$
[L/min]	[%]	[-]	[L/min]	[L/min]
0,3	0,97	$\sqrt{3}$	$1.68 \cdot 10^{-3}$	$3.36 \cdot 10^{-3}$
1	0,57	$\sqrt{3}$	$3.29 \cdot 10^{-3}$	$6.58 \cdot 10^{-3}$
2	0,48	$\sqrt{3}$	$5.54 \cdot 10^{-3}$	$1.11 \cdot 10^{-2}$
4	0,44	$\sqrt{3}$	$1.02 \cdot 10^{-2}$	$2.03 \cdot 10^{-2}$

The calculation of the uncertainty of flowmeters FM3 and FM4 are not included in this section, because the accuracy is irrelevant, as mentioned in section 3.4.2.

### 3.7.3 Thermocouples

In table 3.7 an overview of all contributing uncertainties are presented for a type T thermocouple. It includes all uncertainties in the calibration chain and the resolution of the NI9212 temperature input module of the set-up, which is  $0.01^\circ\text{C}$ .

During calibration it turned out that the random error was almost negligible, because it was never higher than  $\pm 1 \cdot 10^{-3}$  in each measurement set. Therefore, it is decided not to show all different random errors for each thermocouple. Instead the maximum random error of  $\pm 1 \cdot 10^{-3}$  is used for all thermocouples.

The inhomogeneity of the thermostatic bath is assumed to be  $0.05^\circ\text{C}$ , which is stated by Van den Heuvel [15] and Degenhart [9]. The reference thermocouple, has an accuracy of  $\pm 0.36^\circ\text{C}$ . Furthermore, the input module of the calibrator has some inaccuracies. According to the manual of the Memocal 2000 the total uncertainty of this device can be specified by 2 accuracy, namely: the accuracy of the cold junction and the accuracy of the internal thermocouple readout electronics. The final uncertainty regarding the calibrator is the resolution of the display, which is  $0.05^\circ\text{C}$ .

Table 3.7: Uncertainties of the thermocouples in the new set-up

Type uncertainty	Accuracy	Divisor	$u$
	$[\circ\text{C}]$	[-]	$[\circ\text{C}]$
Random error calibration			$1 \cdot 10^{-3}$
Inhomogeneity thermostatic bath	0,05	1	0,05
Resolution temperature input module	0,01	1	0,01
Reference thermocouple calibrator	0,36	$\sqrt{3}$	0,21
Cold junction calibrator	0,4	$\sqrt{3}$	0,23
Internal readout electronics calibrator	0,3	$\sqrt{3}$	0,17
Resolution calibrator	0,05	1	0,05
<b>Standard combined uncertainty</b>			0,36
<b>Expanded combined uncertainty</b>			0,73

### 3.7.4 Temperature difference

As can be seen in table 3.7 the expanded combined uncertainty is quite high. However, for the calculation of the uncertainties of temperature differences all systematic errors of the calibration setup can be cancelled out, because these errors are the same (and in the same direction) for both thermocouples. This increases the accuracy of temperature differences significantly. In table 3.8 the uncertainties are presented regarding temperature differences of the thermocouples in the new set-up. Since 2 thermocouples are involved to calculate a temperature differences, all uncertainties are included twice to calculate the standard combined uncertainty. For this calculation the law of error propagation is used, see equation (E.5).

Table 3.8: Uncertainties regarding a temperature difference of type T thermocouples.

Type uncertainty	Accuracy	Divisor	$u$
	[°C]	[-]	[°C]
Random error calibration (2x)			$1 \cdot 10^{-3}$
Inhomogeneity thermostatic bath (2x)	0,05	1	0,05
Resolution temperature input module (2x)	0,01	1	0,01
<b>Standard combined uncertainty</b>			0,072
<b>Expanded combined uncertainty</b>			0,14

### 3.7.5 Comparison with ISO 9806

Table 3.9 shows the comparison with the ISO 9806 norm. It can be concluded that all requirements are met, except of the requirement for the temperature difference. The uncertainty regarding the temperature difference is determined by the quality of the calibration set-up. So if it is required to lower this uncertainty in the future another calibration set-up need to be used, such as a high quality calibration oven. Lab Technicians are currently conducting some research to realize this in the future.

The sensors regarding the ambient temperature are calibrated by Degenhart and the uncertainty was  $\pm 0.04^\circ\text{C}$ . Since Degenhart used the standard combined uncertainty instead of the expanded combined uncertainty an uncertainty of  $\pm 0.08^\circ\text{C}$  is used.

Table 3.9: Required accuracy or uncertainty and the actual realized uncertainty.

Process Parameter	Required Accuracy	Realized Uncertainty/Accuracy
$\dot{V}$ [L/min]	std. uncertainty < $\pm 1\%$	$\pm 0.97-0.44\%$
G	Class 1 pyranometer or better; ISO 9060	< $\pm 36.4 \text{ W/m}^2$
$T_{in}$	see $\Delta T$	$\pm 0,73^\circ\text{C}$
$T_{out}$	see $\Delta T$	$\pm 0,73^\circ\text{C}$
$\Delta T$	Accuracy < 1% std. uncertainty < $0.05^\circ\text{C}$	$\pm 0.14^\circ\text{C}$
$T_{amb}$	std. uncertainty < $0.5^\circ\text{C}$	$\pm 0,08^\circ\text{C}$

# Chapter 4

## Experimental Research

All measurements for single- and multi-pass mode are carried out with a tilt angle of 45°.

### 4.1 Multi-pass

#### 4.1.1 Method

In table 4.1 an overview of the measurement plan of the multi-pass mode is presented. The information in this table is explained in depth in this section.

As explained briefly in chapter 1, there are four parameters which influences the dynamical response of the multi-pass system, namely: flowrate, irradiance and both temperature zones of the tank  $T_{low}$  and  $T_{high}$ . This temperature difference is called the tank temperature difference ( $\Delta T_t$ ).

Table 4.1: Measurement (M.) plan multi-pass mode in order to determine the optical efficiency.

<b>M.</b>	<b>Irradiance</b>	$T_{low}$	$\Delta T_t$	<b>Flowrate</b>
[nr.]	[W/m <sup>2</sup> K]	[°C]	[°C]	[L/min]
1	PV200 = ± 400	10	35	1
2				2
3				4
4	PV800 = ± 1200	10	35	1
5				2
6				4
7	PV1000 = ± 1400	10	35	1
8				2
9				4
10	PV800 = ± 1200	20	20	1
11				2
12				4

According to the solar Keymark certificate F.2 and ISO 9806:2017 the normal operation condition of the collector is 0.02 kg/s per gross collector area, which is 1.8 L/min. Degenhart [9] rounded this value to 2 L/min to determine the collector coefficients. Therefore, it is decided to include this flowrate in the measuring range. According to Conico Valves bv. flowrates below 1 L/min are not recommended for the multi-pass mode, therefore the minimum value of 1 L/min is also used. The maximum flowrate that is used in the measuring range is 4 L/min, simply be obtained by taking the double value of the normal operation. 2 L/min can be considered as a relative high flowrate and 4 L/min can be considered as a high flowrate. Higher flowrates are not recommended with this set-up, because then the temperature difference across the collector becomes too low, causing high uncertainty.

For the irradiance, 3 settings of the solar simulator with different irradiance are used, namely PV200 (±400 W/m<sup>2</sup>m), PV800 (±1200 W/m<sup>2</sup>) and PV1000 (±1400 W/m<sup>2</sup>). Although ISO 9806:2017 recommends a minimum irradiance of 700 W/m<sup>2</sup>, the PV200 setting is still included in the measuring range in order to study the temperature response inside the evacuated tubes. According to Degenhart [9] the efficiency slightly decreases if the irradiance decreases. He compared

his theoretical approach with experimental results of Apricus [13]. They concluded that the efficiency decreases with 2% if the irradiance was lowered from 900 W/m<sup>2</sup> to 200 W/m<sup>2</sup>. According to this research the decrease in efficiency was due the presence of non-condensable gases at lower heat transfer rates.

These measurements were conducted at fully steady states conditions. However, during multi-pass mode the process temperature are clearly not steady state. The irradiance has influence on the dynamic temperature response of the heatpipes and thus also indirectly on the outlet and inlet temperature, since there exists multiple loops during multi-pass mode. For a low irradiance the periodically temperature increase is expected to be lower since the thermal power is lower. Therefore, the total amount of loops the HTF needs to run is higher, which increases the total cycle time. The total cycle time might have influence on the total thermal efficiency of the system; therefore, it is decided to also study the effect off different irradiances PV200, PV800 and PV1000.

For  $\Delta T_t$  it is decided to take one high temperature difference and one low temperature difference. In consultation with Conico Valves a temperature difference of 30-40°C is considered as high operation temperature difference and 20°C is considered as a relative low operation temperature difference; therefore, the temperature differences of 20°C and 35°C are included in the measurement plan.

For  $\Delta T_t = 35^\circ\text{C}$  the minimum possible value of 10°C is chosen for  $T_{low}$  in order to ensure that  $T_m$  is as close as possible to  $T_a$  and  $T_{red}$  is almost 0. The closer  $T_{red}$  is to zero, the closer the thermal efficiency is to the optical efficiency, see chapter 2. The expected  $T_m$  is around 30°C; therefore, a  $T_{low}$  of 20°C for a  $\Delta T_t$  of 20°C is chosen to approach a  $T_m$  of 30°C as close as possible (rough estimation of  $(T_{low} + T_{high})/2$ ).

In general it is desired to compare thermal efficiencies at the same temperature difference between  $T_m$  and  $T_a$ , to make a fair comparison. However, in practice this is not possible because  $T_m$  is different for different flowrates and the ambient temperature is not always the same. Therefore, in order to compare the thermal efficiencies of different operation conditions, the optical efficiency will be calculated. With the optical efficiency it is possible to compare thermal efficiencies at  $T_{red} = 0$ . The definition of  $T_{red}$  is described in section 2.2.

#### Calculation method thermal efficiency total system

The thermal- and optical efficiency of the collector can be calculated with equation 2.3 and 2.9. However, the calculation of the thermal efficiency for the total system (or the tank) in multi-pass mode should be determined slightly different, since the tank is charged periodically instead of constant. Therefore, two variables are introduced, namely: the total cycle time ( $\Delta t_{cycle}$ ) and the total charging time ( $\Delta t_{charging}$ ).  $\Delta t_{cycle}$  is defined by the start of the cycle ( $t_1$ ) and the end of the cycle ( $t_3$ ), see equation 4.1.  $\Delta t_{charging}$  is defined by  $t_1$  and the end of charging ( $t_2$ ), see equation (4.2).  $t_1$  and  $t_3$  are determined with sensor TC21, because this sensor is able to detect a cold flow, coming from the tank, very accurately (This is the moment when the TDV opens and the tank will be charged).  $t_2$  is determined with sensor TC1, since this gradient is higher and therefore easier to capture during post processing. During charging the tank, still hot water is present in the by-pass line. When the TDV closes again, sensor TC1 is able to detect when the hot water from the by-pass is starting to flow again. TC1 is mounted on a 1 cm distance from the by-pass and the time it takes for the fluid to travel this distance is neglected. TC21 is placed directly at the outlet of the tank.

$$\Delta t_{cycle} = t_3 - t_1 \quad (4.1)$$

$$\Delta t_{charging} = t_2 - t_1 \quad (4.2)$$

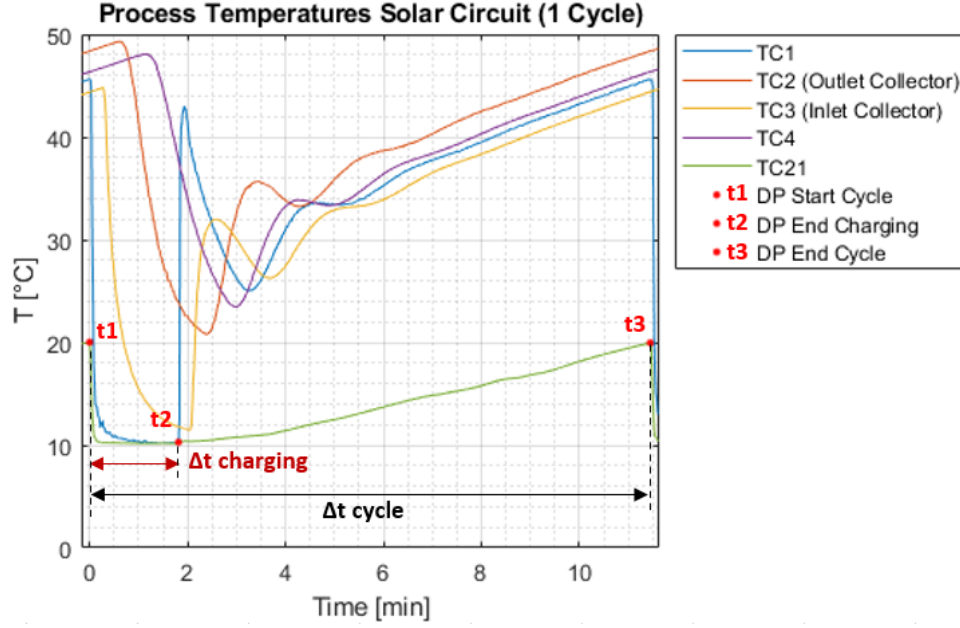


Figure 4.1: Definition of the start of the cycle ( $t_1$ ), end of charging ( $t_2$ ) and the end of the cycle ( $t_3$ )

Then the total energy gain of the tank can be calculated with (4.3)

$$E_t = \dot{Q}_t \Delta t_{charging} \quad (4.3)$$

Where the thermal power of the tank  $\dot{Q}_t$  is defined by equation (4.4).

$$\dot{Q}_t = \dot{m} c_p \Delta T_t \quad (4.4)$$

Furthermore, the total amount of incoming energy  $E_{c,in}$  is calculated with equation (4.5).

$$E_{c,in} = \dot{Q}_{c,in} \Delta t_{cycle} \quad (4.5)$$

Where  $\dot{Q}_{c,in}$  can be calculated with equation (2.1).

Finally, the thermal efficiency of the total system can be calculated with equation (4.6).

$$\eta_{th,tot} = \frac{E_t}{E_{c,in}} \quad (4.6)$$

#### Calculation method heat loss piping

The heat loss of the piping during single-pass mode can simply be calculated equation 4.1.1.

$$\dot{Q}_{loss} = \dot{Q}_{c,out} - \dot{Q}_t \quad (4.7)$$

However, the heat loss of the multi-pass mode can not be simply calculated with , since the tank is charged periodically instead of constant. Therefore, the heat loss is calculated with the total energy gain of the tank ( $E_t$ ) and the collector ( $E_{c,out}$ ) during one cycle.

$$E_{c,out} = \dot{Q}_{c,out} \Delta t_{cycle} \quad (4.8)$$

$$\dot{Q}_{loss} = \frac{E_{c,out} - E_t}{\Delta t_{cycle}} \quad (4.9)$$

### 4.1.2 Measuring procedure

The first step is to make sure that no air is trapped in the manifold of the collector. This is highly important, because the collector needs sometimes to be disconnected from the set-up and during the dismounting- and mounting process air enters the system. The air can be removed by pumping the water with maximum flowrate (10 L/min) trough the collector and to ensure that the water enters the tank via TC5. For safety it is recommended to hold this flowrate for 5 minutes to make sure all the air can collect at the top op the tank an can be released by the air relieve valve. When doing this,  $T_{low}$  and  $T_{high}$  mixes up; therefore, it is highly recommended to do this in the first place!

Then the high temperature zone ( $T_{high}$ ) needs to heat up to the desired temperature. Both heaters of 3 kW each are able to heat up this part of the tank with 22.5°C per hour. At the same time the cooling circuit can cool the low temperature zone ( $T_{low}$ ) of the tank. When a temperature of 10°C is required this may take a couple of hours, since the minimum supply temperature of the cooling circuit is around 9°C. At higher temperatures this will be considerably faster.

Approximately 30 minutes before  $T_{low}$  and  $T_{high}$  are expected to reach the desired temperature the solar simulator can be turned on the right setting. It takes approximately 20 minutes before the irradiance is stabilized. In the meantime the flowrate control can be set on "valve control" with the desired setpoint, which means that the flow will be controlled by CV instead of the PWM signal of the pump. Then a minimum of 45-60 minutes need to be waited in order to achieve a periodically steady state condition. This is normally after a couple of cycles, see 3.14. When periodically steady state is achieved a number of samples is taken with 1 HZ sampling rate. The number of samples depends of the total cycle time.

After the measurements are being logged and saved a new flowrate can be set manually. It is possible to conduct approximately 3 different flowrates per day. All measuring days are started with 1 L/min, followed by 2- and 4 L/min. At one measuring day it is possible to measure 3 or 4 flowrates in total. Furthermore, it is recommended to only change the flowrate of the irradiance at one day, because changing  $T_{low}$  or  $T_{high}$  takes to long.

Due to the low required thermal power of the top spiral heat exchanger it is recommended to use the lowest PWM setting of 2 for PMP2. In some cases the heat exchanger still extracts more heat than desired; therefore, the heater is set to automatic control with setpoint 45°C. Then, the temperature of  $T_{high}$  can be controlled steady.

The settings of the PID parameters can be found in table 4.2 for EMV1, EMV2 and CV. All PID parameters are determined by trial and error. During multi-pass experiments the manual control valve MCV is always fully open (position 5.0). Furtermore, the settings for the pumps and the manual control valve are given in table 4.3.

Table 4.2: Settings of PID parameters for multi-pass mode

<b>PID Parameters</b>	<b>EMV1</b>	<b>EMV2</b>	<b>CV</b>	<b>Unit</b>
$K_c$	0,025	0,025	0,025	[-]
$\tau_i$	0,02	0,02	0,02	[min]
$\tau_d$	0,02	0,02	0,02	[min]

Table 4.3: Settings for all three pumps and the MCV for multi-pass mode. The flowrate in this table corresponds to the flowrate of the solar circuit, thus the settings of PMP2 and PMP3 are independent of that flowrate.

<b>Flowrate</b>	<b>PMP1 PWM</b>	<b>PMP2 PWM</b>	<b>PMP3 PWM</b>	<b>MCV</b>
[L/min]	[-]	[-]	[-]	[-]
1	2	2	10	5.0
2	5	2	10	5.0
4	20	2	10	5.0

### 4.1.3 Results Process Temperatures

The top three sub-figures in figure 4.2 show an overview of all process temperatures in the multi-pass system during 1 cycle for 1, 2 and 4 L/min respectively for PV1000. The results of PV200 and PV800 are presented in appendix B.2. The bottom three sub-figures show an overview of all temperatures inside the first evacuated tube, where the solid lines represent the absorber temperatures and dashed lines represent the evaporator temperatures. At  $t = 0$ , the TDV has been opened and the tank is being charged. The charge time is 249s, 112s and 56s for the flowrates 1, 2 and 4 L/min respectively. The cycle time is 718, 596 and 554 s respectively.

#### Evaluation process temperatures collector loop

In all three cases it can be observed that the first time, the cold stream flows through the collector, the temperature increase is the highest. This is due to the high effective thermal capacity of the collector. At flowrates of 2 L/min and higher it can be observed that the temperature response dampens out after approximately 3 collector loops (at  $t = 400$ s for 2 L/min and at  $t = 200$ s for 4 L/min), which is caused by the thermal capacity of the piping and components. If the thermal capacity of the piping and the components has been lower, this dampening would have been less.

#### Evaluation temperature overshoot

Although  $T_{high}$  is 45°C it can be observed that TC2 (outlet temperature of the collector) and TC4 (inlet temperature of the TDV) becomes higher during charging the tank. This temperature overshoot is clearly higher at lower flowrates, which is due to the higher temperature difference over the collector and the higher loop time (the time that 1 fluid particle need to travel 1 collector loop). This can be explained as followed: when the TDV opens, the last particle in the fluid loop increases more before it enters the tank, due to the higher temperature difference over the collector. The higher the temperature overshoot, the higher the average temperature of the collector, which might result in a lower thermal efficiency of the collector. Therefore, it is recommended to prevent high temperature overshoots.

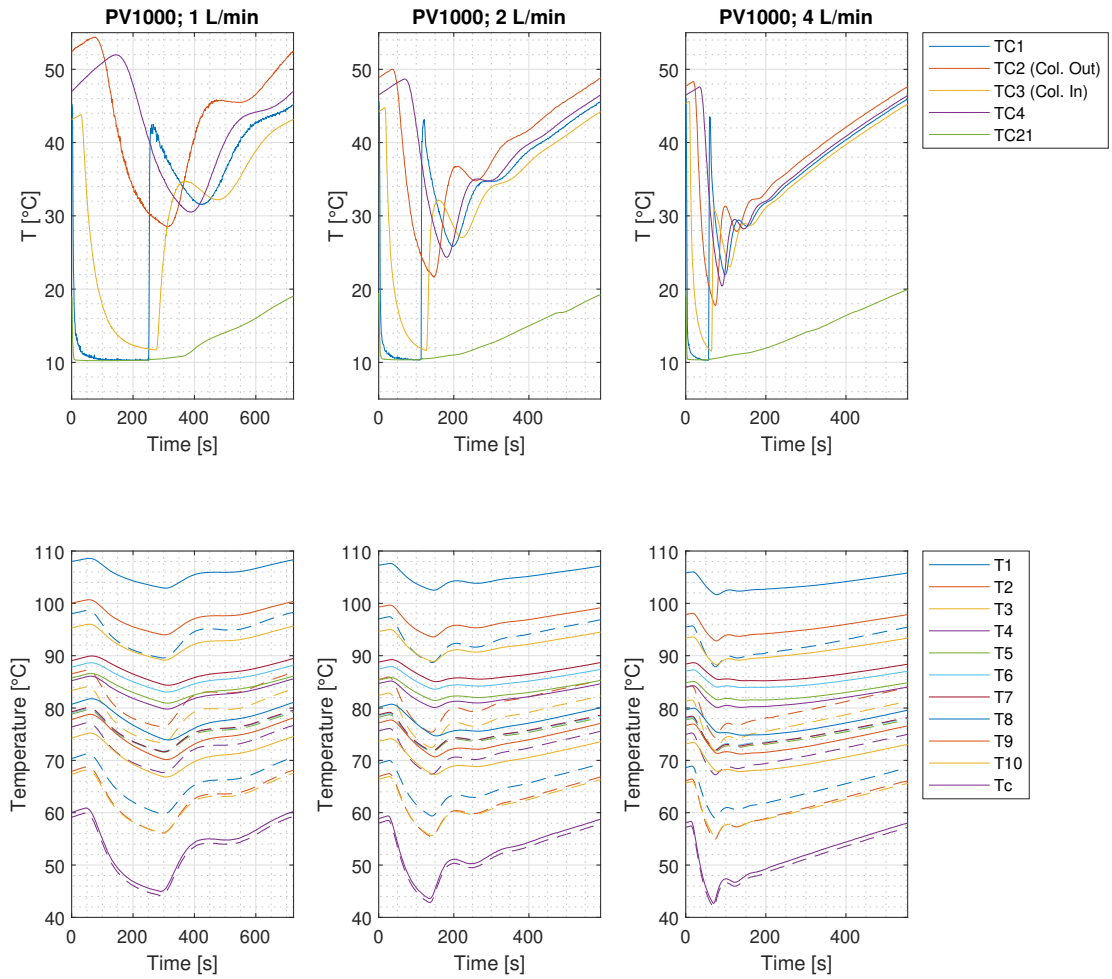


Figure 4.2: Top: Process temperatures Solar Circuit. Bottom: Temperatures inside first evacuated tube, solid lines are absorber temperatures and dashed lines are evaporator temperatures. Conditions: PV1000,  $T_{low} = 10^{\circ}\text{C}$ ,  $T_{high} = 45^{\circ}\text{C}$



#### **Evaluation temperatures inside evacuated tube**

The temperature overshoot also influences the temperature in the evacuated tubes. At lower flowrates it can clearly be observed that the temperature increase between  $t = 0$  and the maximum temperature of the temperature of the condensor ( $T_c$ ) is higher than at higher flowrates. It can also be observed that temperature line lies slightly lower for higher flowrates, which indicates that also the average temperature of the absorber might be is slightly lower, causing in a higher efficiency for higher flowrates. This can also be observed in figure 4.7. This figure shows the average temperature over the entire cycle. The average temperature difference between 1 and 4 L/min is approximately 1-2°C over the entire length of the evacuated tube. The difference between the minimum temperatures of the condensor between 1 and 4 L/min is 2.25°C.

#### **Global comparison with TRNSYS**

When comparing the temperature response of TC2 and TC3 with an arbitrary output of TRNSYS, see figure C.1 it can be concluded that the these two thermal capacities causes the difference between the temperature response of the set-up and the model. So this has to be kept in mind when using TRNSYS.

### 4.1.4 Thermal Efficiency Total System

As mentioned before, the thermal efficiency of the total system also includes the heat losses of the piping to the environment

In figure 4.3 four plots are presented with the thermal efficiency of the the total system versus the flowrate. Also the error bars (expanded combined uncertainty) are included. The error bars are approximately equivalent for all types of efficiencies; therefore, the error bars are only explained for 1 type (the optical efficiency), see section 4.1.6. In each sub-plot an overview of the measuring days (MD) are presented.

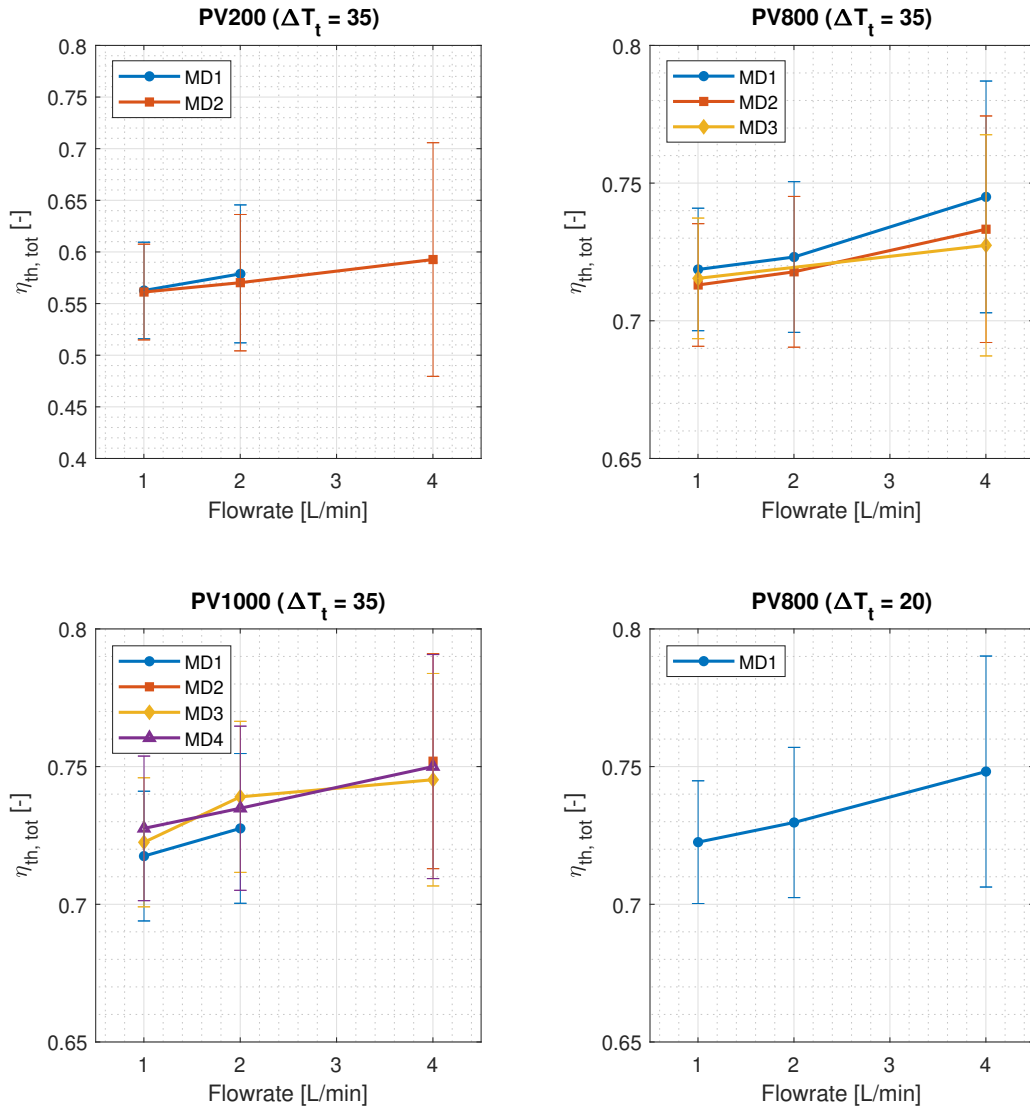


Figure 4.3: Thermal efficiency total system vs. flowrate for multi-pass mode. For  $\Delta T_t = 35^\circ\text{C}$  a  $T_{low}$  of  $10^\circ\text{C}$  is used and for  $\Delta T_t = 20^\circ\text{C}$  a  $T_{low}$  of  $20^\circ\text{C}$  is used.

In general it can be observed that the total thermal efficiency increases in all cases when increasing the flowrate, which was already expected for single pass mode, according to literature and steady

state experiments of Degenhart. This is now also confirmed for multi-pass mode.

As can be observed for PV1000, at MD1 the total thermal efficiency of the system is lower, which is caused by the lower ambient temperatures of the collector and the set-up and thus higher heat losses, see table B.2 in the appendix.

The average heat loss of the piping for PV800 and PV1000 are equivalent; however, the heat loss of the piping during PV200 is approximately twice as much compared to PV800 or PV1000, which is due to the much higher average temperature of the system. Therefore, the thermal efficiency of the total system is considerably lower for PV200.

### 4.1.5 Optical Efficiency Collector

The optical efficiency is derived from the thermal efficiency of the collector. The graphs of the thermal efficiency can be found in appendix B.3 and are used to support the findings for the optical efficiency.

In figure 4.4 four plots are presented with the optical efficiency versus the flowrate. Also the error bars (expanded combined uncertainty) for the optical efficiency are included. The error bars are further explained in the next section. In each sub-plot an overview of the measuring days (MD) are presented.

When you compare the thermal efficiency and the optical efficiency, the following can be concluded: The shape of all curves and the position with respect to each other are similar. The values for the optical efficiency are only corrected with  $T_{red}$ . Since  $T_{red}$  is higher for PV200 comparing to PV800 and PV1000, the optical efficiency for PV200 is corrected with an higher amount.

For PV800 and PV1000 almost each flowrate is measured 3 times, to increase the reliability. Unfortunately, there was not enough time left to do this for all cases. As can be observed the optical efficiency increases in all cases when increasing the flowrate, which was already expected for single pass mode, according to literature and steady state experiments of Degenhart, see 2.2. This is now also confirmed for multi-pass mode. For PV800 and PV1000 the optical efficiency increases with 3% when increasing the flowrate from 1 to 4 L/min. For PV200 this is 9%, which is surprisingly unexpected. This can also be observed in the thermal efficiency of the collector, see figure B.3. For more explanation of this phenomenon, see section 4.1.6.

In each sub-plot it can also be observed that the last measuring day has a slightly lower optical efficiency, namely approximately -2.2%, -2.9% and -1.3% for PV200, PV800 and PV1000 respectively. However, the irradiance  $G$ ,  $T_{m,c}$ ,  $T_{a,c}$ ,  $T_{a,setup}$  (see table B.1) are approximately identical for each measurement, which indicates that there might be some mechanical issues. All uncertainties regarding the flowrate, irradiance, fluid properties and temperature differences are pointing in the same direction for all measurements, so that is probably not causing the slightly lower optical efficiency. This slightly lower optical efficiency might probably due to some of the effects below:

- The position of the collector with respect to the solar simulator might slightly deviate
- Each time, when the collector has been displaced each condensor was inspected in order to check if the condensor was not slid down into the evacuated tube. It might be possible that the thermal contact between the manifold and the condensor is not exactly the same. More information about this phenomenon is presented in appendix K.1.
- The solar simulator is operating for more than 8000 hours after this research. The lifetime of the lamps are approximately 8000 hours, and during this research 2 of them broke down, see appendix K.2 for the position of those lamps. Initially, it was assumed that this had minimum to zero effect on the thermal efficiency of the collector, because these lamps are not placed in the region of the solar collector. It might also be possible that other lamps are almost at the end their lifetime and irradiate less then normally. If this is the case, some evacuated tubes receive less irradiance then the pyranometer measures, causing a slightly efficiency drop.

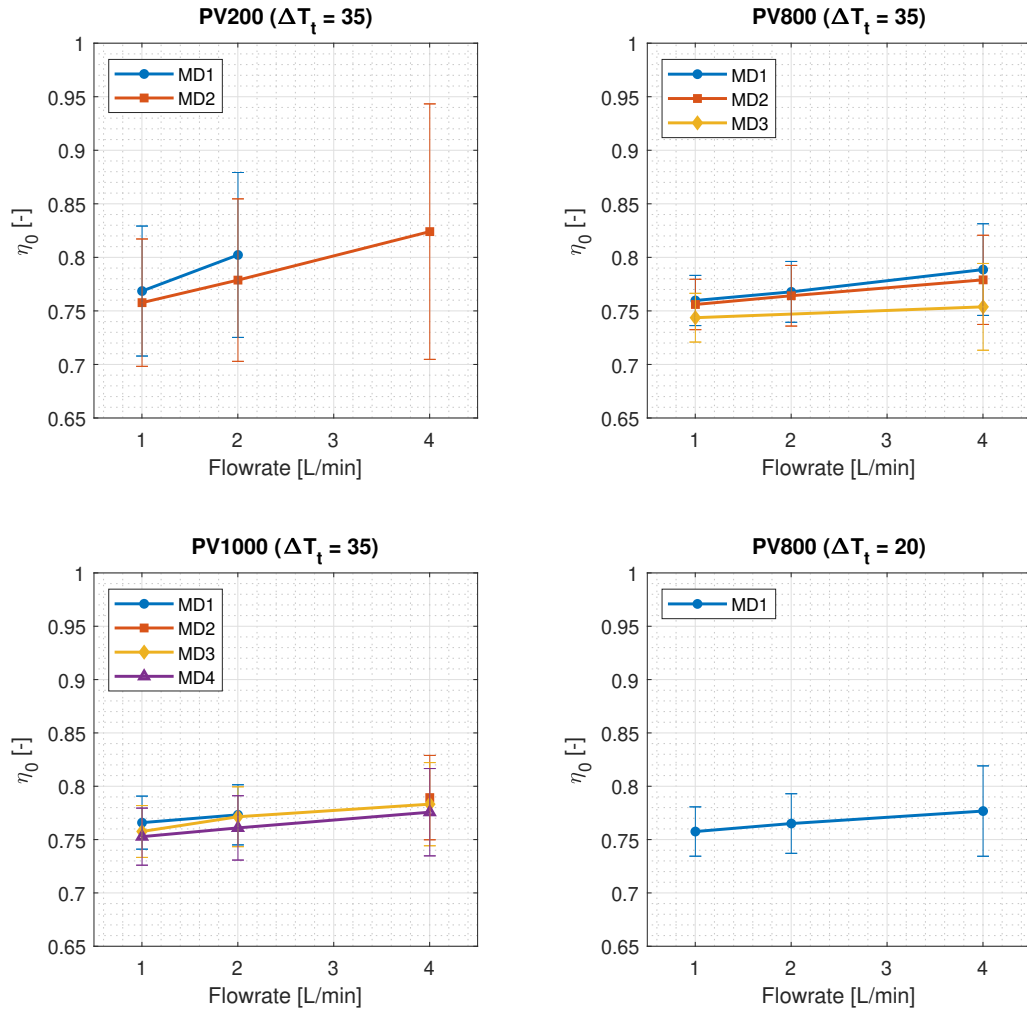


Figure 4.4: Optical efficiency vs. flowrate for multi-pass mode. For  $\Delta T_t = 35^\circ\text{C}$  a  $T_{low}$  of  $10^\circ\text{C}$  is used and for  $\Delta T_t = 20^\circ\text{C}$  a  $T_{low}$  of  $20^\circ\text{C}$  is used.

Table 4.4: An overview of the periods in which each measurement took place. (MD = Measurement Day)

M. Period	PV200 $\Delta T_t = 35^\circ\text{C}$	PV800 $\Delta T_t = 35^\circ\text{C}$	PV1000 $\Delta T_t = 35^\circ\text{C}$	PV800 $\Delta T_t = 20^\circ\text{C}$
mid-December	MD1	MD1, MD2	MD1, MD2, MD3	MD1
mid-January	MD2	MD3		
end-January			MD4	

**Total overview  $\Delta T_t = 35^\circ\text{C}$**

Figure 4.6 shows all multi-pass measurements for  $\Delta T_t = 35^\circ\text{C}$  in one graph to compare the influence of the irradiance. As can be observed the optical efficiency is slightly higher for PV1000 compared to PV800. The actual increase is 1.4 % on average. This value is calculated by taking the average of all measurements and interpolating 1 value of 2 L/min at PV800.

The most remarkable observation is that the optical efficiencies for PV200 are higher than for PV800 and for PV1000. It was expected that the optical efficiency decreases slightly when lowering the irradiance, as explained in section 4.1.1; however, these results show clearly the opposite. This is probably due to the much higher uncertainty, see section 4.1.6 for further explanation.

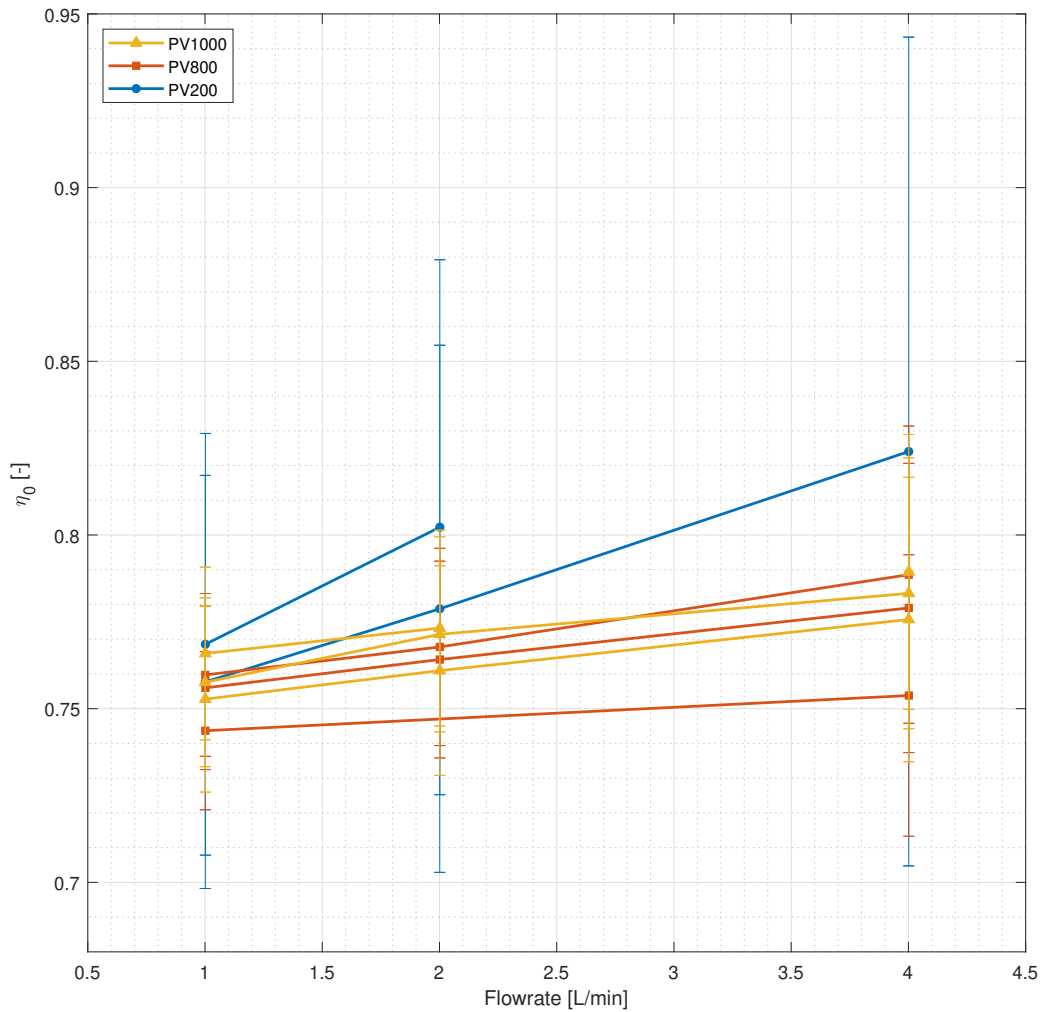


Figure 4.5: Optical efficiency vs. flowrate for multi-pass mode with  $\Delta T_t = 35^\circ\text{C}$  and  $T_{low}$  of  $10^\circ\text{C}$  (all measurements).

**Optical efficiency comparison  $\Delta T_t = 20^\circ\text{C}$  vs.  $\Delta T_t = 35^\circ\text{C}$  at PV800 and 2 L/min**

Figure 4.6 shows a comparison between the optical efficiency of  $\Delta T_t = 20^\circ\text{C}$  and  $\Delta T_t = 35^\circ\text{C}$ . As can be observed the optical efficiency is almost identical for each flowrate. According to these measurements it can be concluded that the optical efficiency does not change significantly when changing  $\Delta T_t$ . However, only 1 measurement series has been conducted for  $\Delta T_t = 20^\circ\text{C}$ , so to confirm this conclusion it is recommended to conduct 1 or 2 extra measurement series in the future.

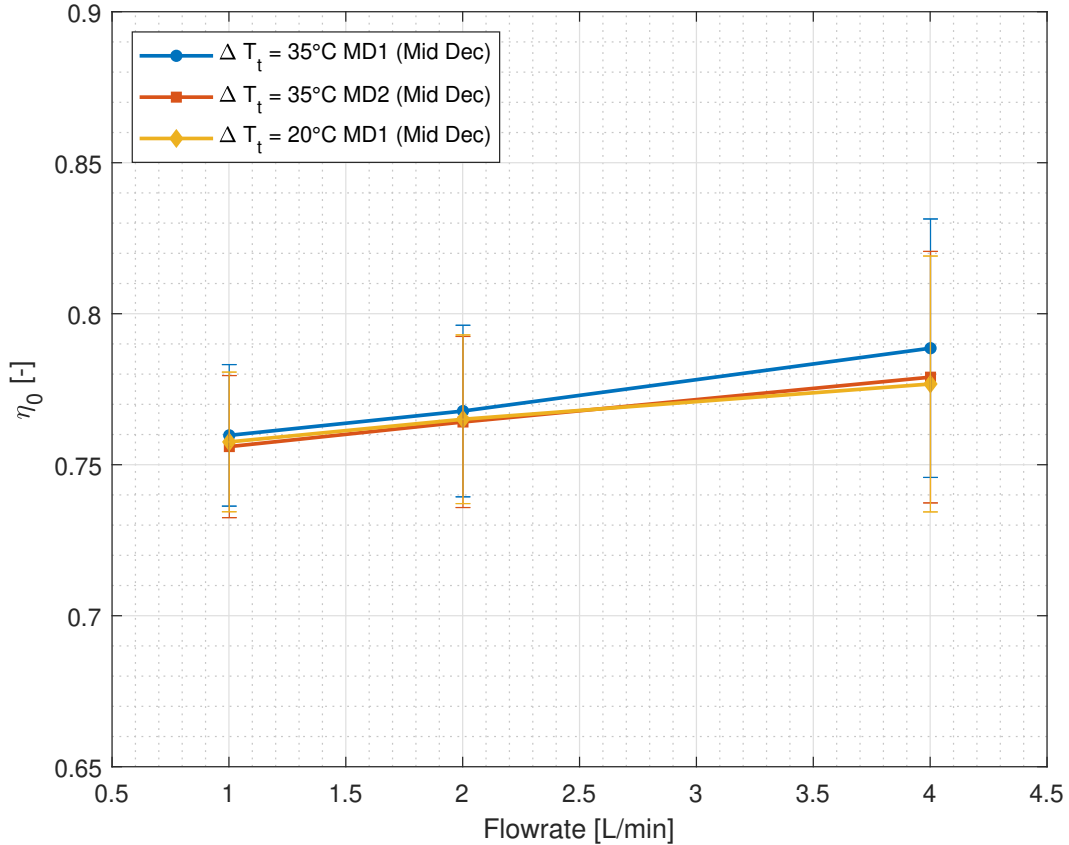


Figure 4.6: Optical efficiency vs. flowrate for multi-pass mode to compare  $\Delta T_t = 20^\circ\text{C}$  vs.  $\Delta T_t = 35^\circ\text{C}$  at PV800 and 2 L/min.  $T_{low} = 20^\circ\text{C}$  for  $\Delta T_t = 20^\circ\text{C}$  and  $T_{low} = 10^\circ\text{C}$  for  $\Delta T_t = 35^\circ\text{C}$ .

#### 4.1.6 Uncertainty Analysis Optical Efficiency

The calculation of the expanded combined uncertainties of all parameters are presented in appendix E. For all PV800 and PV1000 measurements the expanded combined uncertainty for 1, 2 and 4 L/min are approximately  $\pm 0.024$ ,  $\pm 0.028$  and  $\pm 0.041$  respectively. For PV200 this the expanded combined uncertainty is 0.06, 0.08 and 0.12 respectively, which is almost 3 times higher. This effect is mainly caused due to the uncertainty in  $\Delta T_c$ . Table 4.5 shows the average  $\Delta T_c$  for different irradiances and flowrates in column 2-4 and the last three columns show the expanded uncertainty expressed in percentage of the average value. The expanded combined uncertainty of  $\Delta T_c$  is  $0.14^\circ\text{C}$ , see also table 3.8. As can be observed the relative uncertainty for PV800 is slightly higher than PV1000, because  $\Delta T_c$  is also slightly higher. The highest uncertainty is lower than 5%. A higher effect can be observed when comparing PV800 or PV1000 with PV200. In this case the uncertainty can rise up to 14.4%, which is clearly not desired. This is, among other things, also the reason why the ISO norm suggests that, for indoor collector testing, the irradiance

must be higher than  $700 \text{ W/m}^2$ . The steep gradient of PV200 might be explained due to the high uncertainty, this uncertainty namely also increases sharply when increasing the flowrate. The same error in  $\Delta T_c$  might results in an overestimation of the thermal- and optical efficiency when  $\Delta T_c$  is significantly low.

The uncertainty of the flowrate and the irradiance have more effect at lower measured values, since the expanded combined uncertainty (expressed in percentage of the measured value) is relative higher. Uncertainties in  $c_p$  and  $\rho$  are negligible:  $0.28 \text{ J/(kgK)}$  and  $0.16 \text{ kg/m}^3$  respectively, see section 3.7.

Also the random errors that occur during the measurements are negligible, because the amount of samples is high enough and the process parameters are very stable. Examples of the random error for the flowrate, irradiance and ambient temperature are:  $0.001 \text{ L/min}$ ,  $0.7 \text{ W/m}^2$  and  $0.009^\circ\text{C}$  respectively. The number of samples for each measurement depends on the total cycle time, but the average number of samples for PV800 and PV1000 are 626 and for PV200 2253.

The horizontal error bars are excluded from figures 4.4 and 4.6, because these are too small to visualize. The expanded combined uncertainty for 1, 2 and 4 L/min are  $\pm 0.006$ ,  $\pm 0.012$  and  $\pm 0.02 \text{ L/min}$  in all cases.

Finally, the conversion from  $\eta_{th}$  to  $\eta_0$  adds an extra uncertainty which is in almost all cases less than  $\pm 0.001$  ( $T_{red}$  is approximately  $0.005 \text{ m}^2\text{K/W}$ ). However, for PV200 this can rise up to  $\pm 0.01$ , since  $T_{red}$  is approximately  $0.03 \text{ m}^2\text{K/W}$ , due to a higher  $T_m$  and lower  $T_a$ .

Table 4.5: Average  $\Delta T_c$  for each flowrate and irradiance. The last three columns represent the expanded uncertainty expressed in percentage of the average value. The unit L/min is abbreviated as L/m. to save space.

Irradiance	Average $\Delta T_c$			Expanded uncertainty (0,14°C)		
	@ 1 L/m.	@ 2 L/m.	@ 4 L/m.	@ 1 L/m.	@ 2 L/m.	@ 4 L/m.
	[°C]	[°C]	[°C]	[%]	[%]	[%]
PV200	3,8	2,0	1,0	3,8	7,2	14,4
PV800	11,7	6,0	3,0	1,2	2,4	4,8
PV1000	13,5	7,0	3,5	1,1	2,1	4,1

At one day the pyranometer gave a very low signal, for example  $50 \text{ W/m}^2$ . This is a problem that was also observed sometimes a few years ago, but this year this problem never occurred, except for 1 day. The signal came back after ticking on the pyranometer housing; therefore, a small defect in the cable or cable connection is likely the case. Currently, lab technicians are trying to solve this problem. This problem occurred on the 29th of January, which is MD4 for PV1000. Therefore, an average value of 1369 is used for these measurements. This average value is based on 37527 samples, with a minimum and maximum bound of  $22 \text{ W/m}^2$ . Since 100% of the samples are within these bounds, a minimum confidence interval of 95% can be assumed (expanded uncertainty); therefore, a divisor of 2 is used to calculate the expanded combined uncertainty. Also a maximum random error of  $0.4 \text{ W/m}^2$  is used for calculating the expanded combined uncertainty.

### 4.1.7 Results temperature distribution in evacuated tubes

Figure 4.7 shows the average temperature difference inside the first evacuated tube during multi-pass mode. It can be observed that the average temperature inside the evacuated tubes lowers slightly when increasing the flowrate, which was also expected, because the lower the average temperature inside the evacuated tube, the higher the efficiency of the collector.

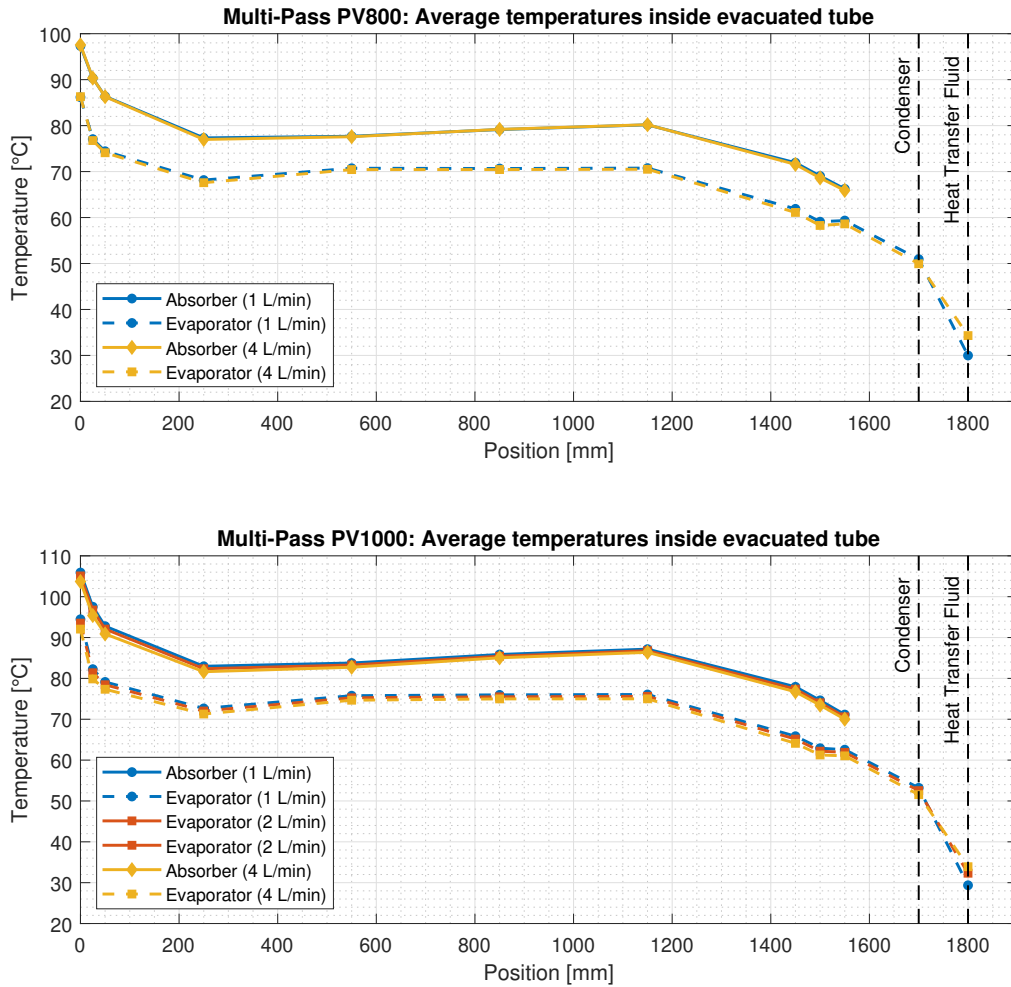


Figure 4.7: Average temperature difference inside one evacuated tube during multi-pass mode. Conditions: PV800, PV1000,  $\Delta T_t = 35^\circ\text{C}$  and  $T_{low} = 10^\circ\text{C}$ .



## 4.2 Single-pass

### 4.2.1 Method

In order to make a comparison between single- and multi-pass mode it is desired to compare the efficiency of both when having the same supply temperature of the tank. Only then, a fair comparison is possible, because comparing with the same flowrate would result in lower supply temperature for the tank, causing mixing of cold and hot water in the top of the tank.

The goal is to determine the thermal- and optical efficiency and to compare the temperatures in the evacuated tubes to the measurements of the multi-pass mode at the same irradiance,  $T_{low}$  and  $\Delta T_t$ , resulting in a certain flowrate.

An overview of the measurement plan is given in table 4.6. Unfortunately, there was not enough time left to conduct measurement 4. It also turned out that the flowrate becomes lower than 0.1 L/min for the setting PV200. Such a low flowrate is definitely not recommended, since thermal stratification start to form at flowrates lower than 0.2 L/min, according to CFD results of Degenhart [9]. Furthermore, the flowmeters are internally limited to 0.1 L/min, which generally can be adjusted by a service mechanic from KROHNE, but for this research it is decided not to measure below 0.1 L/min to prevent thermal stratification in the manifold. Therefore, both measurements 1 and 4 are marked with a grey colour and are not conducted.

Table 4.6: Measurement (M.) plan single-pass mode in order to determine the optical efficiency

<b>M.</b>	<b>Irradiance</b>	$T_{low}$	$\Delta T_t$
[nr.]	[W/m <sup>2</sup> K]	[°C]	[°C]
1	PV200 = ± 400	10	35
2	PV800 = ± 1200	10	35
3	PV1000 = ± 1400	10	35
4	PV800 = ± 1200	20	20

### 4.2.2 Measuring procedure

The biggest difference in the measuring procedure between single-pass and multi-pass is that water from the collector need to enter the tank via TC5 (the tank inlet at the top of the tank), instead of via TC4 and the TDV. It is recommended to cool down the entire tank to the desired  $T_{low}$ , preferably during the night, since this takes very long to achieve 10°C for the entire tank.

Then almost the same procedure as for multi-pass is used, but now the flow is adjusted manually in order to achieve the right supply temperature for the tank. However, this method is very time consuming for the first time, because it is required to wait 30-60 minutes before a steady state is reached. Therefore, a PID controller is developed in LabVIEW to automatically adjust the flowrate. However, the settings of this controller still need to be optimised. Because the time was limited to optimise the PID settings, the measurements in this research are conducted with the manual operation, but in the future it is possible to automate this measurement.

The automatic control valve (CV) is able to control very low flowrates with high precision; however, during the first tests it turned out that the flowrate becomes unstable when CV is operating at an open position lower than 8% (typical flowrate < 0.5 L/min). This is thoroughly investigated by turning off all automatic PID controller and operating CV manually. By trial and error, after many testing days, it could be concluded that the pump caused these oscillations. The solution to prevent this phenomenon is to also throttle the pump suction line, by setting the manual control valve between 0.6-0.8 in stead of fully open (5.0). Then the flowrate becomes very stable, also for flowrates lower than 0.5 L/min. It seems that the pressure of the supply- and suction line of the pump is more balanced in this case, preventing the pump to become unstable. A theoretical

substantiation has not yet be found, but this is very practical method to solve the problem of the oscillating flowrate.

When steady state is achieved, after waiting approximately 60 minutes, a total of 900 samples will be taken over a measuring range of 15 minutes.

The settings of the PID parameters can be found in table 4.7 for EMV1, EMV2 and CV. Again, all PID parameters are determined by trial and error. One important difference is that the gain ( $K_c$ ) is higher for single-pass. With a higher gain a new constant flowrate can be faster obtained, which is an advantage in this experiment. The single-pass mode is also more stable than the multi-pass mode, so higher gain values still result in a steady signal. For multi-pass experiments the system may become unstable when using such a high gain, because temperature variations and TDV influences causes small disturbances in the flowrate.

Furthermore, the settings for the pumps and the manual control valve are given in table 4.8.

Table 4.7: Settings of PID parameters for single-pass mode

PID Parameters	EMV1	EMV2	CV	Unit
$K_c$	0,025	0,025	0,1	[-]
$\tau_i$	0,02	0,02	0,02	[min]
$\tau_i$	0,02	0,02	0,02	[min]

Table 4.8: PWM signals for all three pumps for single-pass mode. The flowrate in this table corresponds to the flowrate of the solar circuit, thus the settings of PMP2 and PMP3 are independent of that flowrate.

Flowrate	PMP1 PWM	PMP2 PWM	PMP3 PWM
[L/min]	[-]	[-]	[-]
$\leq 1$	2	0	10
$> 1$	$\geq 5$	0	10

#### Temperature measurements inside one evacuated tube

All temperatures inside the the first evacuated tubes are measured in order to compare these results with multi-pass mode. It is highly important that the comparison is done with exactly the same fin orientation. This will be further explained in the next section.

The temperature measurements are also conducted to investigate whether or not thermal stratification occurs at lower flowrates inside the manifold. Degenhart [9] concluded that thermal stratification occurs at flowrates lower than 0.2 L/min; however, I expect that this already occurs at slightly higher flowrates. To investigate this phenomenon, each single-pass measurement is conducted twice. The first experiment is conducted in normal operation, which means that the temperature measurements take place in the first tube after the inlet of the collector. In the second experiment the in- and outlet of the collector are reversed, which is possible due to the flexible tubes. During this experiment the temperature measurements take place in the 10th tube (last tube). By comparing both condensor temperatures it can be concluded whether or not thermal stratification occurs.

### 4.2.3 Additional experiment temperature distribution in evacuated tubes

The measured temperature distribution inside the evacuated tubes highly depends on the axial position and the rotation of the aluminum fin. A small change in position might result in different temperatures. During this research 3 thermocouples went loose of the aluminum fin; therefore, the fin has been dismantled and the thermocouples are attached with new aluminum tape. In order to check how significant this effect is, one measurement is conducted with PV800 and 2 L/min (Single-pass) to compare the results with Degenhart, see figure 4.9 for the results.

### 4.2.4 Results Optical efficiency

Figure 4.8 shows the optical efficiencies for single-pass mode with  $\Delta T_t = 35^\circ\text{C}$  and  $T_{low} = 10^\circ\text{C}$ . Measurement day 1 took place on the 15th of January and measurement day 2 took place on the 27th of January. In order to obtain an inlet temperature of the tank of  $45^\circ\text{C}$ , a flowrate of 0.34 L/min is required for PV800 and 0.39 L/min for PV1000. It can also be observed that the average optical efficiency is 0.74 and 0.73 for PV800 and PV1000 respectively, which is approximately the same if the uncertainty is taken into account. In the next section this will be further explained in the uncertainty analysis.

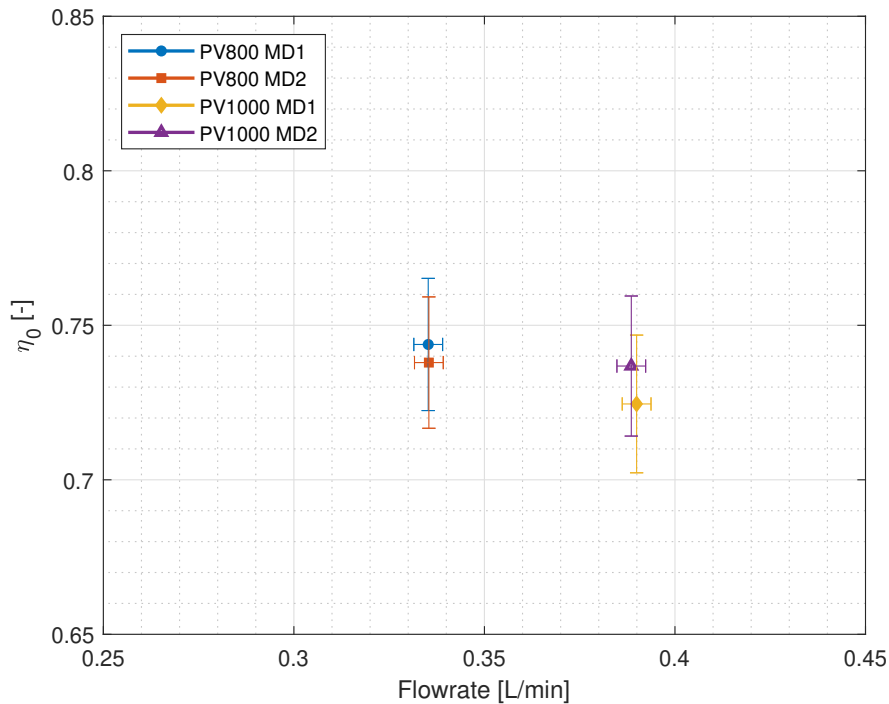


Figure 4.8: Optical efficiency vs. flowrate for single-pass mode. Conditions:  $\Delta T_t = 35^\circ\text{C}$  and  $T_{low} = 10^\circ\text{C}$ .

### 4.2.5 Uncertainty analysis

Also for single-pass measurements, the calculation of the expanded combined uncertainties of all parameters are presented in appendix E. It can be observed that for single-pass mode the expanded uncertainty of the optical efficiency has the same order of magnitude as for multi-pass mode at 1 L/min. At lower flowrates, the uncertainty of the irradiance, flowrate and temperature difference have an almost equal contribution to the total combined uncertainty. The expanded uncertainty of  $\Delta T_c$ , flowrate and irradiance relative to its measured value are approximately 0.4% 1.1% and 1.2% respectively. So, the uncertainty of the flowrate and the irradiance has two times more contribution to the total expanded combined uncertainty than the uncertainty of  $\Delta T_c$  for single-pass mode.

Also here the random errors that occur during the measurements are negligible, because the amount of samples is high enough and the process parameters are very stable.

In this case the horizontal error bars are included, since the relative uncertainty of the flowrate becomes higher for lower flowrates, see chapter E. The order of magnitude of this error is  $\pm 0.004$  L/min.

Finally, the extra uncertainty regarding the conversion from  $\eta_{th}$  to  $\eta_0$  is negligible, since  $T_{red}$  is approximately zero, namely  $-0.001 \text{ m}^2\text{K/W}$ .

### 4.2.6 Results temperature distribution in evacuated tubes

#### Reference measurement

As mentioned in section 4.2.2 the measured temperature distribution inside the evacuated tubes highly depends on the axial position and the rotation of the aluminum fin. Therefore, one reference measurement is conducted with PV800 and 2 L/min to compare the results with the results of Degenhart [9]. Figure 4.9 shows the results of the temperature distribution of the current position of the fin and the results of Degenhart. The blue solid lines represent the actual measurements and the orange solid lines represent the measurements of Degenhart. The solid lines represent the measurements close to the absorber and the dashed lines represent the measurements close to the evaporator (heatpipe). Also the temperature differences between the absorber and the evaporator are shown. This temperature difference is a measure for the transferred heat through one fin 'arm'. As can be seen in 2.2, the fin consist of two arms. The heat of the absorber is transferred via those arms to the evaporator.

As can be observed, the water- (heat transfer fluid) and the condenser temperature are approximately the same, which was also expected, since all conditions are equal. This means also that the transferred heat of the evacuated tube to water is approximately the same. However, there is a relative large difference in the temperature distribution of the absorber and evaporator. From position 850mm to 1800mm the temperature matches quite well, but at lower positions the temperature deviate considerably.

It can also be observed that the temperature difference deviates approximately  $5^\circ\text{C}$ . Out of these observations it can be concluded that, in the actual measurements, the evacuated tube supplies approximately the same amount of heat to the water in the manifold and that a larger part of the transferred heat is transported via the other arm of the fin instead of via the arm where the thermocouples are mounted. This is probably due to the fact that the fin is positioned in a slightly different way than before.

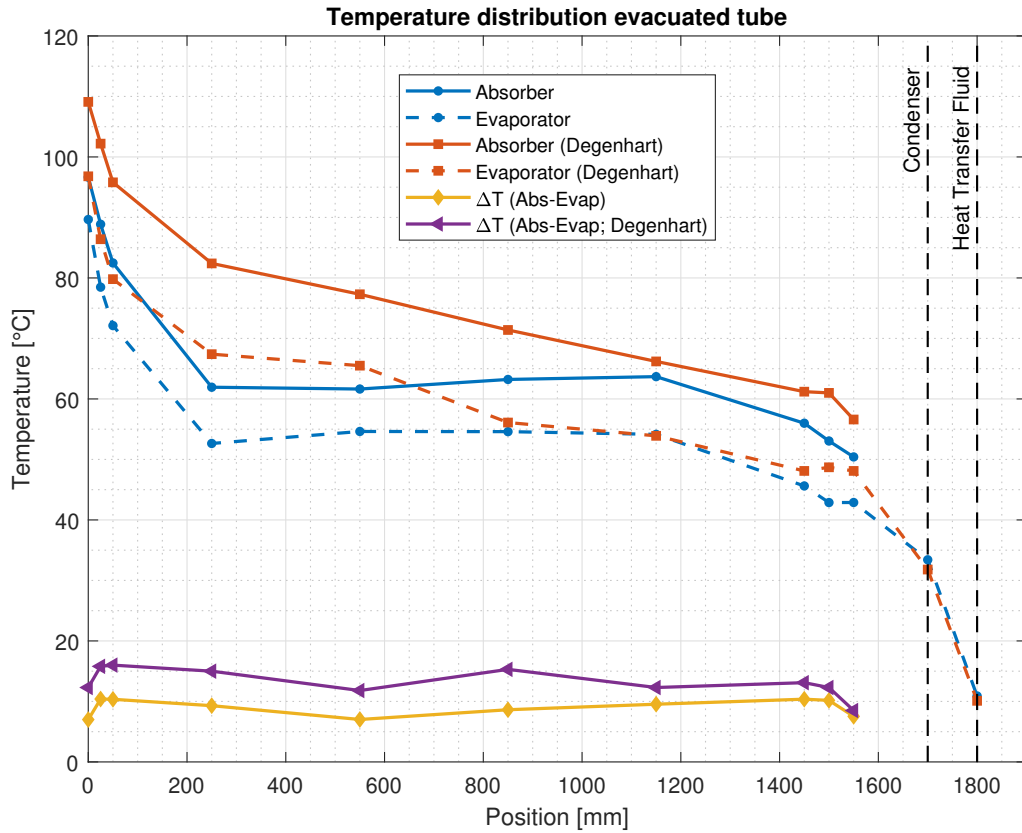


Figure 4.9: Reference measurement: Temperature distribution inside one evacuated tube. Current Position Fin vs. Position Degenhart at PV800 and 2 L/min.

#### Single-Pass with $\Delta T_t = 35^\circ\text{C}$

Figure 4.10 shows the temperature distribution inside the evacuated tube for PV800 and PV1000 during single-pas mode. Position 0mm corresponds to the bottom of the heatpipe (evaporator) and position 1700mm corresponds to the condenser. The temperature of the heat transfer fluid is the inlet temperature of the collector. In each sub figure the upper two lines (coloured in orange) correspond to a temperature measurement in the last tube (tube 10) and the two lower lines correspond to a temperature measurement in the first tube (tube 1). In all cases the temperature rises between the condenser and position 1150mm, then the temperatures remains approximately the same until position 250mm en then the temperature rises again. As can be observed for PV800 and PV1000 the temperature difference between tube 1 and tube 10 is mainly determined by the difference in condenser temperature, which is  $20.8^\circ\text{C}$  and  $21.3^\circ\text{C}$  respectively. These temperature differences are relative low, because the temperature difference over the collector ( $\Delta T_c$ ) is  $34.9^\circ\text{C}$  for PV800 and  $34.8^\circ\text{C}$  for PV1000. This might possibly be due to some thermal stratification inside the manifold. It is expected that no thermal stratification occurs when the difference of condenser temperature between tube 1 and tube 10 is almost equal to  $\Delta T_c$ . Furthermore, it can be observed that the temperatures inside the evacuated tubes are higher for PV1000 than for PV800, which due to the higher irradiation. Also the average temperature difference between the condenser and evaporator are approximately constant over the heatpipe length, this also a measure for the total heat that is transported in radial direction. The heat flux in radial direction (from absorber to evaporator/heatpipe) is defined as  $\dot{Q} = \Delta T/R$ , where R is the same across the fin.

The increase in temperature at the bottom of the heatpipe is probably due to the fact that the

heatpipe is shorter than the aluminum fin and the absorber tube. This means that the heatpipe collects more heat at the bottom of the tube. However, the temperature difference between the absorber and the evaporator is not higher in this region, probably because this heat is also transported in axial direction via the aluminum fin and not only in radial direction (the sensors can only detect a temperature difference in radial direction). Degenhart [9] concluded that no dry-out takes place during single-pass measurements at tilt angles of  $45^\circ\text{C}$ , so the temperature increase at the bottom of the heat pipe is not due to dry-out.

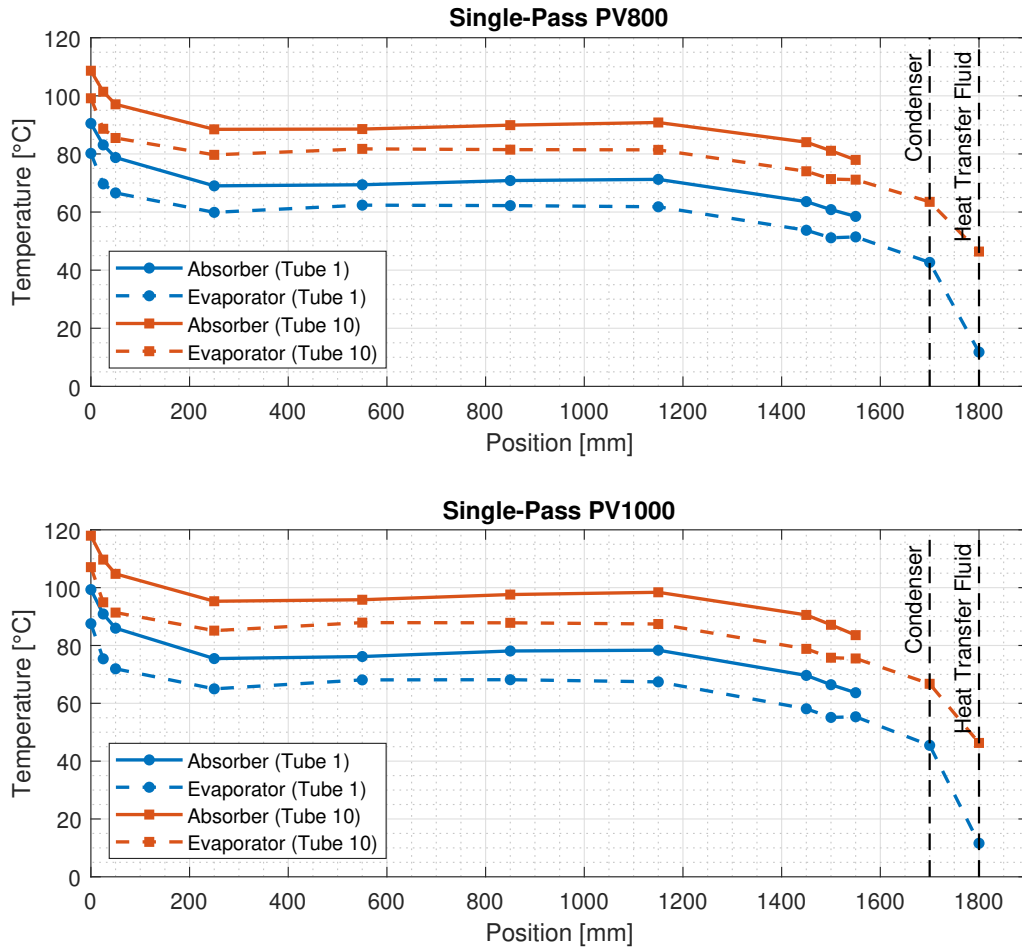


Figure 4.10: Temperature distribution inside one evacuated tube during single-pass mode with conditions: PV800 (0.34 L/min), PV1000 (0.39 L/min),  $\Delta T_t = 35^\circ\text{C}$ ,  $T_{low} = 10^\circ\text{C}$ .

## 4.3 Single-Pass vs Multi-Pass

### 4.3.1 Thermal efficiency of the total system

Figure 4.11 shows an overview of the comparison of the thermal efficiency of the total system between single- and multi-pass mode. In the legend MP stands for 'Multi-Pass', SP stands for 'Single-Pass' and MD stands for 'Measurement Day'.

For single-pass measurements the total thermal efficiency of the system is approximately 0,73 on average, for both PV settings PV800 and PV1000. The heatloss of the piping is 9 Watt on average. And other conditions for PV800 and PV1000 are:  $T_{m,col} = 29,1^{\circ}\text{C}$  for both PV settings,  $T_{a,col} = 29,5^{\circ}\text{C}$  and  $29,8^{\circ}\text{C}$  respectively and  $T_{a,setup}$  is equal to  $25.1^{\circ}\text{C}$  in all cases.

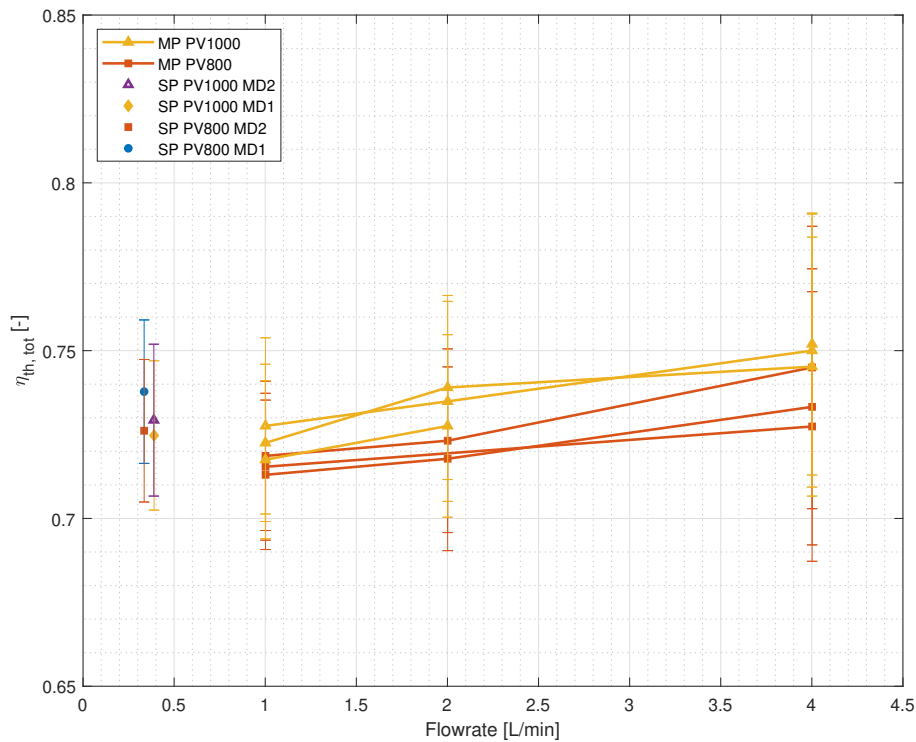


Figure 4.11: Comparison between single- and multi-pass mode: Thermal efficiency total system vs. flowrate. For  $\Delta T_t = 35^{\circ}\text{C}$  a  $T_{low}$  of  $10^{\circ}\text{C}$  is used.

All specific process values of the multi-pass mode are presented in table B.1 and B.2. One important thing to emphasise is that the mean temperature of the collector  $T_{m,col}$  during multi-pass mode is in all cases higher than  $35.5^{\circ}\text{C}$ , which is  $6^{\circ}\text{C}$  higher than single-pass. The ambient temperature of the collector  $T_{a,col}$  during multi-pass is approximately  $28.9^{\circ}\text{C}$ , which is almost the same as during single-pass mode.  $T_{a,setup}$  was  $24^{\circ}\text{C}$  on average, which is  $1.1^{\circ}\text{C}$  lower than single-pass. Finally, the average heat losses of the piping were 31 Which is approximately 3 times higher than single-pass.

#### Conclusion

It can be concluded that the multi-pass mode operates at higher average temperatures. Due to the higher  $T_{m,col}$  and thus also an higher average fluid temperature in the entire loop of the system, the multi-pass mode has more heat losses in the piping. Although the multi-pass mode has more

heat losses in the piping the total efficiency is still higher than single-pass mode at flowrates higher than approximately 1.5 L/min for PV1000 and 3 L/min for PV800.

### 4.3.2 Optical Efficiency

On collector level it is more convenient to compare the optical efficiencies, since the mean temperature of the collector is approximately 6°C higher during multi-pass operation.

When comparing the optical efficiency with the multi-pass mode it might be more realistic to compare the values with the measurements in the same period, since it turned out that the optical efficiency was slightly lower in this period. However, it might also be interesting to compare the single-pass results with the multi-pass results in December. In figure 4.12 both comparisons are presented. The top figure is a comparison with measurements in January (worst case scenario) and the bottom one is a comparison with measurements in December (best case scenario).

It can be concluded that the multi-pass mode is 0,4 to 1,7% more efficient for PV800 and 1,6 to 4,7% for PV1000 in worst case scenario. For best the best case scenario these percentages are slightly higher, namely: 2,3 to 5,8% more efficient for PV800 and 2,8 to 6,1% for PV1000

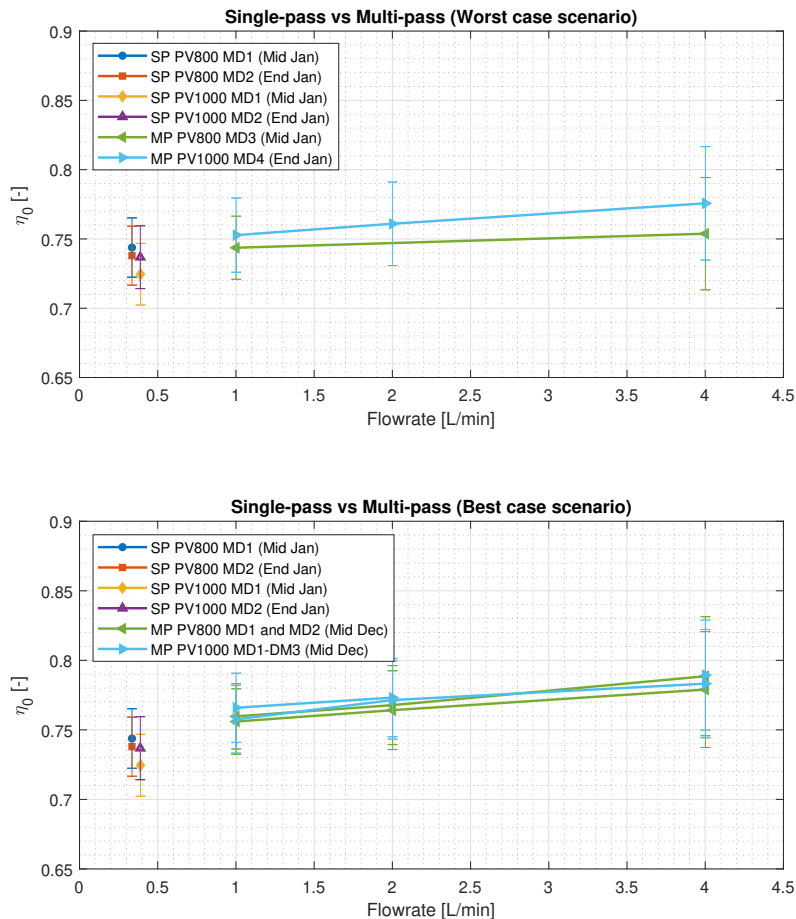


Figure 4.12: Single-pass vs Multi-pass at PV800, PV1000,  $\Delta T_t = 35^\circ\text{C}$  and  $T_{low} = 10^\circ\text{C}$ .



### 4.3.3 Temperature distribution in evacuated tubes

Figure 4.13 shows a comparison of the temperature distribution inside the evacuated tube between single-pass (SP) and multi-pass (MP) mode.

As can be observed the temperatures of the multi-pass mode lies between the single-pass measurements in tube 1 and tube 10. These lines are proportional to the temperatures heat transfer fluid and the condenser.

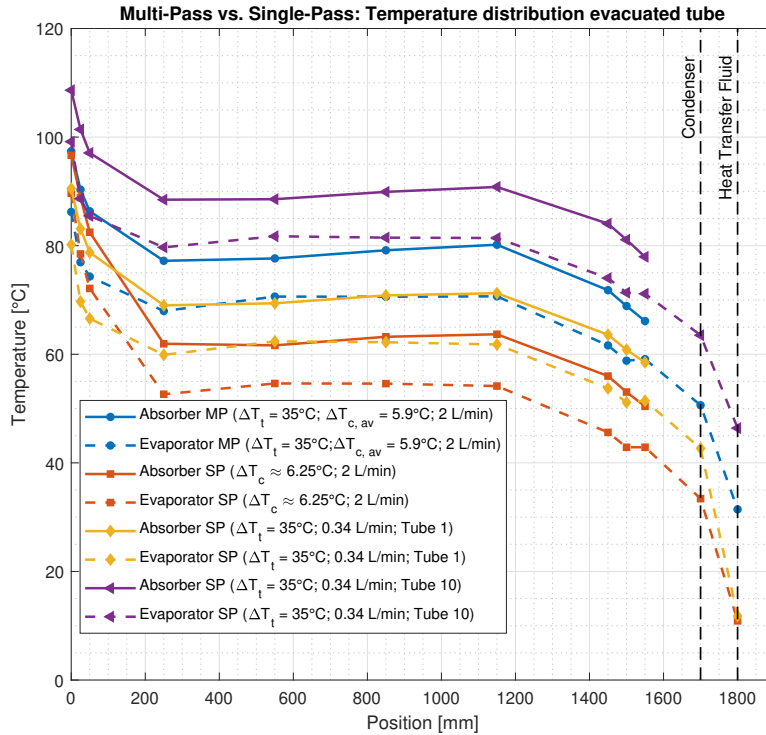


Figure 4.13: Temperature distribution in evacuated tube: Single-Pass (SP) vs Multi-pass (MP) at PV800,  $\Delta T_t = 35^\circ\text{C}$  and  $T_{low} = 10^\circ\text{C}$ .

#### Analysis Dry-ing out heatpipes

As mentioned before, Degenhart [9] concluded that no dry-out takes place for single-pass mode at a tilt angle of  $45^\circ$ . The increase in temperature at the bottom of the heat pipe is more likely caused by the fact that the fin is longer than the heat-pipe, resulting in more added heat due to axial heat transport through the fin. Since the average temperatures of the multi-pass mode show similar behaviour (only a step increase for the lower three thermocouples), it can be concluded that no dry-out occurs during multi-pass mode for PV800. The same holds for PV1000, because this shows similar behaviour, see figure 4.7.

# Chapter 5

## Thermo-Differential Valve

### 5.1 Thermo Differential Valve

In section 3.3.2 the working principle of the TDV is already explained. This chapter includes a theoretical approach of the switching moment and the switching time of the TDV. Furthermore, some experimental results are presented at the end of this section in order to compare these with the theoretical approach.

#### 5.1.1 Switching moment

Now the general working principle is clear, the thermodynamics inside the actuator can be explained. The switching moment is defined as the moment when the liquid in the actuator starts to flow into the float (in closed position) or into the container (in open position); it is highly important to emphasise that this is not the moment when the float starts to move.

The driving force behind this principle is the difference in vapour pressure inside the container and the float. The moment when the liquid starts to flow, depends on the required minimum temperature difference between the inlet of the TDV and the tank temperature. When this minimum temperature difference is reached, the actuator is in thermodynamic equilibrium and the liquid will be forced from container to float or from float to container. This thermodynamic equilibrium is explained in formula form below, for opening- and closing the TDV respectively.

#### Opening TDV

In figure 5.1 a cross-sectional view of the TDV in closed position is presented. As explained before, in this position all liquid is stored in the container. In this figure it can be observed that the liquid in the container needs to overcome a height ( $\Delta h$ ) in order to flow into the float. In other words: The vapor pressure inside the container ( $P_{v,1}$ ) needs to be equal to the vapour pressure in the float ( $P_{v,2}$ ) plus the hydrostatic pressure defined by  $\Delta h$ , see equation (5.1).

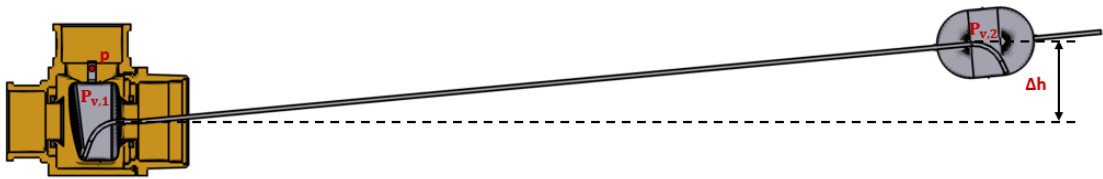


Figure 5.1: This figure shows the locations of the vapour pressure inside the container and the float. It also shows the height that the liquid needs to overcome in order to flow into the float.

$$P_{v,1}(T_1) = P_{v,2}(T_2) + \rho_2 g \Delta h \quad (5.1)$$

With  $\rho_2$  the density at the temperature of the tank  $T_2$ . In this calculation  $T_2$  is assumed to be constant. When equilibrium of equation (5.1) is reached, the entire tube is filled with liquid, but there is no flow to the float.

Equation (5.1) can be solved numerically in order to obtain the required minimum inlet temperature of the TDV ( $T_{1,min}$ ). Then the minimum required temperature difference can be obtained by equation (5.2):

$$\Delta T_{TDV,min} = T_{1,min} - T_2 \quad (5.2)$$

With  $\Delta T_{TDV,min}$  is the minimum temperature difference between the minimum required inlet temperature of the TDV ( $T_{1,min}$ ) and the tank temperature ( $T_2$ ).

### Closing TDV

Almost the same procedure holds for closing the TDV, but now all liquid is stored in the float and needs to overcome a height  $\Delta h$  to flow to the container. The  $\Delta h$  is the same as for opening the TDV. In this case the required minimum inlet temperature of the TDV ( $T_{1,min}$ ) can be obtained by solving equation (5.3) numerically.

$$P_{v,2}(T_2) = P_{v,1}(T_1) + \rho_2 g \Delta h \quad (5.3)$$

Then the minimum required temperature difference can be obtained by equation (5.4):

$$\Delta T_{TDV,min} = T_2 - T_{1,min} \quad (5.4)$$

Since  $\Delta T_{TDV,min}$  depends on the tank temperature it is useful to show this relationship. As a result,  $\Delta T_{TDV,min}$  is calculated as function of tank temperature and presented in figure 5.2. It can be observed that  $\Delta T_{TDV,min}$  is slightly higher, which is due to the difference in fluid properties around the tank temperature.

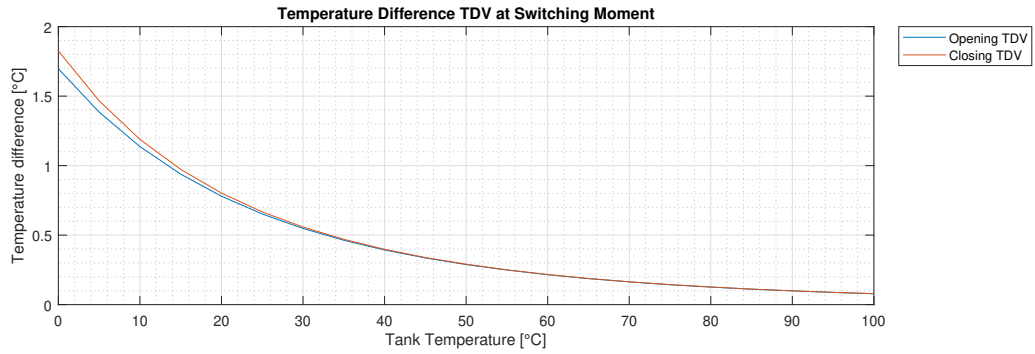


Figure 5.2: Required temperature difference ( $\Delta T_{TDV,min}$ ) to obtain thermodynamic equilibrium (switching moment) inside the actuator as function of tank temperature. For opening the TDV holds:  $\Delta T_{TDV,min} = T_{1,min} - T_2$ ; for closing the TDV holds:  $\Delta T_{TDV,min} = T_2 - T_{1,min}$

### 5.1.2 Switching time

When  $\Delta T_{TDV,min}$  is reached, the entire tube is filled with liquid and the actuator is in perfect thermodynamic equilibrium. Then, if the inlet temperature of the TDV increases slightly more, the liquid enters the float in closed position or it enters the container in open position. At some moment in time, there is enough liquid transferred such that the TDV opens or closes. So, first the amount of liquid that needs to be transferred, should be calculated in order to determine the switching time. It is assumed that the time that it takes to open or close the valve can be neglected. Thus, the switching time can be defined as the time it takes to fill the float (or container) until the right amount of liquid is reached, counted from the switching moment on.

To determine the switching time, more insight into the moment balance around the pivot point of the TDV is needed. Figure 5.3 gives an overview of all forces that apply on the actuator in closed position. In open position all forces, except the release force ( $F_{release}$ ), have the same direction. As can be seen, the direction of  $F_{release}$  is counterclockwise in closed position, but in open position the direction of  $F_{release}$  is clockwise. Figure 5.3 also shows a pivot point ( $p$ ), the centre point of the housing of the TDV ( $c$ ), the centre point of the tube ( $t$ ) and the centre point of the float ( $f$ ). Also the corresponding moment arm lengths are given in this figure.

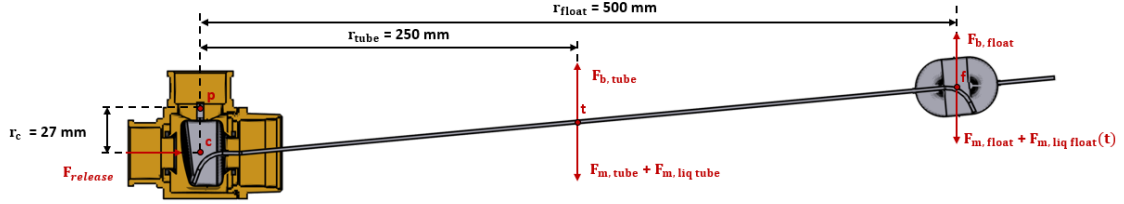


Figure 5.3: An overview all forces that apply on the container, the tube and the float of the TDV in closed position. In addition, the corresponding moment arms are presented.

Where  $F_{release}$  is release force of the TDV. This force can be derived from the pressure drop over the TDV. Actually, this pressure drop consists of a few terms, for example the in- and outflow effects, the blockage effect of the top of the container and the resistance of the sidewall of the container. It is assumed that all effects are negligible compared to the resistance of the sidewall of the container; therefore, the entire pressure drop is entirely translated into one force ( $F_{release}$ ), see equation (5.5). This force applies on the sidewall of the container.

$$F_{fr, valve} = \Delta P_{fr, valve} \cdot A_{c, ring} \quad (5.5)$$

Where  $A_{c, ring}$  is the cross-sectional flow area of the v-ring ( $A_{c, ring} = \pi/4 \cdot D_{ring}^2$ ). On both outlets of the TDV a v-ring of the type va-20 is used, which has a diameter ( $D_{ring}$ ) of 26 mm.

The pressure drop in equation 5.5 is calculated by equation (5.6).

$$\Delta P_{fr, valve} = \left( \frac{Q_v}{K_{vs}} \right)^2 \cdot 100000 \quad (5.6)$$

Where  $Q_v$  is the flowrate in  $m^3/h$  and  $K_{vs}$  is the flow coefficient, which is equal to  $8.0 m^3/h$ . In open position the  $K_{vs}$  value might be slightly lower, because the tube of the actuator might block some of the flow. However, this value is not entirely verified by Conico Valves bv. and therefore the same  $K_{vs}$  value of  $8.0 m^3/h$  is used for open position.

In general a buoyancy force can be defined as the weight of the displaced fluid times the gravitational constant ( $g$ ), which acts in the opposite direction of gravity. Both tube and float are submerged in water; therefore, they experience a buoyancy force. These buoyancy forces can be calculated using equation (5.7) and (5.8) respectively.

$$F_{b, float} = \rho_w \cdot V_{float} \cdot g \quad (5.7)$$

$$F_{b, tube} = \rho_w \cdot V_{tube} \cdot g \quad (5.8)$$

With  $\rho_w$  represents the density of the water in the tank,  $V_{float}$  the volume of the float and  $V_{tube}$  the volume of the tube.

All gravitational forces are obtained by multiplying the mass of the object times  $g$ , see equation (5.9), (5.10) and (5.11). In this calculation it is assumed that both gravitational- and buoyancy forces apply on the centre of the object. Furthermore, the mass of vapour in the float is assumed to be negligible.

$$F_{m, tube} = m_{tube} \cdot g \quad (5.9)$$

$$F_{m, liq tube} = m_{liq, tube} \cdot g \quad (5.10)$$

$$F_{m, float} = m_{float} \cdot g \quad (5.11)$$

After calculating all constant forces, the required amount of transferred liquid can be calculated. This can be realized by taking the moment balance around pivot point  $p$ , followed by calculating the required gravitational force on the float. This force can be calculated if the sum of the moments around pivot point  $p$  is zero. Because the moment balance for opening and closing the TDV slightly differs, both will be presented below.

#### Moment balance when TDV opens

When opening the TDV, the moment balance can be directly extracted from figure 5.3, resulting in equation (5.12). In this equation is the clockwise direction the positive direction.

$$\begin{aligned} \sum M_p = & (F_{m, tube} + F_{m, liq tube} - F_{b, tube}) \cdot r_{tube} \\ & + (F_{m, float} + F_{m, liq float}(t) - F_{b, float}) \cdot r_{float} - F_{fr, valve} \cdot r_c = 0 \end{aligned} \quad (5.12)$$

Next, the required gravitational force due to the liquid inside the float ( $F_{m, liq float}(t)$ ) can be calculated, see equation (5.13).

$$\begin{aligned} F_{m, liq float}(t) = & (F_{b, tube} - F_{m, tube} - F_{m, liq tube}) \cdot \frac{r_{tube}}{r_{float}} + F_{b, float} - F_{m, float} \\ & + F_{fr, valve} \cdot \frac{r_c}{r_{float}} = 0 \end{aligned} \quad (5.13)$$

Finally, the required mass that needs to be transferred ( $m_{liq, trans}(t_{end})$ ) can be determined by:

$$m_{liq, trans}(t_{end}) = \frac{F_{m, liq float}(t_{end})}{g} \quad (5.14)$$

#### Moment balance when TDV closes

When closing the TDV, the moment balance can not be directly extracted from figure 5.3, because in this case the friction force ( $F_{release}$ ) applies in clockwise direction instead of counterclockwise direction. Therefore, a new moment balance need to be used. By rearranging the new moment balance, equation (5.15) can be obtained.

$$\begin{aligned} F_{m, liq float}(t) = & (F_{b, tube} - F_{m, tube} - F_{m, liq tube}) \cdot \frac{r_{tube}}{r_{float}} + F_{b, float} - F_{m, float} \\ & - F_{fr, valve} \cdot \frac{r_c}{r_{float}} = 0 \end{aligned} \quad (5.15)$$

Subsequently,  $m_{liq,trans}(t_{end})$  can be calculated by equation (5.16). Note that, the fluid flows from the float to the container in this case.

$$m_{liq,trans}(t_{end}) = m_{liq,tot} - \frac{F_{m,liq float}(t_{end})}{g} \quad (5.16)$$

Where  $m_{liq,tot}$  is the total mass of liquid inside the actuator.

In figure 5.4 the required mass-fractions that need to be transferred to open or close the TDV at different flowrates are presented. In this figure the calculated  $m_{liq,trans}(t_{end})$  is normalized with  $m_{liq,tot}$ . As can be seen, more mass need to be transferred in order to close the TDV. Furthermore, it can be observed that slightly more mass needs to be transferred for higher flowrates.

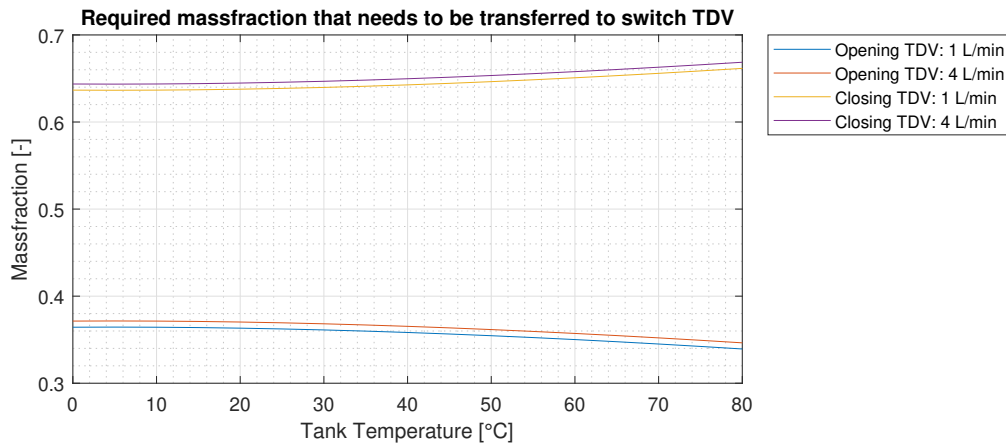


Figure 5.4: The required mass-fractions that need to be transferred to open or close the TDV at flowrates of 1 L/min and 4 L/min

### Switching Time when TDV Opens

Since the required amount of mass that needs to be transferred is determined, the time that it takes to transfer this amount of liquid can be calculated. Therefore, the velocity in the tube of the actuator needs to be determined first. If liquid is flowing through the tube an extra pressure drop term needs to be added to equation (5.1), resulting in equation (5.17).

$$P_{v1}(T_1) = P_{v2}(T_2) + \rho_2 g \Delta h + \Delta P_{friction}(v_{tube}) \quad (5.17)$$

If the inlet temperature of the TDV remains constant, also the pressure drop inside the tube as well as the velocity remains constant. The pressure drop inside the tube is defined as followed:

$$\Delta P_{friction}(v_{tube}) = f \frac{L_{tube}}{D_{i,tube}} \frac{\rho_m v_{tube}^2}{2} \quad (5.18)$$

The corresponding friction factor is obtained from VDI Heat Atlas [7]. In this handbook the Hagen-Poiseuille law is used for the friction factor for laminar flow and is described by equation (5.19). This equation applies very accurately to smooth tubes with a maximum absolute roughness of  $0.07 \cdot 10^{-3}$ . According to the producer (Sandvik) the absolute roughness is lower than  $0.4 \cdot 10^{-6}$ ; therefore, equation (5.19) is valid and can be used for  $Re < 2320$ .

$$f_l = \frac{64}{Re} \quad (5.19)$$

According to Blasius [7], the friction factor between  $3000 < Re < 100.000$  can be determined by equation (5.20). This equation holds for tubes with a maximum absolute roughness of  $0.001-0.002 \cdot 10^{-3}$ .

$$f_t = \frac{0.3164}{Re^{0.25}} \quad (5.20)$$

In the region between  $Re = 2320$  and  $Re = 3000$  an interpolation between  $f_l$  and  $f_t$  is used:

$$f_{trans} = f_{2320} + \frac{f_{3000} - f_{2320}}{3000 - 2320} \cdot (Re - 2320) \quad (5.21)$$

By rewriting equation (5.18), the velocity inside the tube can be obtained:

$$v_{tube} = \sqrt{\frac{2D_{i,tube}\Delta P_{friction}(v_{tube})}{fL_{tube}\rho_m}} \quad (5.22)$$

Finally, the corresponding flowrate ( $\dot{V}$  in  $m^3/h$ ) and the switching time can be calculated with equation (5.23) and (5.24) respectively. This is an iterative process since a velocity needs to be guessed in the first iteration. In the calculation of equation 5.23 it is assumed that the pressure drop in the tube is the determining factor of the flowrate in the tube and not the speed of the formation of vapour ( $m^3/s$ ) in the container or float.

$$\dot{V} = A_c v_{tube} \quad (5.23)$$

$$t_s = \frac{V_l}{\dot{V}} \quad (5.24)$$

Where  $A_c$  is the cross sectional flow area of the tube and  $V_l$  is the volume of liquid that needs to be transferred. This volume is retrieved by dividing  $m_{liq,trans}(t_{end})$  by the density of the liquid.

Figure 5.5 gives an overview of the switching times for opening and closing the TDV. As mentioned before, the the switching time also depends on the flowrate and the inlet temperature of the TDV. Therefore, the switching times are calculated for different inlet temperatures and presented in each subplot. The switching times are also given for a low flowrate (1 L/min) and a high flowrate (4 L/min), see the top and bottom figures respectively.

### Conclusion

It can be concluded that the switching time is higher for closing the TDV, which is caused by the fact that more liquid needs to be transferred. It can also be observed that the switching time decreases for higher inlet temperatures, which is caused by a higher driven force between the container and the float. The difference in switching time between a low and high flowrate is not significant according figure 5.5. Furthermore, it is important to notice that the shape of the curves is due to the friction factor of the tube of the actuator, see figure 5.6.

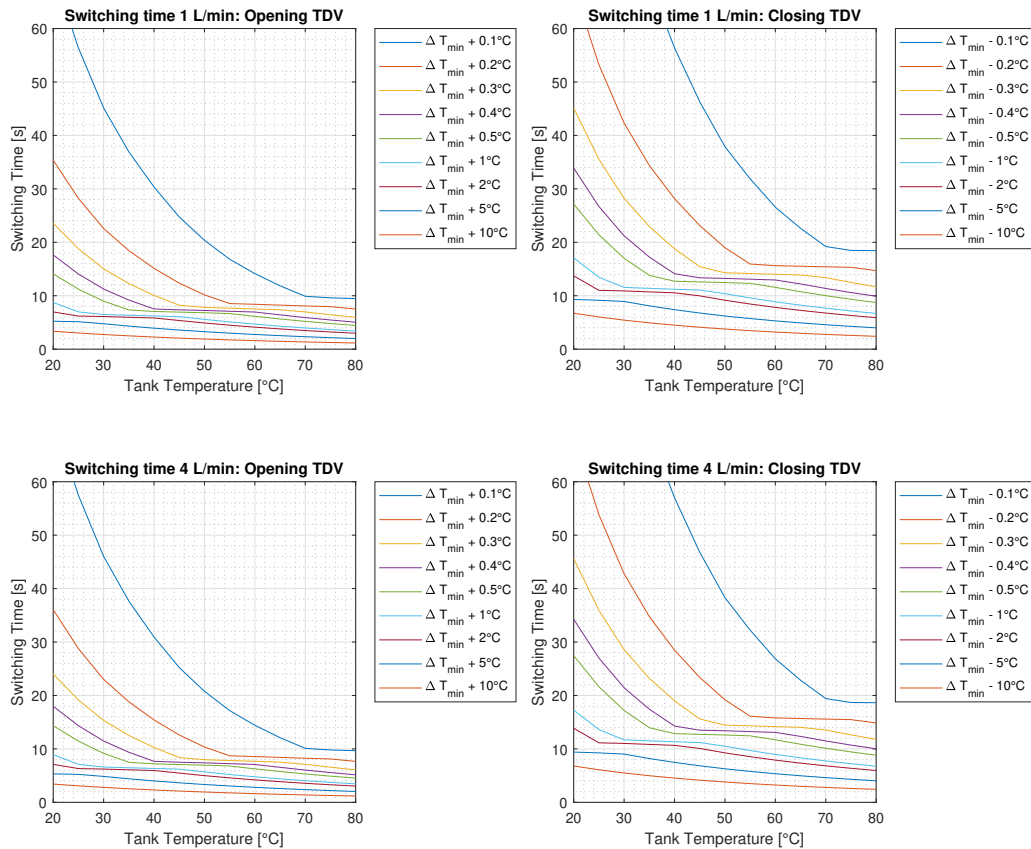


Figure 5.5: Switching times for opening and closing the TDV for flowrates of 1 L/min and 4 L/min. In each sub figure the switching times of different inlet temperatures are presented.



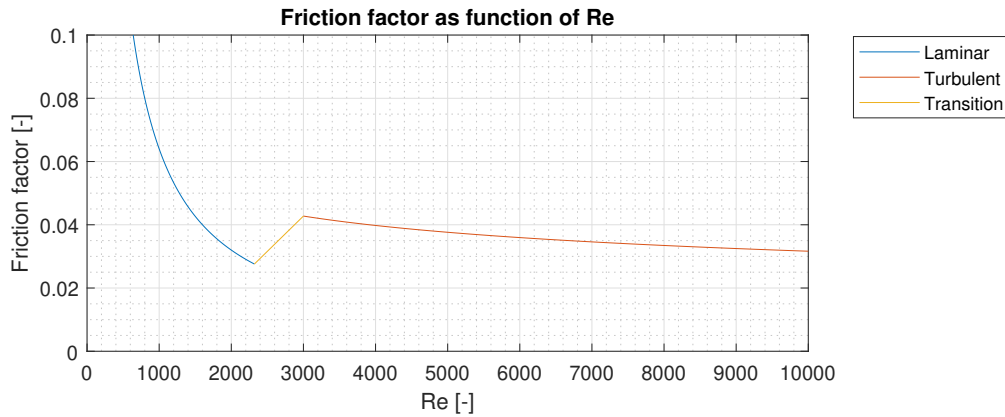


Figure 5.6: Friction factor of the tube of the actuator in laminar, transition and turbulent region.

## 5.2 Experimental results

In table 5.1 the experimental results of the actual temperature difference are presented. Also the number of cycles (samples) and the standard deviation is given in this figure. In these experiments the lower tank temperature was 10°C and the higher tank temperature was 45°C.

As can be observed, all temperature differences for PV800 and PV1000 are significantly higher than the calculated theoretical values at the switching moment of figure 5.2. However, for PV200 the theoretical model very accurately predicts the temperature difference when opening the TDV.

This is probably caused by the fact that during operation of the multi-pass system the inlet temperature of the TDV is never constant. Each time the TDV opens or closes there is a temperature gradient present at the inlet of the TDV. The higher this temperature gradient, the higher these differences can be, because the container of the TDV needs time to heat up. According these experimental results it can be concluded that the thermal inertia of the container (including fluid) is of importance. Therefore, the theoretical static value may deviate from the experimental results. This can also be observed when closing the TDV, since there the gradient is much steeper als the temperature differences are higher.

In figure 5.7 an overview of all process temperatures of the solar circuit of one cycle are presented. The blue dot represents the temperature at which the TDV opens and the blue dot represents the temperature at which the TDV closes. In addition, the presence of a temperature gradient before opening and closing can be clearly observed. It can also be observed that the gradient right before closing the TDV is higher than right before opening the TDV.

Table 5.1: Temperature differences between the inlet of the TDV and the tank temperature during multi-pass. In these experiments  $T_{low} = 10^{\circ}\text{C}$  and  $T_{high} = 45^{\circ}\text{C}$ .

Setting	Flowrate	$\Delta T$ Opening TDV	$\Delta T$ Closing TDV
[-]	[L/min]	[ $^{\circ}\text{C}$ ]	[ $^{\circ}\text{C}$ ]
PV200	1	0,40	4,17
	2	0,34	6,49
	4	0,36	10,68
PV800	1	1,74	4,55
	2	1,34	7,13
	4	1,25	11,14
PV1000	1	1,77	4,84
	2	1,55	7,16
	4	1,43	11,03

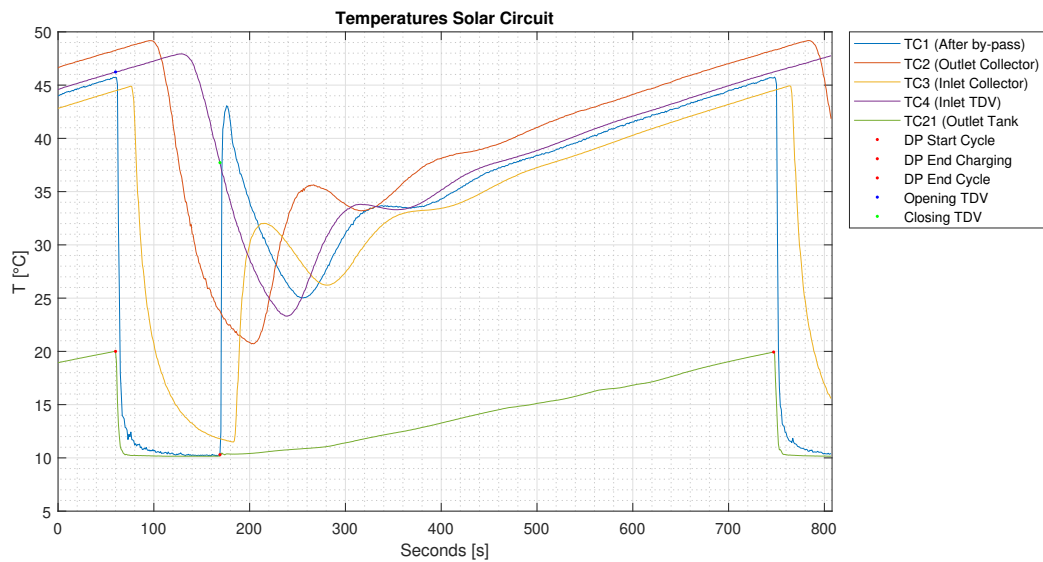


Figure 5.7: Temperatures of the solar circuit during one cycle; PV800; 2 L/min;  $T_{low} = 10^{\circ}\text{C}$ ;  $T_{high} = 45^{\circ}\text{C}$

### Limitations of the model

The thermal inertia of the container and the fluid inside the container are not included in this model. In future research this thermal inertia can be included.

# Chapter 6

## Conclusions and Recommendations

The main goal of this research was to design and built an experimental set-up in order to conduct measurements on the single- and multi-pass mode of the DMP Solar System of Conico Valves.

### 6.1 Conclusions

In this research experiments are conducted in order to determine the thermal- and optical efficiency of an evacuated tube collector during single- and multi-pass mode of the DMP Solar System. Also the total thermal efficiency of the entire system is evaluated for single- and multi-pass mode.

In order to do so, a new experimental set-up has been designed and built in order to run the single- and multi-pass mode of the DMP-Solar system. The set-up is able to capture the dynamic behaviour and complies with the requirements of ISO 9806 norm in all cases except for one. The only requirement which is not met is the requirement regarding the temperature difference. The actual expanded uncertainty is  $\pm 0.14^{\circ}\text{C}$ , while  $\pm 0.05^{\circ}\text{C}$  is required. So if it is required to lower this uncertainty in the future, another calibration set-up need to be used, such as a high quality calibration oven. Lab Technicians are currently conducting some research to realize this in the future. The stability of all process parameters during multi-pass experiments also comply with the ISO 9806 norm.

After the experimental set-up has been built, experiments were conducted to determine the thermal performance of the system. It turned out that there are four parameters which influences the dynamical response of the multi-pass system, namely: flowrate, irradiance and both temperature zones of the tank  $T_{low}$  and  $T_{high}$ . This temperature difference is called the tank temperature difference ( $\Delta T_t$ ). Experiments are conducted with varying flowrate, irradiance and  $\Delta T_t$ . This research does not include variations in  $T_{low}$ . Most of the experiments are conducted with  $\Delta T_t = 35^{\circ}\text{C}$ .

Below conclusions are presented regarding different research subjects.

#### **Temperature distribution in evacuated tubes**

Degenhart showed that no dry-out takes place for single-pass mode at a tilt angle of  $45^{\circ}$ . Since it is shown in this research that the average temperatures inside the evacuated tubes of the multi-pass mode show similar behaviour as for single-pass mode, it can be concluded that no dry-out occurs during multi-pass mode.

By evaluating the temperatures in the evacuates tubes during single-pass mode, it was observed that thermal stratification may play a role. Although Degenhart showed in his CFD model that thermal stratification only starts to occur at flowrates lower than 0.2 L/min, it is observed that during single-pass mode, with a flowrate of approximately 0.3 L/min, thermal stratification already starts to occur. This is probably due to some simplifications in the CFD model. The in- and outflow effects of the collector were not incorporated.

The average temperature difference inside the first evacuated tube during multi-pass mode slightly decreases when increasing the flowrate, resulting in an increase in collector efficiency.

**Thermal efficiency of total system**

It can be concluded that the multi-pass mode operates at higher average temperatures. Due to a higher mean temperature of the collector and thus also a higher average fluid temperature in the entire loop of the system, the multi-pass mode has more heat losses in the piping. Although the multi-pass mode has more heat losses in the piping the total efficiency is still higher than single-pass mode at flowrates higher than approximately 1.5 L/min for PV1000 and 3 L/min for PV800.

**Optical Efficiency**

For  $\Delta T_t = 35^\circ\text{C}$  it can be concluded that by increasing the irradiance from 1200 to 1400  $\text{W}/\text{m}^2$  this results in an increase of 1.4% in optical efficiency. However, for an irradiance of 400  $\text{W}/\text{m}^2$  the opposite was observed. This is probably due to the fact that the temperature difference over the collector is too small, causing high uncertainties (up to 14.4% of the measured value). Therefore, measurements on the multi-pass system with the PV200 setting are not recommended for the multi-pass mode.

In all experiments the thermal- and optical efficiency increases when increasing the flowrate during multi-pass mode.

When analysing the optical efficiency, it can be concluded that the multi-pass mode is 0,4% to 1,7% more efficient for PV800 and 1,6% to 4,7% for PV1000 in worst case scenario. For best the best case scenario these percentages are slightly higher, namely: 2,3% to 5,8% more efficient for PV800 and 2,8% to 6,1% for PV1000.

One experiment is conducted with a lower  $\Delta T_t$  ( $\Delta T_t = 20^\circ\text{C}$ ) concluded to compare low temperature difference between the low- and the high temperature zone of the tank that the optical efficiency does not change significantly when changing  $\Delta T_t$ . However, only 1 measurement series has been conducted for  $\Delta T_t = 20^\circ\text{C}$ , so to confirm this conclusion it is recommended to conduct 1 or 2 extra measurement series in the future.

**TDV**

Furthermore, a solid basis for a model of the TDV has been developed. This model needs to be improved in the future by adding the thermal inertia of the container and the fluid.

## 6.2 Recommendations for future research

**Experimental set-up**

There are some practical recommendations regarding the new test set-up. These can be listed as follows:

- The current settings of all PID controllers are tuned by trial and error to perform the first experiments. Although, the process parameters were very steady during the experiments it would really help to automate the experiments.
- The uncertainties of the efficiencies might be reduced slightly in the future by calibrating the ambient sensors together with the rest of the sensors in the new experimental set-up. Now, 2 different calibration procedures are used (current procedure, and procedure by Degenhart), which causes a slightly higher uncertainty.
- Measurements on the multi-pass system with the PV200 setting are not recommended, since the temperature difference over the collector is too small in this case, causing high uncertainties. It can only be used at very low flowrates. If it is desirable in the future to conduct experiments with PV200, it might be possible to add some extra evacuated tubes to the collector to increase the temperature difference over the collector.
- It is also recommended to use a more powerful pump in the old experimental set-up to increase the flowrate in the primary flow of the hydraulic separator in the cooling circuit.
- It is highly recommended to use a tube stopper for the evacuated tubes in the future, to prevent the heatpipes from sliding down into the evacuated tubes.

- Replacement of the thermocouple in the evacuated tube which measures the absorber temperatures in tangential direction of the fin.

### TRNSYS

This research does not include variations in  $T_{low}$ . However, more of these type of experiments might be conducted in the future to determine the collector coefficients  $a_1$  and  $a_2$ . In this research the parameters  $a_1$  and  $a_2$  of Degenhart are used for the determination of the optical efficiency, but it might be that these coefficients are different during multi-pass mode.

When comparing the temperature response of the in- and outlet temperature of the collector with TRNSYS it can be concluded that thermal capacity of the collector and the piping causes significant differences. These two thermal capacities are not modeled correctly. For future research it might be interesting to conduct research in the possibilities of integrating other dynamic methods proposed in this research into TRNSYS. In this research some methods such as Multi-node approach, Filtering technique with least square method and Improved Transfer function Method are proposed. However, when applying such models it need to be kept in mind that a tremendously amount of experiments need to be conducted in order to validate these models. However, if Conico Valves prefers to use the current model, with some limitations regarding the thermal effective capacity of the collector and the piping more research need to be conduction in how to validate this model with the experimental results. One important issue is the definition of the mean temperature of the collector. The TRNYS model which is developed by Jiang can be further developed in order to validate this model with the new experimental set-up

# Appendix A

## Additional Literature Review

### A.1 Additional literature review regarding steady-state testing

Degenhart [9] also conducted research on stagnant operation with periodic flow. This is determined by conducting experiments and by using a CFD model. It was also concluded that the highest efficiency is gained for the highest possible flow rate, using the 24mm diameter condenser with pure water as the working fluid.

The developed Thermal Resistance Network (TRN) model gave a good insight of the thermal processes inside the solar collector and what kind of parameters influence the thermal processes. However, the comparison with experimental results showed that the TRN did not accurately predict the thermal resistances. This is probably due to some simplifications and unknown thermodynamic conditions inside the heat pipe. Also resistances of the heat pipe and manifold could not be accurately calculated.

Degenhart also conducted experiments on start-stop mode, which is a periodic dynamic condition. The goal was to find the optical efficiency of the stagnant period of the start-stop mode. Therefore, the start-stop cycles were repeated until a steady condition was reached. In these experiments the thermal efficiency is calculated by taking the difference in heat output between 24 and 16 minutes during stagnant operation. However, it is unlikely that the system had reached a steady-stagnant situation by that time. The thermal efficiency is used to determine  $\eta_0$ . It turned out that  $\eta_{0,stag} = 0,572 \pm 0,10$ . The used method has a high uncertainty.

#### Steady state test method external research

As mentioned before, the experiments of Degenhart to determine the collector parameters and the optical efficiency are conducted during steady-state conditions (except for the start-stop experiments). The collector parameters are determined with the Hottel-Whiller Bliss equation, which is thoroughly explained by D. Chwieduk (2014) [8] and A. Kalogirou (2014) [21]. They also clearly indicate that this equation can be applied for ETCs.

Jafarkazemi et al. [14] investigated an evacuated solar heat pipe collector theoretically and experimentally at a tilt angle of 45° during steady-state. The theoretical model is based on energy balance equations and a TRN. The test method is adopted from ISO 9806-1 to compare the theoretical model with the experimental results. This research shows that the theoretical model is in good agreement with the experimental results and is capable of predicting the efficiency, useful energy gain, and working fluid outlet temperature of an evacuated heat pipe collector with good accuracy.

In general, solar collectors can be tested by two basic methods: by using a steady-state test method and by using a dynamic test method. The former method is widely used and the test procedures are well documented in the European standards (NEN-EN-ISO 9806-2017) [1]. For steady-state testing, the environmental conditions and collector operation conditions must be constant during the testing period. For indoor and outdoor experiments with stable weather conditions the required steady conditions are easily satisfied and the testing period requires only a few days. However, in many outdoor locations in the world, steady conditions may be difficult to achieve. For this reason, transient or dynamic test methods have been developed.

## A.2 Additional literature review Quasi-dynamic test method

An ETC can in general be considered as a combination of masses at different temperatures. When an ETC is operating, each component of the ETC responds differently to a change in operating conditions. Therefore, it is useful to consider an **effective thermal capacity** for the entire ETC. However, according to the NEN-EN-ISO 9806-2017 norm it is evident that the effective thermal capacity and the overall time constant may depend on the operating conditions and are not always simple collector parameters with a unique value. Therefore one of the methods including the indicated reference conditions need to be chosen. The measurement of the heat capacity and the time constant need to be conducted using a flow rate similar to that for collector efficiency testing. So it may be that the heat capacity and time constant are a function of flow rate. In the procedure to determine the effective thermal capacity the inlet fluid temperature is kept constant at ambient temperature, while there is no solar irradiation (the collector is covered by a shield). When a steady state is reached the shield is removed and the collector heats up due to the solar irradiation until a second steady state is reached. The transient behaviour of the collector between the two steady-states 1 and 2 is described by equation (A.1).

$$C \frac{dT_m}{dt} = A\eta_{0,hem}G - \dot{m}c_p\Delta T - A_G U(T_m - T_a) \quad (\text{A.1})$$

Then, the effective thermal capacity of the collector can be obtained by integrating over the period of time between the two steady-states conditions, see equation (A.2)

$$C = \frac{A\eta_{0,hem} \int_{t_1}^{t_2} G dt - \dot{m}c_p \int_{t_1}^{t_2} \Delta T dt - A_G U \left[ \int_{t_1}^{t_2} (T_i - T_a) dt + \frac{1}{2} \int_{t_1}^{t_2} \Delta T dt \right]}{T_{m2} - T_{m1}} \quad (\text{A.2})$$

Kalogirou [21] described a 'dynamic test method', which is adopted by EN 12975-2 standard. The EN 12975-2 standard is the predecessor of the NEN-EN-ISO 9806-2017 standard. In this standard it is called a quasi-dynamic test method and is meant for locations that do not have steady environmental conditions for long periods of time. After the experiments, the collected data (over a wide range of operating conditions) are fitted to a transient mathematical model of the collector performance. The useful thermal power in transient conditions is proposed by Morrison (2001), see equation (A.3):

$$Q_u = \eta_0 G - a_0(T_m - T_a) - a_1(T_m - T_a)^2 - C \frac{dT_m}{dt} \quad (\text{A.3})$$

Equation (A.3) is a time-dependent mathematical model and can be used to identify the collector performance parameters from the transient data. In addition, this equation is similar to the second-order equations used for steady-state testing, but with the addition of a transient term. This equation is proposed by Morrison because a lot of outdoor test setups are located somewhere in the world where steady state conditions may be difficult to achieve. The solar irradiation in these cases may change over time. During these transient tests the collector performance need to be monitored for a range of irradiation. An advantage of this transient method is that it can be applied to determine a wider range of collector performance parameters than the steady state method.

The primary difference between the steady state method and the dynamic method is that, in the dynamic method, the data are recorded on a continuous basis over a day and averaged over 5–10 min. It is likely that this dynamic method may displace the steady-state testing method, even for locations that have clear and stable climatic conditions. That is due to the wider range of collector parameters that can be determined with the dynamic method. S. A. Kalogirou also presents a method to determine the time constant of the system, which is a measure for the effective thermal capacity of the collector.

Facão et al. [17] analysed a plate heat pipe collector numerically and experimentally. The numerical model is based on energy balance equations assuming a quasi-steady state condition. In the numerical model the major simplification is that the temperature in the heat pipe was considered to be uniform and equal to the saturation temperature. Two types of experiments are conducted: the first experiment is the determination of the instantaneous efficiency curve and the second experiment is the determination of the collector time constant, which is a measure of its thermal inertia. Results showed a collector optical efficiency of 0.64 and a time constant of 410 seconds. According to J. Facão et al. this time constant is assumed to be low enough to confirm a quasi-steady state condition. There was a good agreement between numerical and experimental results.

Fisher et al. [6] made a comparison between experimental determination of the collector parameters of the quasi-dynamic test method and the steady state method. The methods can be applied for ETCs and all other thermal collectors on the market except for integral collector storage (ICS) collectors. In both cases the yearly gain is calculated with the simulation tool TRNSYS by implementing the experimentally determined collector parameters. It turned out that the yearly energy is approximately 2% higher with the quasi-dynamic method, but this is basically due to the missing handling of the diffuse irradiation in the steady-state method. S. Fisher et al. used Multi Linear Regression (MLR) for the identification of the collector parameters.

Mahmoud Elsheniti et al. [25] developed a mathematical model of an ETC with heat pipe and validated it experimentally under weather conditions of Alexandria, Egypt. The model is also upgraded by adding a transient term and by considering the effect of the effective thermal capacity of the system. Mahmoud B. Elsheniti et al. concluded that the relative error between the experimental and theoretical results were reduces from 12.5% to 4.4% by considering this effective thermal capacity. The time dependent mathematical model is based on energy balance equations and a TRN model.

## A.3 Dynamic test method

### A.3.1 Dynamic test method: one-node approach

Duffie and Beckman [20] state that the operation of most solar energy systems is inherently transient. In practice there does not exist steady-state operation when considering the transient nature of the driving forces. Therefore, they studied the effects of the thermal capacity in transient conditions, with a one-node approach. Wijeysondera (1978) compared this one-node approach with a two-node approach. The effect of the thermal capacity can be estimated by solving the transient energy balance equations for various parts of the collector. To illustrate this method, they considered a flat-plate collector with a single-cover. In this one-node approach it is assumed that the absorber plate, the water in the tubes, and one-half of the back insulation are all at the same temperature ( $T_p$ ). It is also assumed that the cover is at a uniform temperature ( $T_c$ ) that is different from  $T_p$ . Two transient energy balances are combined into equation (A.4).

$$\left[ (mC)_p + \frac{U_L}{U_{c-a}} (mC)_c \right] \frac{dT_p}{dt} = A_c [S - U_L(T_p - T_a)] \quad (\text{A.4})$$

The term at the left hand side of the equation in square brackets represents the effective thermal capacity of the collector. This term can be extended if more components, with its own transient energy balance, are taken into consideration, see equation (A.5). In this case a collector with n covers can be considered.

$$(mC)_e = (mC)_p + \sum_{i=1}^n a_i (mC)_{c,i} \quad (\text{A.5})$$



### A.3.2 Dynamic test method: multi-node approach

In the quasi-dynamic test method described in the EN 12975-2 standard and the NEN-EN-ISO 9806-2017 standard a typical one-node approach is used, which means that the collector including working fluid can be seen as one unit. In this case the effective collector thermal capacity is lumped and is referenced by the collector mean fluid temperature ( $T_m$ ).

#### Filtering technique with least square method

However, also multi-node test methods exist. One example is the method of J. Muschaweck and W. Spirkel (1990) [29] [18]. They developed a dynamic test method using a combination of filtering theory and the least square method. In this method the solar collector is divided into several units with its own energy conservation equation. One important advantage is that this method has no requirements on the variations of the fluid flow rate, fluid inlet temperature, surrounding air temperature and solar irradiance. A second advantage is that this method is more accurate than the lumped method. However, the digital filtering method is complicated. Nayak and Amer (2000) [11] showed, by performing experiments, that this method can accurately predict the fluid outlet temperature. However, it cannot determine the collector parameters.

#### Laplace transform technique

Amer et al. (1999) [12] introduced a new dynamic test method that uses the Laplace transform technique to get an analytical solution for the fluid temperature. The main assumption of this method is that the effective thermal capacity is uniformly distributed over the collector. This test method only requires a constant flow rate during the test. An advantage is that the results of the parameter estimation can be compared with steady state test results. The predicted outlet temperature is quite accurate. However, this test method requires complex math calculations and many experiments.

#### Improved Transfer function Method

One dynamic method for solar thermal collectors with the most advantages for this research is the improved transfer function method. It is proved that this method can handle a varying inlet temperature, resulting in dynamic behaviour. This method was first presented by Hou (2004). He combined two energy conservation equations to eliminate the absorber temperature into a second-order differential equation. Then Wang (2008) improved this method by using the arithmetic mean value of the in- and outlet temperatures instead of just the fluid temperature and he derived the same second-order differential equation, but with less model parameters. Finally, Xu (2009) derived a transfer function model using Hou's method, but with more precise mathematical method. To determine the transient collector parameters a Multiple Linear Regression (MLR) technique is used, which is much easier to use than the filter method with the least square method and the Laplace transform technique. The following papers that are described below are based on the improved transfer function method.

W. Kong and Z. Wang et al. (2012) [32] presented the results of a series of experiments to illustrate the improved transfer function method. The experiments are compared with the numerical solutions of the mathematical transfer function model. An analysis of the errors between the numerical predicted- and measured fluid outlet temperatures is made. Considering various test conditions show that the improved transfer function method can accurately predict the fluid outlet temperature. It is concluded that the average error is less than 1°C for unsteady test conditions. In addition, the transfer function method model does not need to assume a particular kind of solar collector. Thus, it can be applied for flat-plate and ETCS. Finally, the transfer function method is evaluated to provide improvements in future designs.

L. Xu, Z. Wang et al. (2012) [24] used the improved transfer function method for an all-glass ETC with air as heat HTF under dynamic conditions. To achieve dynamic cases they varied the inlet temperature sharply by controlling the heater and they also periodically used a shield to block the solar irradiation. The massflow should be constant during the experiments. During all tests the data is acquired on a 10 seconds interval to capture the transient conditions. In the

first test the measured data is used to identify the model parameters. This is done by regressing the standardized form of the linear differential equation, see equation (A.8). Then two other test are conducted to check if the model with the regressed collector parameters match with other experimental results. It can be concluded that the improved transfer function method can accurately determine the collector parameters in order to calculate the outlet temperature of the collector. It can also give information about the thermal performance of the collector. The maximum error between the model and the experiments was 2.39%.

W. Kong and Z. Wang. et al. [31] compared the improved transfer function method with the quasi-dynamic method proposed in NEN-EN-ISO 9806-2017. This is done for a flat plate collector and an ETC. Because lacking of experimental data of ETC's some artificial experiments are carried out with TRNSYS (the validated Type 832 model under real weather conditions). It can be concluded that the improved transfer function method can accurately determine the collector parameters for flat plate collectors and investigations indicate that this method is also suitable for ETC's. However, real experiments with ETC's need to be conducted in the future instead of the artificial experiments in TRNSYS.

The improved transfer function method is based on a two-node method, because the collector is divided into two main parts: the solid part (the collector) and the fluid part. Both parts are described by the transient energy balance. The collector part is described by equation (A.6) and the fluid part is described by equation (A.7).

$$m_b c_b \frac{dT_b}{dt} = F_R (\tau \alpha)_{en} A_a G - A_f U_{bf} (T_b - T_f) - A_{am} U_{ba} (T_b - T_a) \quad (A.6)$$

$$m_f c_f \frac{dT_f}{dt} = A_f U_{bf} (T_b - T_f) - \dot{m} c_f (T_o - T_i) \quad (A.7)$$

With subscript b = collector, f = fluid, a = ambient, o and i = out- and inlet temperature of the collector. And with  $A_a$  = aperture area [ $m^2$ ],  $F_R$  = the heat removal factor [-],  $m$  = mass [ $kg$ ],  $c$  = specific heat capacity [ $J/(kgK)$ ],  $U_{xy}$  = overall heat loss coefficient from x to y [ $W/(m^2K)$ ],  $T$  = temperature [ $^{\circ}C$ ].

By adding equation (A.6) and (A.7) and eliminating  $T_b$ , a second order linear differential equation can be obtained:

$$\frac{d^2 T_o}{dt^2} + A \frac{dT_o}{dt} + B(T_o - T_i) = C \frac{dT_i}{dt} + EG - F(T_i - T_a) \quad (A.8)$$

With its coefficients expressed in equation (A.9), (A.10), (A.11), (A.12), (A.13) and (A.14).

$$A = \frac{1 + \dot{m} c_f R_{bf}}{C_f R_{bf}} + \frac{R_{bf} + R_{ba}}{C_b R_{bf} R_{ba}} \quad (A.9)$$

$$B = \frac{1 + (R_{bf} + R_{ba}) \dot{m} c_f}{C_b C_f R_{bf} R_{ba}} \quad (A.10)$$

$$C = \frac{\dot{m} c_f}{C_f} \quad (A.11)$$

$$D = \frac{(R_{bf} + R_{ba}) \dot{m} c_f}{C_b C_f R_{bf} R_{ba}} \quad (A.12)$$

$$E = \frac{F_R(\tau\alpha)_{en}A_a}{C_bC_fR_{bf}} \quad (\text{A.13})$$

$$F = \frac{1}{C_bC_fR_{bf}R_{ba}} \quad (\text{A.14})$$

with  $R_{ba} = 1/(A_{am}U_{ba})$  and  $R_{bf} = 1/(A_fU_{bf})$ .

By rewriting equation (A.8), the instantaneous thermal efficiency can be obtained:

$$\eta = -\frac{\dot{m}c_f}{BGA_a} \left( \frac{d^2T_o}{dt^2} + A \frac{dT_o}{dt} - C \frac{dT_i}{dt} \right) + \frac{E\dot{m}c_f}{BA_a} - \frac{F\dot{m}c_f}{BA_a} T^* \quad (\text{A.15})$$

With  $T^* = (T_o - T_i)/G =$  the reduced temperature difference

This instantaneous thermal efficiency proves that there is a close relationship between the transient model and the first order model if the transient terms are eliminated from equation (A.15):

$$\eta = \eta_0 - a_1 T^* \quad (\text{A.16})$$

With  $\eta_0 = E\dot{m}c_f/(BA_a)$  and  $a_1 = F\dot{m}c_f/(BA_a)$ .

# Appendix B

## Additional Results

### B.1 Additional Results Multi-Pass Mode

Table B.1: Multi-Pass results part 1

Settings	MD	$G$	$\dot{V}$	$T_{m,c}$	$T_{a,c}$	$T_{a,setup}$	$T_{red}$
[-]	[-]	[W/m <sup>2</sup> ]	[L/min]	[°C]	[°C]	[°C]	[m <sup>2</sup> K/W]
<b>PV200</b> $T_{low} = 10^{\circ}\text{C}$ $T_{high} = 45^{\circ}\text{C}$	2	410	1,00	37,59	25,19	23,11	0,030
	2	409	2,00	37,67	25,25	23,16	0,030
	2	410	4,00	37,53	24,97	22,88	0,031
	1	406	1,00	37,64	24,91	23,15	0,031
	1	406	2,00	37,61	25,01	23,19	0,031
<b>PV800</b> $T_{low} = 10^{\circ}\text{C}$ $T_{high} = 45^{\circ}\text{C}$	3	1206	1,00	35,90	29,52	25,04	0,0053
	3	1239	4,00	35,86	30,21	25,18	0,0046
	2	1177	1,00	35,86	28,28	23,82	0,0064
	2	1176	2,00	35,97	28,69	24,09	0,0062
	2	1212	4,00	35,86	29,19	24,59	0,0055
	1	1193	1,00	36,01	28,53	23,78	0,0063
	1	1179	2,00	35,98	28,36	23,60	0,0065
	1	1180	4,00	35,84	28,04	23,42	0,0066
<b>PV1000</b> $T_{low} = 10^{\circ}\text{C}$ $T_{high} = 45^{\circ}\text{C}$	4	1369	1,00	36,16	30,07	24,81	0,0044
	4	1369	2,00	35,80	30,38	25,03	0,0040
	4	1369	4,00	35,71	30,35	24,90	0,0039
	3	1366	1,00	35,96	28,52	23,72	0,0054
	3	1355	2,00	35,81	28,91	23,89	0,0051
	3	1379	4,00	35,75	29,09	24,04	0,0048
	2	1359	4,00	35,71	28,35	23,37	0,0054
	1	1361	1,00	36,27	27,16	22,08	0,0067
	1	1381	2,00	36,12	27,51	22,40	0,0062
<b>PV800</b> $T_{low} = 20^{\circ}\text{C}$ $T_{high} = 40^{\circ}\text{C}$	1	1190	1,00	34,40	28,14	23,56	0,0053
	1	1191	2,00	34,59	28,49	23,78	0,0051
	1	1180	4,00	34,52	28,52	23,88	0,0051

Table B.2: Multi-Pass results part 2

PV Setting	MD	$\dot{V}$	$\dot{Q}_{c,i}$	$\dot{Q}_{c,o}$	$\dot{Q}_t$	$\dot{Q}_{loss}$	$\eta_{th}$	$\eta_{th,tot}$	$\eta_o$
[-]	[-]	[L/min]	[W]	[W]	[W]	[W]	[-]	[-]	[-]
<b>PV200</b> $T_{low} = 10^\circ\text{C}$ $T_{high} = 45^\circ\text{C}$	2	1,00	380	262	213	49	0,69	0,56	0,76
	2	2,00	379	272	216	56	0,71	0,57	0,78
	2	4,00	380	287	225	62	0,76	0,59	0,82
	1	1,00	377	263	212	51	0,70	0,56	0,77
	1	2,00	376	276	218	59	0,73	0,58	0,80
<b>PV800</b> $T_{low} = 10^\circ\text{C}$ $T_{high} = 45^\circ\text{C}$	3	1,00	1118	820	800	21	0,73	0,72	0,74
	3	4,00	1148	855	835	19	0,74	0,73	0,75
	2	1,00	1091	811	778	34	0,74	0,71	0,76
	2	2,00	1090	820	782	38	0,75	0,72	0,76
	2	4,00	1123	861	823	37	0,77	0,73	0,78
	1	1,00	1106	826	795	31	0,75	0,72	0,76
	1	2,00	1093	824	790	34	0,75	0,72	0,77
	1	4,00	1093	848	815	34	0,77	0,74	0,79
<b>PV1000</b> $T_{low} = 10^\circ\text{C}$ $T_{high} = 45^\circ\text{C}$	4	1,00	1269	943	923	20	0,74	0,73	0,75
	4	2,00	1269	955	932	23	0,75	0,73	0,76
	4	4,00	1269	974	951	22	0,77	0,75	0,78
	3	1,00	1265	944	914	30	0,75	0,72	0,76
	3	2,00	1256	956	928	28	0,76	0,74	0,77
	3	4,00	1278	988	952	35	0,77	0,75	0,78
	2	4,00	1260	980	947	33	0,78	0,75	0,79
	1	1,00	1261	947	905	42	0,75	0,72	0,77
	1	2,00	1280	972	931	41	0,76	0,73	0,77
<b>PV800</b> $T_{low} = 20^\circ\text{C}$ $T_{high} = 40^\circ\text{C}$	1	1,00	1103	824	797	27	0,75	0,72	0,76
	1	2,00	1104	832	805	27	0,75	0,73	0,77
	1	4,00	1094	837	818	19	0,77	0,75	0,78

## B.2 Results Process Parameters

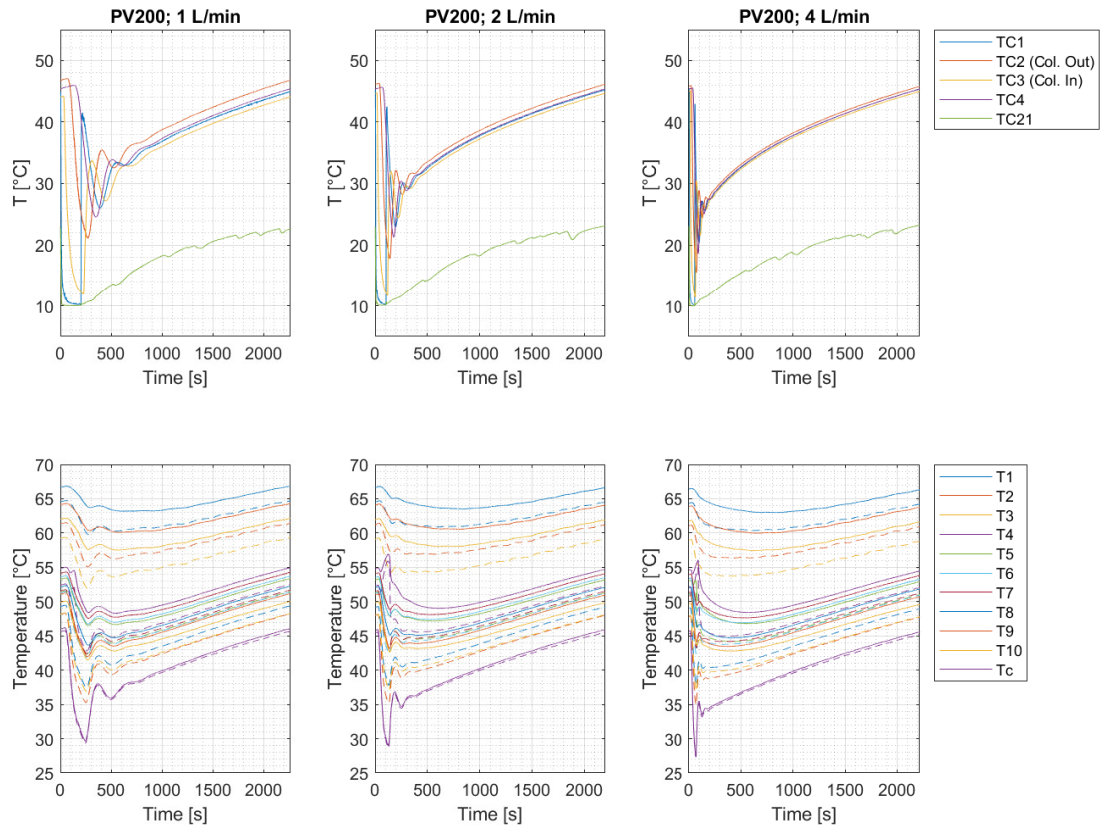


Figure B.1: Top: Process temperatures Solar Circuit. Bottom: Temperatures inside first evacuated tube, solid lines are absorber temperatures and dashed lines are evaporator temperatures. Conditions: PV200,  $T_{low} = 10^{\circ}\text{C}$ ,  $T_{high} = 45^{\circ}\text{C}$

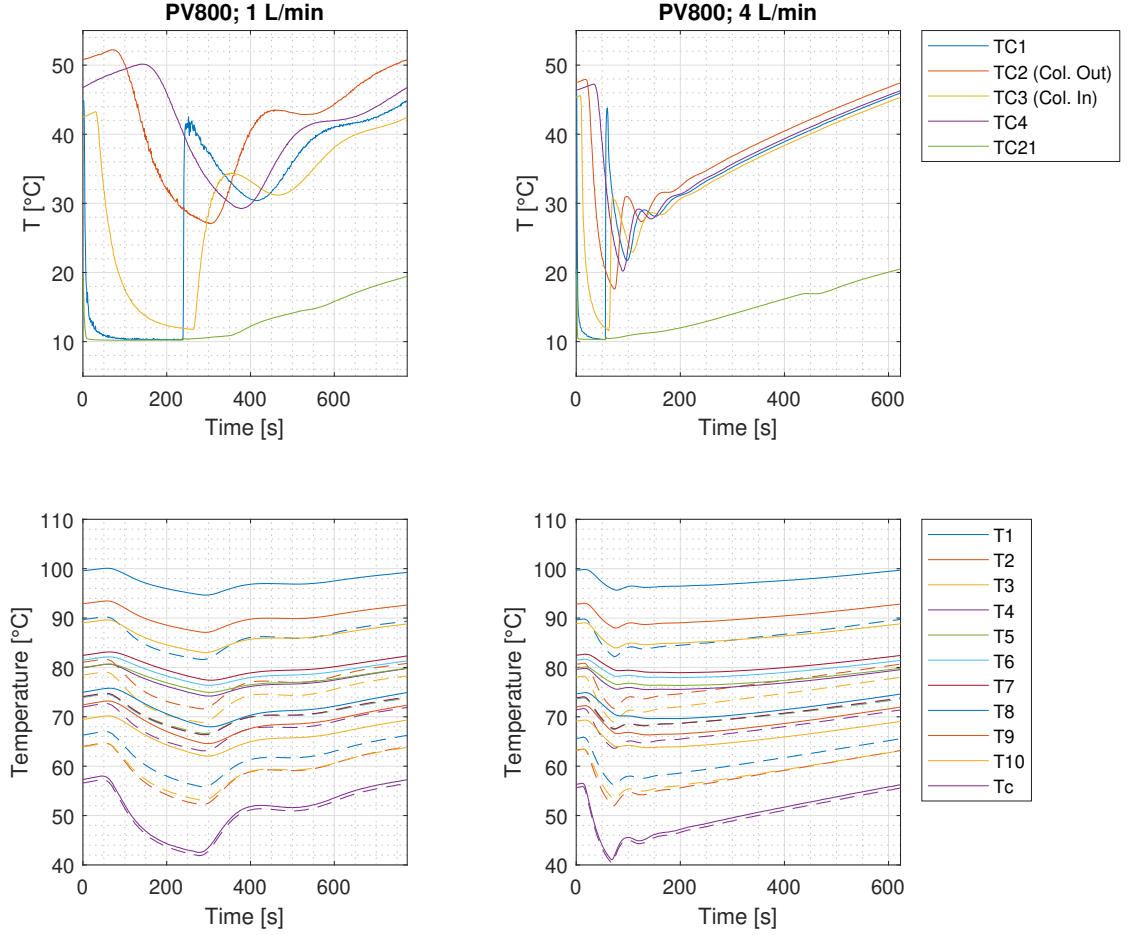


Figure B.2: Top: Process temperatures Solar Circuit. Bottom: Temperatures inside first evacuated tube, solid lines are absorber temperatures and dashed lines are evaporator temperatures. Conditions: PV800,  $T_{low} = 10^{\circ}\text{C}$ ,  $T_{high} = 45^{\circ}\text{C}$

### B.3 Thermal efficiency collector

The shape of all curves and the position with respect to each other are similar to the curves of the optical efficiency. The values for the optical efficiency are only corrected with  $T_{red}$ . Since  $T_{red}$  is higher for PV200 comparing to PV800 and PV1000, the optical efficiency for PV200 is corrected with an higher amount.

Also here it can clearly be observed that at the measurement days which are conducted in January (MD2, MD3 and MD4 for PV200, PV800 and PV1000 respectively) a lower thermal efficiency of the collector exists. However, the irradiance  $G$ ,  $T_{m,c}$ ,  $T_{a,c}$ ,  $T_{a,setup}$  (see table B.1) are approximately identical for each measurement, which indicates that there are some mechanical issues. The reason behind this phenomenon is explained in section 4.1.5.

In figure B.4 a steep gradient can be observed for PV200, which is definitely not expected. Even the thermal efficiency at 4 L/min is higher at PV200 than at PV800. According to literature and research by Degenhart [9] it was expected that the thermal efficiency for lower irradiances are always lower than higher irradiances. The rational behind this phenomenon is explained in section

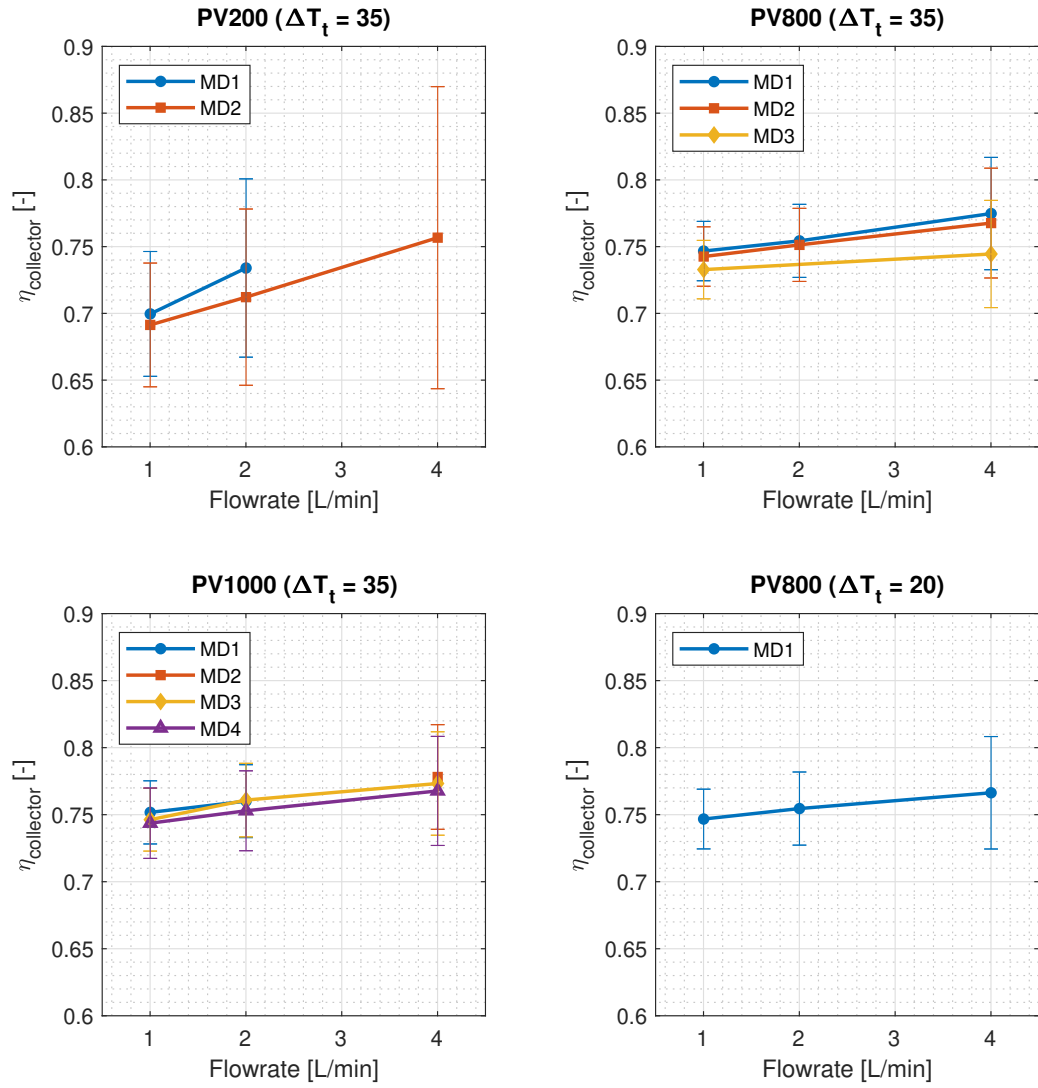


Figure B.3: Thermal efficiency collector vs. flowrate for multi-pass mode. For  $\Delta T_t = 35^\circ\text{C}$  a  $T_{low}$  of  $10^\circ\text{C}$  is used and for  $\Delta T_t = 20^\circ\text{C}$  a  $T_{low}$  of  $20^\circ\text{C}$  is used.



4.1.5.

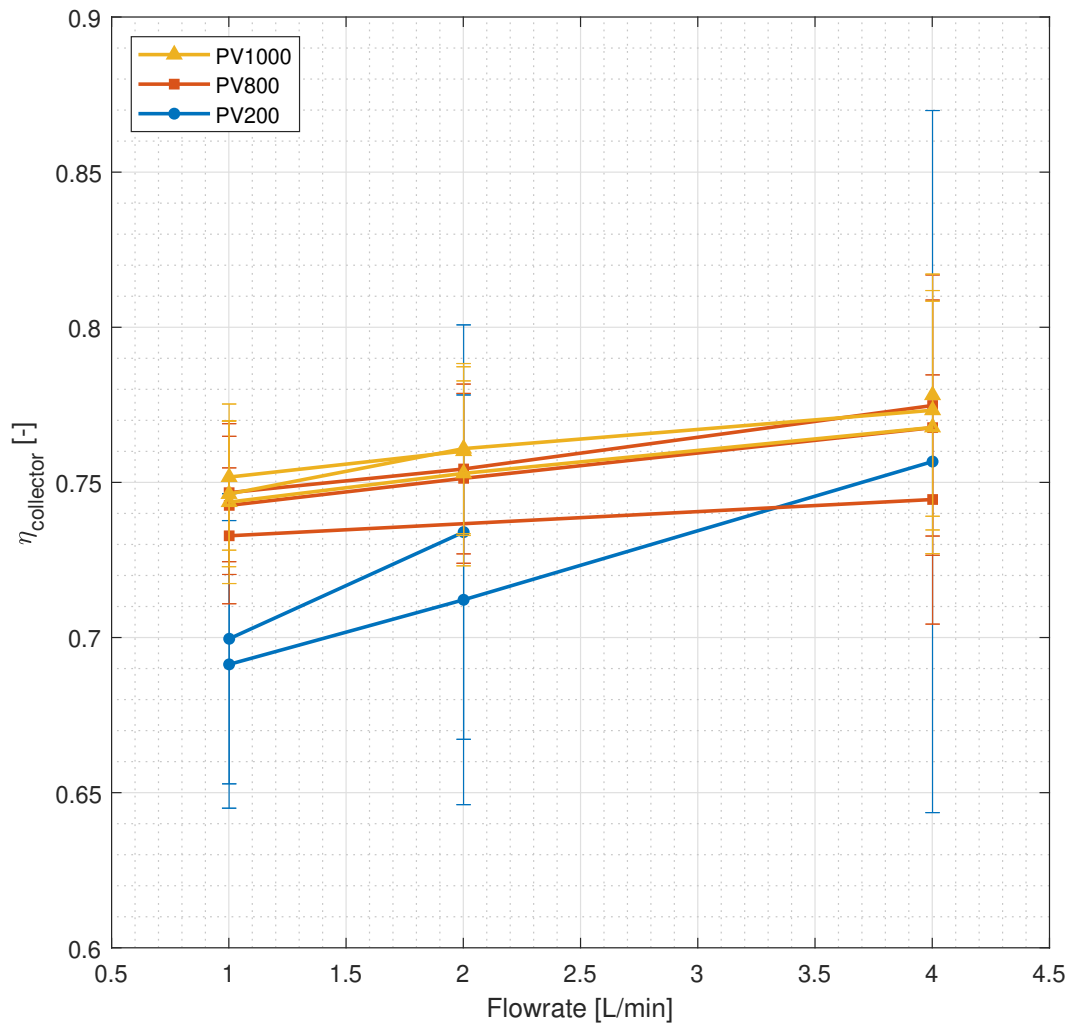


Figure B.4: Thermal efficiency collector vs. flowrate for multi-pass mode (all measurement combined in one figure. For  $\Delta T_t = 35^\circ\text{C}$  a  $T_{low}$  of  $10^\circ\text{C}$  is used and for  $\Delta T_t = 20^\circ\text{C}$  a  $T_{low}$  of  $20^\circ\text{C}$  is used.

# Appendix C

## TRNSYS Output

Figure C.1 shows a simulation result of the DMP Solar System operating in a typical spring day. This model is developed by Jiang [19]. During 1 cycle it can be observed that an equal stair shape pattern occurs. This is due to the fact that the effective thermal capacity of the collector is modelled as the thermal capacity of the fluid and not as a combined thermal capacity of the fluid and collector material. It can also clearly be observed that the stair shape patterns do not dampens out during the cycle, which is can be caused by the fact that the thermal capacity of the piping is not included in the model.

It can also be observed that the mean temperature of the collector  $T_m$  is approximately the average of  $T_{low}$  and  $T_{high}$ , see equation (C.1).

$$T_m \approx \frac{T_{low} + T_{high}}{2} \quad (C.1)$$

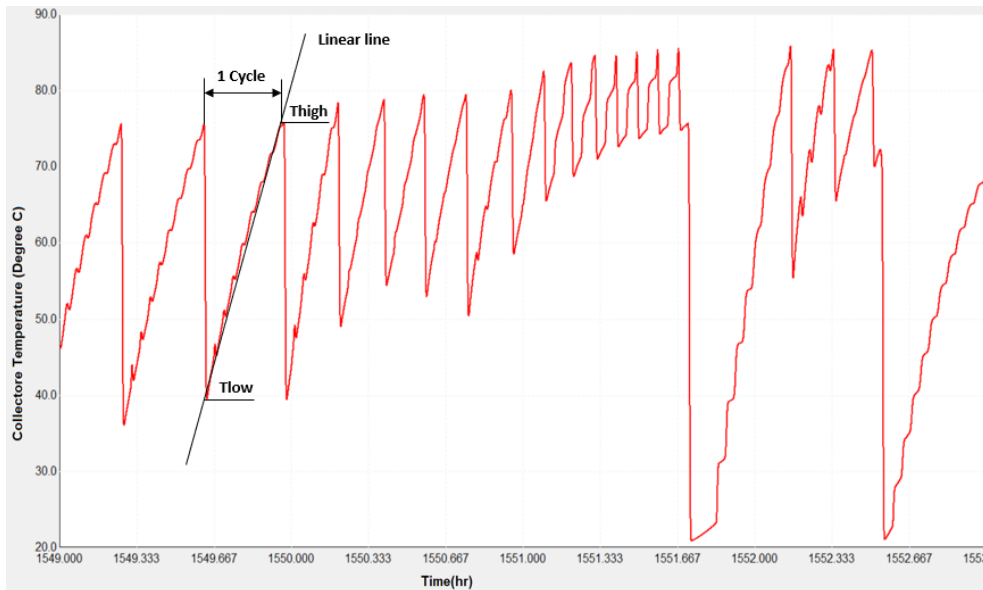


Figure C.1: Simulation result of the DMP Solar System in TRNSYS. The model is based on a Type 538 Evacuated tube collector and is developed by Jiang [19]

### Validation TRNSYS with experimental results

The work of Jiang can be adopted to have a solid basis for a reference system. The TRNSYS model of Jiang may be further developed in the future in order to validate the model with experimental results.

As explained in chapter ?? there are some experimental methods to determine the thermal performance of an ETC during dynamic conditions, namely:

- Quasi-dynamic test method
- One-node approach

- Multi-node approach
- Filtering technique with least square method
- Laplace transform technique
- Improved Transfer function Method

For future research it might be interesting to conduct research in the possibilities of the methods described above. To validate such models a tremendously amount of experiments need to be conducted in order to validate these models and for the scope of this research this is not possible. Designing, building and commissioning the new test-setup already took approximately 75% of the time. Also due to the Corona measures and a shortage of lab technicians there was no help available to built and commission the set-up, therefore, this process took longer than initially expected.

# Appendix D

## Calibration Results

The linear fit is realised by using equation (D.1).

$$T_{Measured,Uncalibrated} = aT_{Calibrated} + b \quad (D.1)$$

Table D.1: Calibration results of thermocouples TC1-TC5. Also the coefficients a and b for the linear fit are presented. The goodness of the fit is characterised by R<sup>2</sup>.

	Reference	Uncalibrated					Units
	TC	TC1	TC2	TC3	TC4	TC5	
	0,54	0,42	0,39	0,36	0,37	0,37	°C
	23,12	23,45	23,33	23,32	23,31	23,33	°C
	29,97	30,29	30,14	30,15	30,13	30,17	°C
	39,87	40,2	39,95	40	39,93	40,02	°C
	49,8	50,12	49,77	49,87	49,73	49,88	°C
	59,82	60,06	59,62	59,75	59,58	59,78	°C
	69,83	69,97	69,47	69,65	69,46	69,64	°C
	79,85	79,81	79,25	79,5	79,28	79,43	°C
	89,97	89,8	89,37	89,58	89,4	89,43	°C
a		0,9979	0,9918	0,9951	0,9923	0,9937	-
b		0,2552	0,239	0,1742	0,2008	0,2274	°C
R <sup>2</sup>		1	1	1	1	0,9999	-

Table D.2: Calibration results of thermocouples TC1-TC5. Also the coefficients a and b for the linear fit are presented. The goodness of the fit is characterised by R<sup>2</sup>.

	Reference	Uncalibrated					Units
	TC	TC1	TC2	TC3	TC4	TC5	
	0,5	0,4	0,4	0,4	0,4	0,4	°C
	23,1	23,4	23,3	23,3	23,3	23,3	°C
	30,0	30,3	30,1	30,1	30,1	30,2	°C
	39,9	40,2	40,0	40,0	39,9	40,0	°C
	49,8	50,1	49,8	49,9	49,7	49,9	°C
	59,8	60,1	59,6	59,8	59,6	59,8	°C
	69,8	70,0	69,5	69,6	69,5	69,6	°C
	79,9	79,8	79,2	79,5	79,3	79,4	°C
	90,0	89,8	89,4	89,6	89,4	89,4	°C
a		0,9979	0,9918	0,9951	0,9923	0,9937	-
b		0,2552	0,2390	0,1742	0,2008	0,2274	°C
R <sup>2</sup>		1,0000	1,0000	1,0000	1,0000	0,9999	-

APPENDIX D. CALIBRATION RESULTS

Table D.3: Calibration results of thermocouples TC6-TC13. Also the coefficients a and b for the linear fit are presented. The goodness of the fit is characterised by  $R^2$ .

Ref.	Uncalibrated								Unit
TC	TC6	TC7	TC8	TC9	TC10	TC11	TC12	TC13	
0,54	0,15	0,13	0,45	0,42	0,35	0,14	0,13	0,42	°C
21,49	21,43	21,42	21,72	21,66	21,70	21,49	21,48	21,77	°C
29,97	29,99	29,98	30,27	30,21	30,27	30,06	30,04	30,33	°C
39,89	39,93	39,92	40,20	40,15	40,21	40,00	39,99	40,26	°C
49,80	49,86	49,85	50,12	50,07	50,12	49,93	49,91	50,18	°C
59,82	59,78	59,78	60,04	60,00	60,05	59,86	59,84	60,10	°C
69,83	69,66	69,64	69,89	69,86	69,92	69,74	69,71	69,97	°C
79,85	79,51	79,51	79,74	79,71	79,77	79,60	79,56	79,82	°C
89,87	89,36	89,37	89,59	89,54	89,63	89,45	89,42	89,66	°C
a	0,9976	0,9978	0,9968	0,9969	0,9981	0,9986	0,9983	0,9977	-
b	-0,0382	-0,0563	0,262	0,213	0,1984	-0,0176	-0,0268	0,2717	°C
$R^2$	1	1	1	1	0,9999	0,9999	0,9999	0,9999	-

Table D.4: Calibration results of thermocouples TC14-TC20. Also the coefficients a and b for the linear fit are presented. The goodness of the fit is characterised by  $R^2$ .

Reference	Uncalibrated							Unit
TC	TC14	TC15	TC16	TC17	TC18	TC19	TC20	
0,54	0,39	0,37	0,42	0,39	0,37	0,43	0,39	°C
21,49	21,75	21,72	21,77	21,76	21,73	21,79	21,75	°C
29,97	30,31	30,28	30,34	30,32	30,30	30,35	30,32	°C
39,89	40,25	40,22	40,27	40,26	40,25	40,29	40,26	°C
49,80	50,17	50,13	50,19	50,18	50,17	50,21	50,18	°C
59,82	60,09	60,05	60,11	60,11	60,11	60,14	60,11	°C
69,83	69,97	69,91	69,97	69,98	69,98	70,00	69,98	°C
79,85	79,82	79,76	79,82	79,83	79,85	79,87	79,83	°C
89,87	89,67	89,63	89,70	89,69	89,73	89,73	89,72	°C
a	0,9981	0,9978	0,9979	0,9983	0,9989	0,9983	0,9985	-
b	0,2428	0,2231	0,2715	0,2468	0,2148	0,2773	0,2377	°C
$R^2$	0,9999	0,9999	0,9999	0,9999	0,9999	0,9999	0,9999	-

Table D.5: Calibration results of thermocouples TC21-TC22. Also the coefficients a and b for the linear fit are presented. The goodness of the fit is characterised by  $R^2$ .

	Reference	Uncalibrated		Units
	TC	TC21	TC22	
	0,54	0,27	0,48	°C
	18,63	18,83	18,90	°C
	29,97	30,29	30,24	°C
	39,89	40,22	40,04	°C
	49,90	50,14	49,80	°C
	59,92	60,07	59,55	°C
	69,94	69,97	69,32	°C
	79,95	79,82	79,25	°C
	90,07	89,72	89,24	°C
<b>a</b>		0,9974	0,9877	-
<b>b</b>		0,1832	0,3768	°C
<b>R<sup>2</sup></b>		0,9999	0,9999	-

**Thermocouple Calibration by Degenhart**

Remark: Degenhart defined the a and b coefficient differently, see equation (D.2).

The A1-A4 for sensors represent the ambient temperatures and the rest are the thermocouples inside one evacuated tube.

$$T_{Calibrated} = aT_{Measured,Uncalibrated} + b \tag{D.2}$$

Table D.6: Thermocouple calibration results of Degenhart

TC	a	b	urandom	TC	a	b	urandom
<b>A1</b>	-0.0060	-0.1100	0.0024	<b>T5a</b>	-0.0024	-0.3100	0.0010
<b>A2</b>	-0.0020	-0.2167	0.0028	<b>T5e</b>	-0.0039	-0.2250	0.0012
<b>A3</b>	-0.0044	-0.1800	0.0027	<b>T6a</b>	-0.0039	-0.2683	0.0014
<b>A4</b>	-0.0058	-0.1833	0.0018	<b>T6e</b>	-0.0021	-0.4283	0.0014
<b>cb</b>	0.0043	-0.1027	0.0012	<b>T7a</b>	-0.0051	-0.2267	0.0016
<b>ct</b>	-0.0012	0.0215	0.0021	<b>T7e</b>	-0.0036	-0.3600	0.0018
<b>T1a</b>	-0.0017	-0.2250	0.0012	<b>T8a</b>	-0.0026	-0.1983	0.0020
<b>T1e</b>	-0.0032	-0.1417	0.0022	<b>T8e</b>	-0.0026	-0.1550	0.0020
<b>T2a</b>	-0.0022	-0.2600	0.0013	<b>T8b</b>	-0.0004	0.0321	0.0010
<b>T2e</b>	-0.0021	-0.3150	0.0008	<b>T8c</b>	-0.0021	0.0021	0.0021
<b>T3a</b>	-0.0024	-0.3100	0.0010	<b>T9a</b>	-0.0018	-0.0967	0.0016
<b>T3e</b>	-0.0039	-0.2250	0.0012	<b>T9e</b>	0.0019	-0.2550	0.0011
<b>T4a</b>	-0.0039	-0.2683	0.0014	<b>T10e</b>	-0.0030	0.1983	0.0006
<b>T4e</b>	-0.0021	-0.4283	0.0014	<b>T10a</b>	-0.0026	0.2250	0.0017

# Appendix E

## Uncertainty analysis

### E.1 Type A uncertainty (Random error)

Standard uncertainties of type A can be obtained for steady-state measurements, by statistical analysis. During one measurement, 900 samples over 15 minutes are taken. The best estimate of a quantity  $x$  is determined by taking the arithmetic mean  $\bar{x}$  of  $n$  samples ( $x_i$ ), see equation (E.1).

$$\bar{x} = \frac{\sum_{i=1}^n x_i}{n} \quad (\text{E.1})$$

Furthermore, the uncertainty is characterised by its standard deviation, because all samples are normally distributed around the mean. The standard deviation can be calculated with equation (E.2), giving a 68% level of confidence. However, in this research a level of confidence of 95% is required [9], but this will be achieved by calculating the expanded combined uncertainty as mentioned in the introduction of this section. see equation (??).

$$u_{\text{random}} = \sigma_x = \left( \frac{\sum_{i=1}^n (x_i - \bar{x})^2}{n(n-1)} \right)^{0.5} \quad (\text{E.2})$$

With  $\sigma_x$  is the standard deviation of the mean of quantity  $x$ .

The random error can only be determined for quantities which are constant over time (steady-state), since an arithmetic mean and a standard deviation is used. However, for multi-pass experiments the process temperatures are not constant and show dynamic behaviour over time. According to ISO-9806, the random error for (quasi) dynamic measurements can be set to 0. Therefore, the random error for temperature measurements in the multi-pass experiments are neglected. For other quantities, such as flowrate and irradiance, the random error is determined with statistical analysis described above.

The random error of temperature measurements are in the order of magnitude of  $10^{-3}$ . Therefore, it is assumed to be acceptable to neglect the random error for the temperature measurements during multi-pass experiments.

### E.2 Type B uncertainty (Systematic error)

Standard uncertainties of type B can be obtained by using specified accuracies. According to ISO/IEC guide 98-3:2008 [33] it can be assumed that these specified accuracies are priori distributed with a rectangular shape, which means that the stated accuracy has symmetric bounds and there is an equal probability that a measurement point lies between these bounds. In general, this means that the standard uncertainty of type-B, which is specified by an accuracy, can be calculated by dividing the stated accuracy by  $\sqrt{3}$ . However, if the supplier explicitly specifies that the accuracy is based on another distribution, then the accuracy should be divided by another

factor. For convenience this factor is called the divisor, see equation E.3. Below an overview of different divisors is given:

- Divisor =  $\sqrt{3}$ , when a priori distribution with a rectangular shape is stated in the specifications (Standard).
- Divisor = 2, when the expanded combined uncertainty is stated in the specifications.
- Divisor =  $\sqrt{6}$ , when a priori distribution with a triangular shape is stated in the specifications.

$$u_{B,x} = \frac{\alpha_x}{\text{Divisor}} \quad (\text{E.3})$$

Where  $\alpha_x$  is the specified accuracy.

### E.3 Combined standard uncertainty of measured values

As explained in previous sections the total error consist of a random error and a systematic error. In section 3.7 the systematic errors of the measuring quantities flowrate, irradiance, temperatures and temperature difference are presented, which also includes random errors during calibration. However, during the measurements of the experiments also a random error occurs. Therefore, the random error during experiments is added to the systematic error by using equation (E.4). This is the general rule to combine errors.

$$u_{std} = \sqrt{\sum_{i=1}^n u_i^2} \quad (\text{E.4})$$

### E.4 Error propagation

Most quantities can not be directly measured and need to be calculated with other quantities. In this case, the corresponding error can be calculated by using the law of error propagation [26]. In this section only the cases of adding, subtracting, multiplication and division is explained. In the examples the standard combined uncertainty of quantity  $x$  ( $u_{std}$ ) is calculated, where  $x \pm u_{std}$  is a function of  $y \pm u_y$  and  $z \pm u_z$ . The law of error propagation is used for all derived quantities in this section.

For adding and subtracting ( $x = y + z$  or  $x = y - z$ ),  $u_x$  can be calculated with (E.5).

$$u_{std} = \sqrt{u_y^2 + u_z^2} \quad (\text{E.5})$$

For multiplication and division ( $x = yz$  or  $x = y/z$ ),  $u_x$  can be calculated with (E.6).

$$u_{std} = \sqrt{\left(\frac{\partial x}{\partial y} u_y\right)^2 + \left(\frac{\partial x}{\partial z} u_z\right)^2} \quad (\text{E.6})$$

### E.5 Expanded uncertainty

The expanded uncertainty is calculated from the standard combined uncertainty by multiplying it with a coverage factor,  $k$ . For a 95.5% confidence interval the coverage factor  $k$  equals 2.

$$u_{exp} = k \cdot u_{std} \quad (\text{E.7})$$



## E.6 Standard combined uncertainty of derived quantities

In this section the standard combined uncertainties of all derived quantities are presented, which are calculated by using equation (E.5) and (E.6).

### E.6.1 Fluid properties

No uncertainties of the fluid properties are specified in ISO 9806:2017 [1]. However, Van den Heuvel [15] reported an expanded uncertainty in  $c_p$  of  $\pm 1.60 J/(kgK)$  and  $\pm 0.25$ . Since he did not report an uncertainty for the density is assumed. The uncertainty of  $c_p$  is approximately 0.04% of the actual value; therefore, the same accuracy of 0.04% is used for the density, which result in an uncertainty of  $\pm 0.4 kg/m^3$ .

### E.6.2 Massflow

$$\dot{m} = \frac{\dot{V}\rho}{1000 \cdot 60} \quad (E.8)$$

With  $\dot{V}$  in L/min.

$$\begin{aligned} u_{\dot{m}} &= \sqrt{\left(\frac{\partial \dot{m}}{\partial \dot{V}} u_{\dot{V}}\right)^2 + \left(\frac{\partial \dot{m}}{\partial \rho} u_{\rho}\right)^2} \\ &= \sqrt{\left(\frac{\rho}{1000 \cdot 60} u_{\dot{V}}\right)^2 + \left(\frac{\dot{V}}{1000 \cdot 60} u_{\rho}\right)^2} \end{aligned} \quad (E.9)$$

### E.6.3 Aperture area

The uncertainty in the aperture area  $A_a$  is assumed to be  $\pm 0.005 m^2$ , since its area is reported with 2 decimals in the certificate in appendix F.

### E.6.4 Thermal efficiency collector

$$\begin{aligned} u_{\eta} &= \sqrt{\left(\frac{\partial \eta}{\partial \dot{m}} u_{\dot{m}}\right)^2 + \left(\frac{\partial \eta}{\partial c_p} u_{c_p}\right)^2 + \left(\frac{\partial \eta}{\partial \Delta T} u_{\Delta T}\right)^2 + \left(\frac{\partial \eta}{\partial G} u_G\right)^2 + \left(\frac{\partial \eta}{\partial A_a} u_{A_a}\right)^2} \\ &= \sqrt{\left(\frac{c_p \Delta T}{G A_a} u_{\dot{m}}\right)^2 + \left(\frac{\dot{m} \Delta T}{G A_a} u_{c_p}\right)^2 + \left(\frac{\dot{m} c_p}{G A_a} u_{\Delta T}\right)^2 + \left(-\frac{\dot{m} c_p \Delta T}{G^2 A_a} u_G\right)^2 + \left(-\frac{\dot{m} c_p \Delta T}{G A_a^2} u_{A_a}\right)^2} \end{aligned} \quad (E.10)$$

### E.6.5 Ambient temperature

$$T_a = \frac{T_{A1} + T_{A2} + T_{A3} + T_{A4}}{4} \quad (E.11)$$

$$\begin{aligned} u_{T_a} &= \sqrt{\left(\frac{\partial T_a}{\partial T_{A1}} u_{T_{A1}}\right)^2 + \left(\frac{\partial T_a}{\partial T_{A2}} u_{T_{A2}}\right)^2 + \left(\frac{\partial T_a}{\partial T_{A3}} u_{T_{A3}}\right)^2 + \left(\frac{\partial T_a}{\partial T_{A4}} u_{T_{A4}}\right)^2} \\ &= \sqrt{\left(\frac{1}{4} u_{T_{A1}}\right)^2 + \left(\frac{1}{4} u_{T_{A2}}\right)^2 + \left(\frac{1}{4} u_{T_{A3}}\right)^2 + \left(\frac{1}{4} u_{T_{A4}}\right)^2} \end{aligned} \quad (E.12)$$

### E.6.6 Mean temperature

$$T_m = \frac{T_{in} + T_{out}}{2} \quad (E.13)$$

$$\begin{aligned} u_{T_m} &= \sqrt{\left(\frac{\partial T_m}{\partial T_{in}} u_{T_{in}}\right)^2 + \left(\frac{\partial T_m}{\partial T_{out}} u_{T_{out}}\right)^2} \\ &= \sqrt{\left(\frac{1}{2} u_{T_{in}}\right)^2 + \left(\frac{1}{2} u_{T_{out}}\right)^2} \end{aligned} \quad (E.14)$$

### E.6.7 Reduced temperature

$$T_{red} = \frac{T_m - T_a}{G} = \frac{\Delta T_{m-a}}{G} \quad (E.15)$$

$$\begin{aligned} u_{T_{red}} &= \sqrt{\left(\frac{\partial T_{red}}{\partial \Delta T_{m-a}} u_{\Delta T_{m-a}}\right)^2 + \left(\frac{\partial T_{red}}{\partial G} u_G\right)^2} \\ &= \sqrt{\left(\frac{1}{G} u_{\Delta T_{m-a}}\right)^2 + \left(\frac{-\Delta T_{m-a}}{G^2} u_G\right)^2} \end{aligned} \quad (E.16)$$

### E.6.8 Optical efficiency

Since the optical efficiency consists of 3 parts, first the uncertainty of the parts are calculated separately and are then combined.

$$\eta_0 = \eta + a_1 T_{red} + a_2 G T_{red}^2 = \eta_{0,p1} + \eta_{0,p2} + \eta_{0,p3} \quad (E.17)$$

With  $\eta_{0,p1} = \eta$ ,  $\eta_{0,p2} = a_1 T_{red}$  and  $\eta_{0,p3} = a_2 G T_{red}^2$ .

$$\begin{aligned} u_{\eta_0} &= \sqrt{\eta^2 + \left(\frac{\partial \eta_{0,p2}}{\partial a_1} u_{a_1}\right)^2 + \left(\frac{\partial \eta_{0,p2}}{\partial T_{red}} u_{T_{red}}\right)^2 + \left(\frac{\partial \eta_{0,p3}}{\partial a_2} u_{a_2}\right)^2 + \left(\frac{\partial \eta_{0,p3}}{\partial G} u_G\right)^2 + \left(\frac{\partial \eta_{0,p3}}{\partial T_{red}} u_{T_{red}}\right)^2} \\ &= \sqrt{\eta^2 + (T_{red} u_{a_1})^2 + (a_1 u_{T_{red}})^2 + (G T_{red}^2 u_{a_2})^2 + (a_2 T_{red}^2 u_G)^2 + (2a_2 G T_{red} u_{T_{red}})^2} \end{aligned} \quad (E.18)$$

# Appendix F

## Solar Keymark Certificate



### CERTIFIKAT

Solar Keymark Certificate  
No. SP SC0175-15

#### Holder/Issued to

Company: TWL Technologie GmbH  
Address: Im Gewerbegebiet 8-12, 92271 Freihung, Germany

#### Product name and description

Vacuum tube thermal solar collectors for water heating. For technical information see Appendix (2 pages).

Models:	TWL HLK20, TWL HLK30
---------	----------------------

#### Certificate

The product mentioned above is found to comply with requirements in EN 12975-1:2006+A1:2010 and the Specific CEN Keymark Scheme Rules for Solar Thermal Products, and are based on test results according to ISO 9806:2013.

#### Marking

Products conforming to this certificate shall be marked in accordance with the requirements in the Specific CEN Keymark Scheme Rules for Solar Thermal Products. The marking shall, together with the Keymark logo, show the identification code of the empowered certification body (SP Technical Research Institute of Sweden, No. 012), also see CEN-CENELEC Internal Regulations Part 4 Certification, Annex A.

#### Validity

This certificate is valid until 2020-01-28 provided that the conditions in the Solar Keymark Rules are fulfilled and the standard or rules are not modified significantly. The validity of the certificate can be checked in the database, see Solar Keymark website <http://www.solarkeymark.org>

#### Miscellaneous

The manufacturer's factory production control procedures are under surveillance by the responsibility of SP. This is the first version of this certificate.

Borås, Sweden 2015-04-21

SP Technical Research Institute of Sweden  
Certification

  
Lennart Aronsson  
Product Certification Manager

  
Susanne Hansson  
Certification Officer



SP Technical Research Institute of Sweden

Postal address: SP, Box 857, SE-501 15 Borås, SWEDEN  
Phone / Fax: +4610 516 50 00 / +4633 13 55 02  
Reg number: 556494-6874  
E-mail / Internet: info@sp.se, www.sp.se

Empowered Certification Body No. 012: SP Certification, Sweden  
For more information of Solar Keymark visit: [www.solarkeymark.org](http://www.solarkeymark.org)  
This certificate may not be reproduced other than in full, except with the prior written approval by SP.

Certificate page 1 (1)

5P02115

Figure F.1: Solar Keymark certificate part 1



Annex to Solar Keymark Certificate



Page 1/2

Summary of ISO 9806 Test Results		Licence Number		SP SC0175-15							
		Issued		2015-04-21							
Company holding the	TWL Technologie GmbH			Country	Germany						
Brand (optional)	HLK20			Website	www.twl-technologie.de						
Street, street number	Im Gewerbegebiet 8-12			E-mail	vertrieb@twl-technologie.de						
Postal Code / City, province	D-92271	Freihung		Tel/Fax	+49 04351-75 17 00						
Collector Type (flat plate glazed/un-glazed; evacuate tubular)	Evacuated tubular collector										
Thermal / photo voltaic hybrid collector? (PVT collector)	No										
Integration in the roof possible? (manufacturers declaration)	No										
Collector name	Aperture area (Aa)	Gross length	Gross width	Gross height	Gross area (AG)	Power output per collector module					
						G = 1000 W/m <sup>2</sup>					
						Tm-Ta					
						0 K	10 K	30 K	50 K	70 K	
TWL HLK20	1.86	1 953	1 550	151.5	3.03	1 415	1 371	1 270	1 155	1 025	
TWL HLK30	2.78	1 953	2 300	151.5	4.49	2 116	2 049	1 899	1 727	1 532	
Performance test method		Glazed liquid heating collector - steady state - outdoor									
Performance parameters related to aperture		η0	a1	a2							
Units		-	W/(m <sup>2</sup> K)	W/(m <sup>2</sup> K <sup>2</sup> )							
Test results - Flow rate and fluid see note 1		0.761	2.299	0.010							
Bi-directional incidence angle modifiers?		Yes Kθ values are obligatory for 50°.									
Incidence angle modifiers Kθ(θT) transversal direction		Angle	10°	20°	30°	40°	50°	60°	70°	80°	90°
		Kθ(θT)	--	1.03	--	1.19	--	1.31	--	--	0.00
Incidence angle modifiers Kθ(θL) longitudinal direction		Angle	10°	20°	30°	40°	50°	60°	70°	80°	90°
		Kθ(θL)	--	--	--	--	0.90	--	--	--	0.00
Stagnation temperature - Weather conditions see note 2				Tstg		228.5 °C					
Effective thermal capacity				ceff = C/Ag		4.38 kJ/(m <sup>2</sup> K)					
Max. intended operation temperature - see note 3				Tmax,op		120 °C					
Max. operation pressure - see note 3				pmax,op		700 kPa					
Pressure drop table - for a collector family, the values shall be for the module with highest ΔP per m <sup>2</sup> aperture area											
Flow rate	kg/(s m <sup>2</sup> )	0.005	0.010	0.015	0.020	0.025	0.030				
Pressure drop, ΔP	Pa	663	1705	3263	5257	7699	10602				
Optional weather data		Location			Link						
Testing Laboratory		Intertek Testing Services Shenzhen Ltd. Guangzhou Branch									
Website		www.intertek.com									
Test report id. number		140605032GZU-001			Date of test report		2014-12-18				
During the test GDIF/GTOT was always between		0.11	and	0.22							
Comments of testing laboratory:											
Aperture area, referenced to above, is according to definition in ISO 9488:2008.											
Note 1	Flow rate	0.020	kg/(s m <sup>2</sup> )	Fluid	Water						
Note 2	Irradiance, G = 1000 W/m <sup>2</sup> ; Ambient temperature, Ta=30 °C										
Note 3	Given by manufacturer										
SP02115/OBL1018-14								Date: 4.06.2014-01-15			
Test lab: Intertek Testing Services Shenzhen Ltd. Guangzhou Branch Block E, No.7-2 Guang Dong Software Science Park, Caipin Road, Guangzhou Science City,GETDD, Guangzhou, China. Telephone: 86 20 82139688											

Figure F.2: Solar Keymark certificate part 2



Annex to Solar Keymark Certificate

Page 2/2

Annual collector output based on ISO 9806 Test Results, annex to Solar KEYMARK Certificate	Licence Number	SP SC0175-15
	Issued	2015-04-21

Annual collector output kWh/module														
Collector name	Location and collector temperature (Tm)													
	Athens			Davos			Stockholm			Würzburg				
	25°C	50°C	75°C	25°C	50°C	75°C	25°C	50°C	75°C	25°C	50°C	75°C		
TWL HLK20	2 468	2 010	1 561	2 007	1 593	1 208	1 466	1 124	829	1 581	1 213	882		
TWL HLK30	3 688	3 004	2 333	3 000	2 381	1 805	2 191	1 680	1 238	2 363	1 812	1 319		

Collector mounting: Fixed or tracking Fixed; slope = latitude - 15° (rounded to nearest 5°)

Overview of locations				
Location	Latitude *	Gtot kWh/m²	Ta °C	Collector orientation or tracking mode
Athens	38	1 765	18.5	South, 25°
Davos	47	1 714	3.2	South, 30°
Stockholm	59	1 166	7.5	South, 45°
Würzburg	50	1 244	9.0	South, 35°

Gtot	Annual total irradiation on collector plane	kWh/m²
Ta	Mean annual ambient air temperature	°C
Tm	Constant collector operating temperature (mean of in- and outlet temperatures)	°C

The calculation of the annual collector performance is performed with the official Solar Keymark spreadsheet tool ScenoCalc. The collector output is calculated hour by hour according to the efficiency parameters from the Keymark test using constant collector operating temperature (Tm). A detailed description of the calculations is available at <http://www.sp.se/en/index/services/solar/ScenoCalc/Sidor/default.aspx>.

Certification Body: <b>SP Technical Research Institute of Sweden</b> Box 857, 501 15 Borås, Sweden www.sp.se info@sp.se tel +4610 516 5000	Datasheet version:
	4.06, 2014-01-15
	ScenoCalc version:
	Ver. 4.06 (Jan, 2014)

Figure F.3: Solar Keymark certificate part 3

# Appendix G

## Heat Exchanger Performance

The heat exchanger performance check is based on the maximum thermal power that the collector can supply, which is approximately 1125 W (assuming a maximum irradiance 1400 W/m<sup>2</sup> with a maximum efficiency of 0.8). It is also assumed that the bottom coil does have to cool 8 times more than the top coil, which is a rough estimation. However, it is better to overestimate the required thermal power of the bottom coil, since this one needs to operate at the lowest temperature. The top coil only operates at temperatures higher than 30°C or 40°C and the chiller can supply a temperature of approximately 9°C, which means that there is a very high  $\Delta T$  available to cool if this is necessary. Therefore, the bottom coil is the most critical heat exchanger.

The entire calculation is based on the logarithmic mean temperature difference method and the UA value is based on the external surface area, see equation (G.2). The  $\Delta T_{ln}$  is based on the in- and outlet temperature of the heat exchanger and the average tank temperature, see equation (G.3). This method is commonly used in the heat exchanger industry to evaluate the performance of a heat exchanger, for example at VDL Klima. The results of this calculation program are presented in figure G.1 to G.4. The yellow fields are possible input fields and the blue fields are the final results of the last iteration.

First the heat balance will be calculated, with  $\dot{Q}_{req} = 1000 \text{ W/m}^2$  (8/9 times 1125 W/m<sup>2</sup>),  $\dot{m} = 0.17 \text{ kg/s}$  (=10 L/min) and  $T_{in} = 9^\circ\text{C}$ , resulting in an outlet temperature  $T_{out}$ , see equation (G.2). Then the  $\Delta T_{ln}$  can be calculated.

This program is able to calculate the thermal performance of the heat exchanger, which is an iterative process. Since the dimensions of the coil are given by the supplier it is only necessary to check if the coil reaches the required thermal power. It calculates the required surface area and compares this with the actual surface area. As a result, a design margin can be calculated, see equation (G.4). The design margin is a measure for the over capacity of the heat exchanger. If a design margin is higher than 0%, the performance of the coil is acceptable, while a lower design margin means that the coil is not suitable for the application. It can be concluded that with an inlet temperature of 9°C a design margin of 38.9% can be obtained, which means that the design of the coil is approved. The top coil can be operated with a temperature difference of 1°C and still has a design margin of 14.2%.

$$\dot{Q}_{req} = \dot{m}c_p(T_{out} - T_{in}) \quad (\text{G.1})$$

$$\dot{Q} = U_o A_o \Delta T_{ln} \quad (\text{G.2})$$

$$\Delta T_{ln} = \frac{(T_{in} - T_{av,tank}) - (T_{out} - T_{av,tank})}{\ln\left(\frac{T_{in} - T_{av,tank}}{T_{out} - T_{av,tank}}\right)} \quad (\text{G.3})$$

With  $T_{av,tank}$  is the average temperature of the low temperature zone  $T_{low}$ . For the calculation of  $T_{av,tank}$  and example will be given with  $T_{low} = 10^\circ\text{C}$  and  $T_{high} = 45^\circ\text{C}$ . At the start of an experiment  $T_{av,tank}$  is equal to  $T_{low} = 10^\circ\text{C}$  and it is assumed that the position of thermocline is exactly at the top of the helically coil. After 1 hot water injection the thermocline lowers slightly and the coil can

start to cool this part. This actually has influence on  $T_{av,tank}$ . At some point an equilibrium starts to form, where the position and the thickness of the thermocline remains constant. It is estimated that this equilibrium starts to form around 5 cycles, which is a rough estimation. However, if an extra design margin of 25% is taken into account, this method is assumed to be valid. Table G.1 shows an overview of the calculation of  $T_{av,tank}$ . In this table the height of the hot water column is equivalent to 20L of injected hot water.

Table G.1: Calculation of the average temperature of the low temperature zone of the tank.

Parameter	Value	Unit
Internal diameter tank	0,545	m
Injection volume per cycle	4	L
Number of cycles	5	-
Total injected volume	20	L
Height helically coil	0,47	m
Height hot water column	0,09	m
Height cold water column	0,38	m
Temperature hot water column	45	°C
Temperature cold water column	10	°C
Average temperature tank	16,4	°C

$$Design\ Margin = \left( \frac{Q_{act}}{Q_{req}} - 1 \right) * 100 \quad (G.4)$$

The overall heat transfer coefficient  $U_o$  is calculated by using equation (G.5), with  $\alpha_i$  the convective heat transfer coefficient in the tube side and  $\alpha_o$  the convective heat transfer coefficient at the tank side.  $\alpha_i$  is calculated with standard Nusselt relations for helically coil heat exchangers from the VDI Heat Atlas [7]. All equations that are used can be found in figure G.1 to G.4. After each calculated variable it is mentioned which equation from the VDI heat atlas is used.  $\alpha_o$  is calculated with natural convection correlations for helically coils. Two different correlations of Fernández-Seara J. et al [4] and Devanahalli G. Prabhanjan et al. [2] are used and the one with the lowest Nusselt number is used for safety purposes. Both correlations are optimised for domestic hot water storage tanks, see equation G.6 and G.7.

$$\frac{1}{U_o} = \frac{1}{\alpha_i} \frac{A_o}{A_m} + \frac{\delta}{\lambda} \frac{A_o}{A_m} + \frac{1}{\alpha_o} \quad (G.5)$$

With  $\delta$  is the tube thickness and  $\lambda$  is the conduction coefficient.

Nusselt number correlation according to Fernández-Seara J. et al:

$$Nu = 0.0749 Ra^{0.3421} \quad (G.6)$$

Nusselt number correlation according to Devanahalli G. Prabhanjan et al:

$$Nu = 0.818 Ra^{0.2633} \quad (G.7)$$

With Ra is the Rayleigh number.

The convective heat transfer coefficient  $\alpha_o$  is then calculated by equation (G.8).

$$\alpha_o = Nu \frac{\lambda}{H} \tag{G.8}$$

With H is the height of the coil.

	Flow		Thigh		
	Iteratie 1	Iteratie 7	Iteratie 1	Iteratie 7	
<b>In- &amp; Output</b>					
<b>Heat Balance (Q=m cp dT)</b>					
Water temperature tank	16,4	16,4	45	45	°C
Delta T (Twater tank - Tav tube)	6,7	6,7	1,0	1,0	°C
Thermal power delivery solar circuit	1000	1000	125	125	W
Flow rate	10	10	10	10	L/min
Volume flow	0,00017	0,00017	0,00017	0,00017	m3/s
Mass flow	0,17	0,17	0,17	0,17	kg/s
Delta T (Tout - Tin)	1,4	1,4	0,2	0,2	°C
Tmean	9,7	9,7	44,0	44,0	°C
Tin	9,0	9,0	43,9	43,9	°C
Tout	10,4	10,4	44,1	44,1	°C
LMTD	6,7	6,7	1,0	1,0	°C
<b>Geometry Coil</b>					
Projected diameter of a winding (Dc)	0,4	0,4	0,4	0,4	m (VDI 2 G3)
The average diameter of a spiral (Ds)	0,4002	0,4002	0,4002	0,4002	m (VDI 1 G3)
Average diameter of curvature (D)	0,4004	0,4004	0,4004	0,4004	m (VDI 3 G3)
Diameter tube outside (do)	0,03	0,03	0,0295	0,0295	m
Wall thickness (t)	0,002	0,002	0,002	0,002	m
Diameter tube inside (di)	0,026	0,026	0,0255	0,0255	m
Number of turns	11	11	8	8	-
Pitch (h)	0,040	0,040	0,040	0,040	m
Thermal conductivity tube (C-steel)	50	50	50	50	W/mK
Total height coil	0,4700	0,4700	0,3495	0,3495	m
Lenght Tube	13,98	13,98	10,21	10,21	m
<b>Output</b>					
Design margin (Overdesign)	48,6	38,9	17,0	14,2	%

Figure G.1: Results of the heat exchanger calculation program for the first and the last iteration for the helically coil for  $T_{low}$  and  $T_{high}$  (Part 1).



**Calculations General**

Velocity	0,31	0,31	0,33	0,33	m/s
Reynolds	6039	6163	13668	13690	-(VDI Bc3)
Reynolds critical	8079	8079	8029	8029	-(VDI 4 G3)
Prandtl	9,7	9,5	4,0	4,0	-(VDI Bc3)
Prandtl @Wall	9,7	9,2	4,0	3,9	-(VDI Bc3)
<b>Nusselt Coil</b>					
Coeff m	0,67	0,67	0,67	0,67	-(VDI 12 G3)
Nu_Lam (Re<Re_crit)	66,3	66,9	83,5	83,5	-(VDI 12 G3)
Friction factor	0,044	0,043	0,037	0,037	-(VDI 14 G3)
Nu_Turb (Re>22000)	73,7	74,4	108,6	108,7	-(VDI 13 G3)
Nu_Lam (@Re=Re_crit)	79,8	79,5	59,6	59,5	-(VDI 15 G3)
Friction factor (@Re=22000)	3,36E-02	0,03342	0,033534	0,033539	-(VDI 15 G3)
Nu_Turb (@Re=22000)	2,29E+02	226,7028	163,3892	163,2799	-(VDI 15 G3)
Gamma	1,146493	1,137649	0,596343	0,594754	-(VDI 16 G3)
Nu_Trans	5,80E+01	59,22715	101,4678	101,5657	-(VDI 15 G3)
Nu	66,3	66,9	101,5	101,6	-
<b>Nusselt Straight Pipe (To compare)</b>					
Num,q,2,2300	6,76	6,71	5,53	5,53	-
Num,q,3,2300	4,07	4,04	3,50	3,50	-
Num,L,2300	7,27	7,23	6,27	6,27	-
Num,T,10^4	99,82	99,00	71,09	71,03	-
Nusselt	52,22	53,26	101,96	102,08	-
Nusseltcorrected	53,78	51	194	102,00	-
ξ	0,04	0,04	0,03	0,03	-(VDI 27 Ga5)
Nusselt (Re>=10000)	65,94	66,50	91,33	91,38	-(VDI 26 Ga5)
Nusselt corrected	67,91	64,16	173,84	91,32	-(VDI 41 Ga8)
Nusselt Straight Tube	53,78	51,39	173,84	91,32	-
<b>Internal Heat Transfer Coefficient Tube</b>					
Heat transfer coefficient (α)	1492,7	1509,0	2531,8	2534,6	W/(m²K) (VDI Ga5)
<b>Pressure drop straight pipe</b>					
ξ smooth Re <10^5 (Blasius)	0,04	0,04	0,03	0,03	[-]
ΔP	950	946	618	618	Pa
<b>External Heat Transfer Coefficient (Natural convection)</b>					
Thermal Expansion Coefficient (β)	1,7E-04	1,7E-04	4,5E-04	4,5E-04	1/°C
Thermal diffusivity (α)	1,4E-07	1,4E-07	1,5E-07	1,5E-07	m²/s
Film temperature @do	12,8	13,5	44,5	44,5	°C
Rayleigh with do height as char. Length (Ra_do)	1,9E+06	1,6E+06	1,2E+06	1,1E+06	-
Rayleigh with tube length as char. Length (Ra_L)	2,0E+14	1,6E+14	5,0E+13	4,7E+13	-
Rayleigh with coil height as char. Length (Ra_H)	7,5E+09	6,1E+09	2,0E+09	1,9E+09	-

Figure G.2: Results of the heat exchanger calculation program for the first and the last iteration for the helically coil for  $T_{low}$  and  $T_{high}$  (Part 2).

APPENDIX G. HEAT EXCHANGER PERFORMANCE

<b>External HTC by Fernández-Seara J</b>					
Nusselt (Nu <sub>do</sub> )	22,6	21,4	19,9	19,6	-(4,67*10 <sup>6</sup> <=Ra<=3,54*10 <sup>7</sup> )
Nusselt (Nu <sub>l</sub> )	9921,9	9395,9	6910,9	6787,6	-(1,97*10 <sup>14</sup> <=Ra<=1,49*10 <sup>15</sup> )
Nusselt (Nu <sub>H</sub> )	325,7	308,4	230,1	226,0	-(5,31*10 <sup>9</sup> <=Ra<=4,02*10 <sup>10</sup> )
External heat transfer coefficient (α <sub>do</sub> )	446,5	423,7	430,8	423,1	W/(m <sup>2</sup> K)
External heat transfer coefficient (α <sub>l</sub> )	419,9	398,5	431,2	423,6	W/(m <sup>2</sup> K)
External heat transfer coefficient (α <sub>H</sub> )	409,9	389,0	419,4	411,9	W/(m <sup>2</sup> K)
<b>External HTC by Prabhanjan</b>					
Nusselt (Nu <sub>l</sub> )	4648,8	4282,1	2694,1	2621,9	-(5*10 <sup>14</sup> <=Ra<=3*10 <sup>15</sup> )
Nusselt (Nu <sub>H</sub> )	178,9	166,7	113,9	111,3	-(9*10 <sup>9</sup> <=Ra<=4*10 <sup>11</sup> )
External heat transfer coefficient (α <sub>l</sub> )	196,7	181,6	168,1	163,6	W/(m <sup>2</sup> K)
External heat transfer coefficient (α <sub>H</sub> )	225,2	210,3	207,7	202,9	W/(m <sup>2</sup> K)
External heat transfer coefficient (α)	196,7	181,6	168,1	163,6	W/(m <sup>2</sup> K)
<b>Performance HEX, Length known</b>					
LMTD	6,6544	6,6544	0,9973	0,9973	°C
A <sub>in</sub>	1,142	1,142	0,818	0,818	m <sup>2</sup>
A <sub>m</sub>	1,230	1,230	0,882	0,882	m <sup>2</sup>
A <sub>out</sub>	1,318	1,318	0,946	0,946	m <sup>2</sup>
R1 <sub>con_tube</sub>	5,9E-04	5,8E-04	4,8E-04	4,8E-04	K/W
R2 <sub>tube</sub>	3,3E-05	3,3E-05	4,5E-05	4,5E-05	K/W
R3 <sub>conv_tank</sub>	3,9E-03	4,2E-03	6,3E-03	6,5E-03	K/W
R <sub>tot</sub>	4,5E-03	4,8E-03	6,8E-03	7,0E-03	K/W
UA	223,4	208,7	146,7	143,1	W/K
U <sub>internal</sub>	195,6	182,7	179,4	175,0	W/(m <sup>2</sup> K)
U <sub>mean</sub>	181,6	169,7	166,4	162,3	W/(m <sup>2</sup> K)
U <sub>out</sub>	169,5	158,4	155,1	151,3	W/(m <sup>2</sup> K)
Q = U A ΔT <sub>ln</sub> = U <sub>out</sub> A <sub>out</sub> ΔT <sub>ln</sub>	1486,4	1388,6	146,3	142,7	W
A <sub>out_required</sub>	0,89	0,95	0,81	0,83	m <sup>2</sup>
Area ratio (=Q ratio)	1,49	1,39	1,17	1,14	-
Q ratio	1,49	1,39	1,17	1,14	W/(m <sup>2</sup> K)
Design margin	48,6	38,9	17,0	14,2	%
<b>Wall Temperatures</b>					
Wall temperature internal	9,1049	10,526	44,0094	44,0688	°C
Wall temperature external	9,1049	10,571	44,0094	44,0753	°C
Wall temperature external (check)	10,6660	10,597	44,0801	44,0781	
Check wall temperature	-1,56110	-0,026	-0,07065	-0,00274	

Figure G.3: Results of the heat exchanger calculation program for the first and the last iteration for the helically coil for  $T_{low}$  and  $T_{high}$  (Part 3).

APPENDIX G. HEAT EXCHANGER PERFORMANCE

---

**Water Properties (Source VDI Heat Atlas)**

Density water @ Tmean	999,6	999,6	990,6	990,6	kg/m <sup>3</sup>
Thermal capacity water @ Tmean	4197,3	4197,3	4178,2	4178,2	J/kgK
Conduction coefficient @ Tmean	0,6	0,6	0,6	0,6	W/mK
Dynamic viscosity @ Tmean	1,35E-03	1,32E-03	6,03E-04	6,02E-04	kg/ms (T<=112,1°C)
Kinematic viscosity @ Tmean	1,35E-06	1,32E-06	6,09E-07	6,08E-07	m <sup>2</sup> /s
Density water @ Twall	999,6	999,5	990,6	990,6	kg/m <sup>3</sup>
Thermal capacity water @ Twall	4198,1	4196,3	4178,2	4178,2	J/kgK
Conduction coefficient @ Twall	0,6	0,6	0,6	0,6	W/mK
Dynamic viscosity @ Twall	1,35E-03	1,29E-03	6,02E-04	6,01E-04	kg/ms (T<=112,1°C)
Kinematic viscosity @ Twall	1,35E-06	1,29E-06	6,08E-07	6,07E-07	m <sup>2</sup> /s
Density water @ Tfilm_do	999,2	999,1	990,4	990,4	kg/m <sup>3</sup>
Thermal capacity water @ Tfilm_do	4193,8	4193,0	4178,2	4178,3	J/kgK
Conduction coefficient @ Tfilm_do	0,6	0,6	0,6	0,6	W/mK
Dynamic viscosity @ Tfilm_do	1,22E-03	1,19E-03	5,97E-04	5,96E-04	kg/ms (T<=112,1°C)
Kinematic viscosity @ Tfilm_do	1,22E-06	1,19E-06	6,03E-07	6,02E-07	m <sup>2</sup> /s

Figure G.4: Results of the heat exchanger calculation program for the first and the last iteration for the helically coil for  $T_{low}$  and  $T_{high}$  (Part 4).

# Appendix H

## Mechanical Construction Details

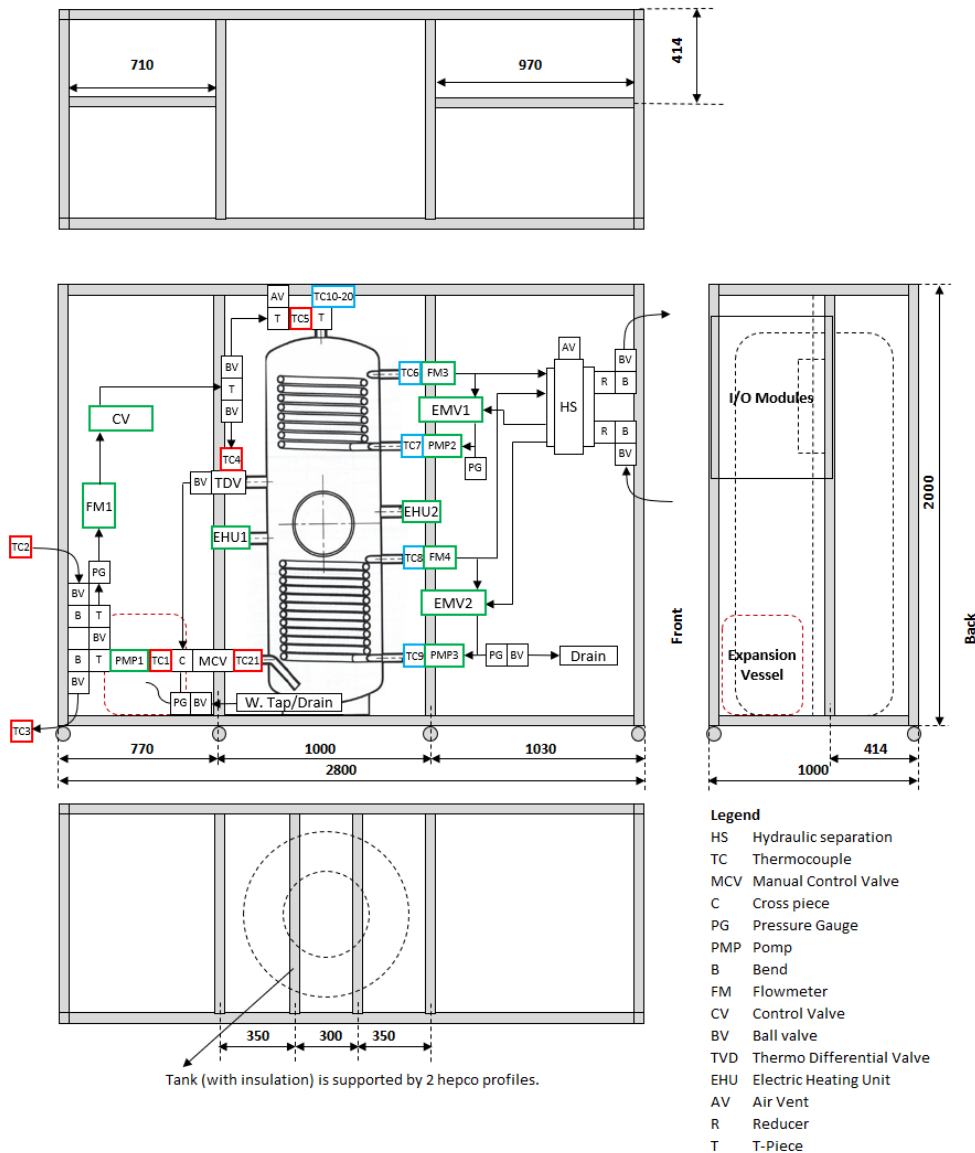


Figure H.1: Total layout of the set-up including the dimensions. All components are illustrated on scale.

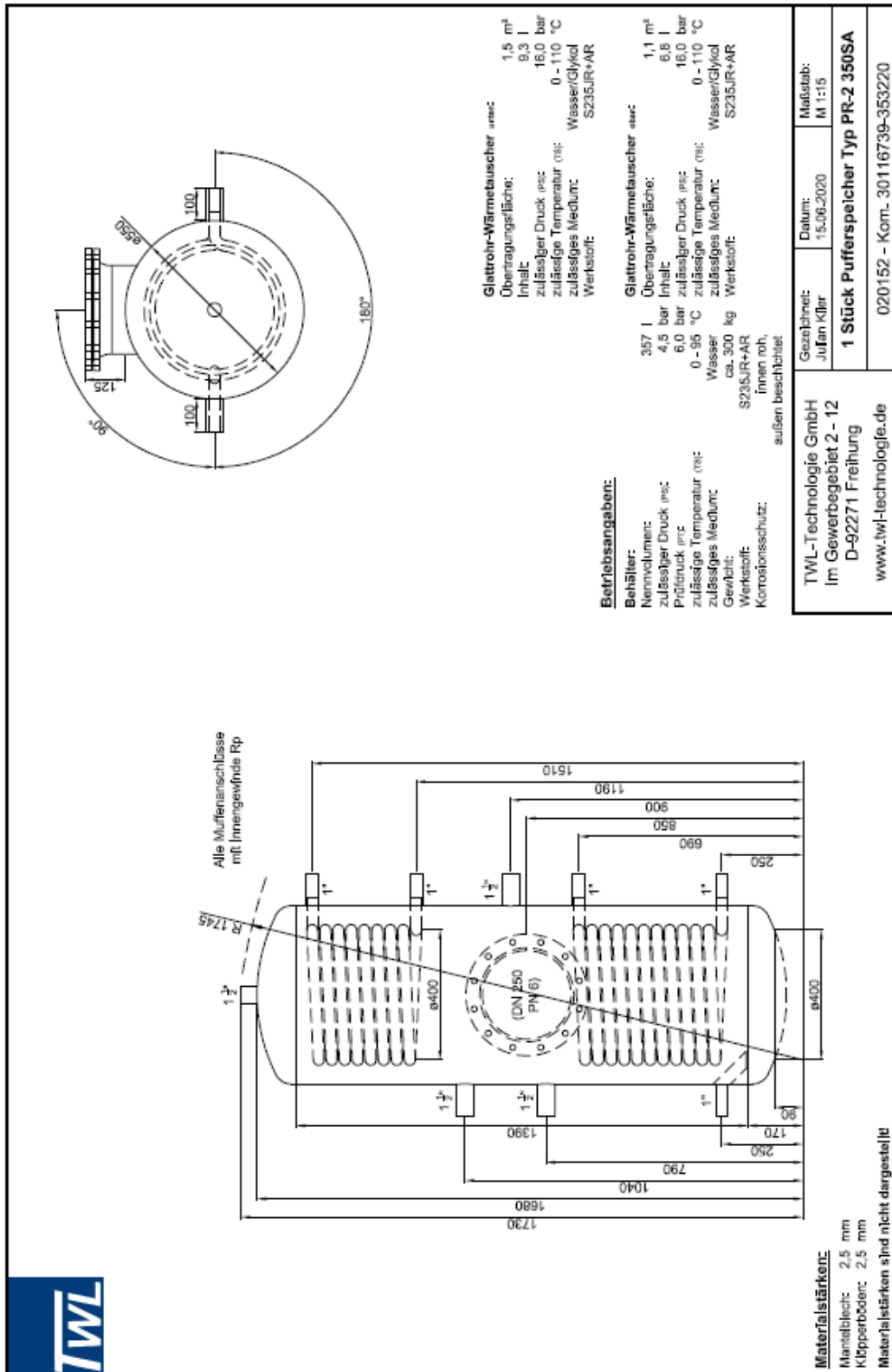


Figure H.2: Technical drawing of the storage tank, made by the supplier TWL.

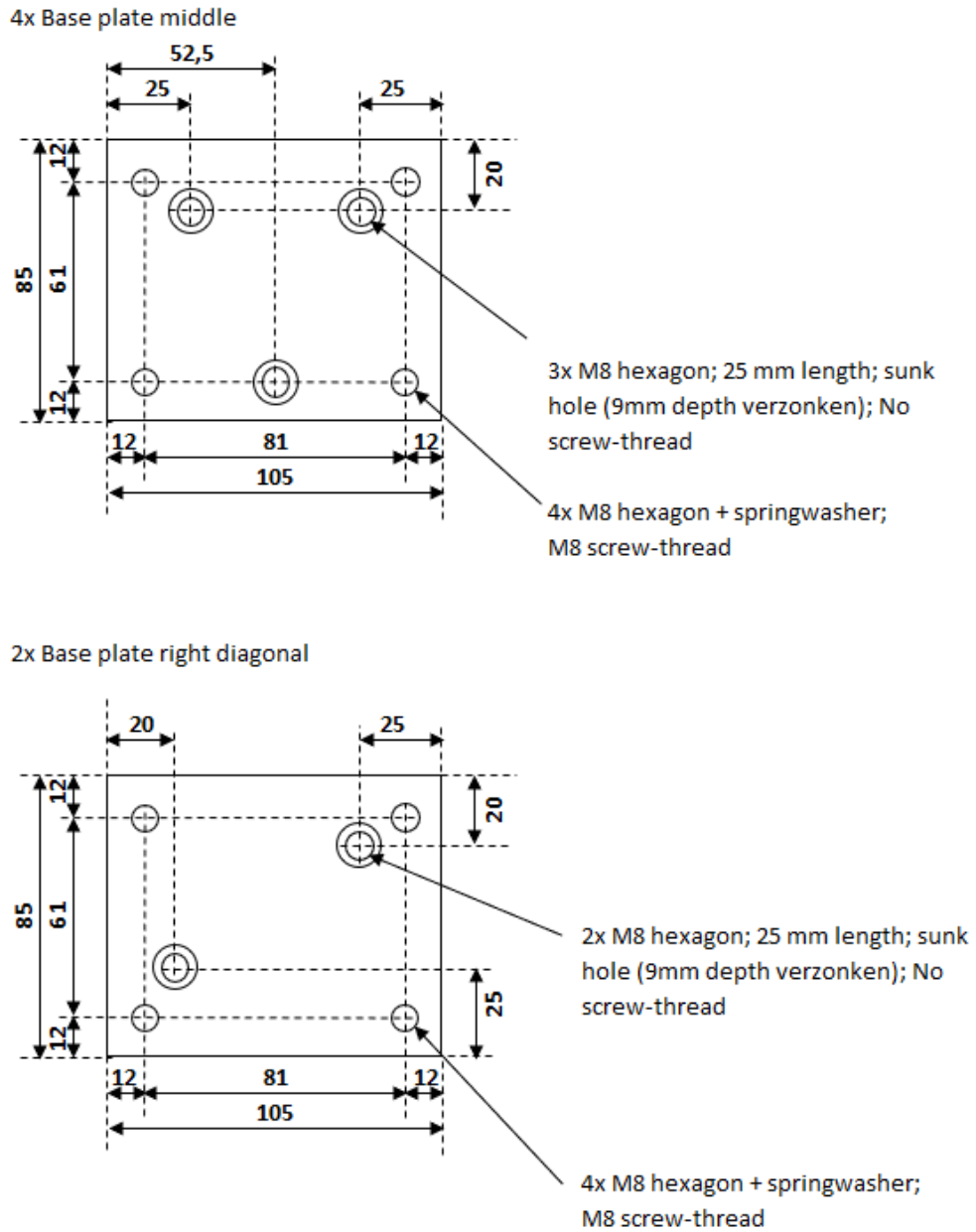


Figure H.3: Dimensions of the base Plates for mounting the wheels (middle and right diagonal).

2x Base plate left diagonal

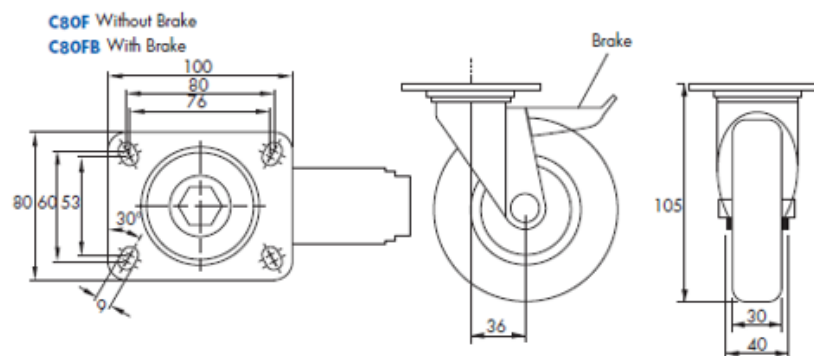
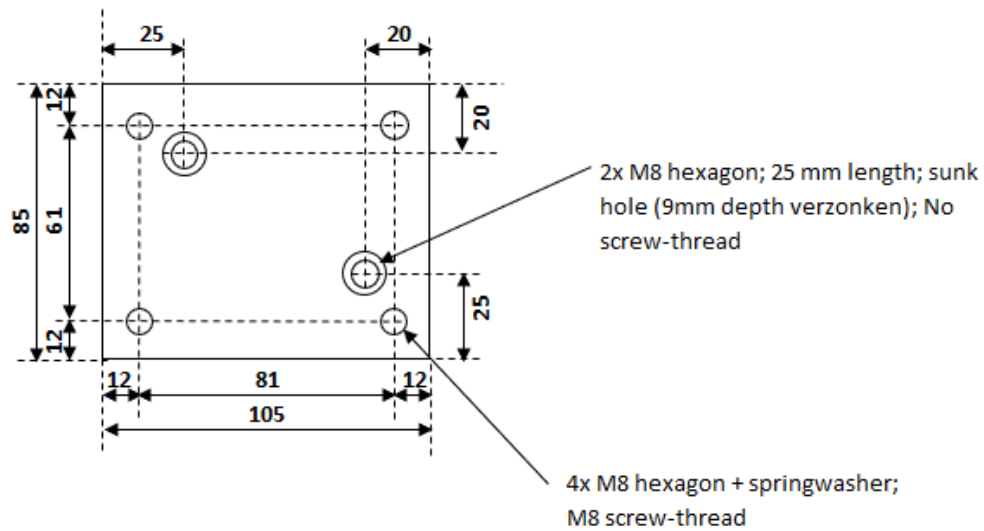


Figure H.4: Dimensions of the base plates for mounting the wheels (left diagonal) and dimensions of the wheels.

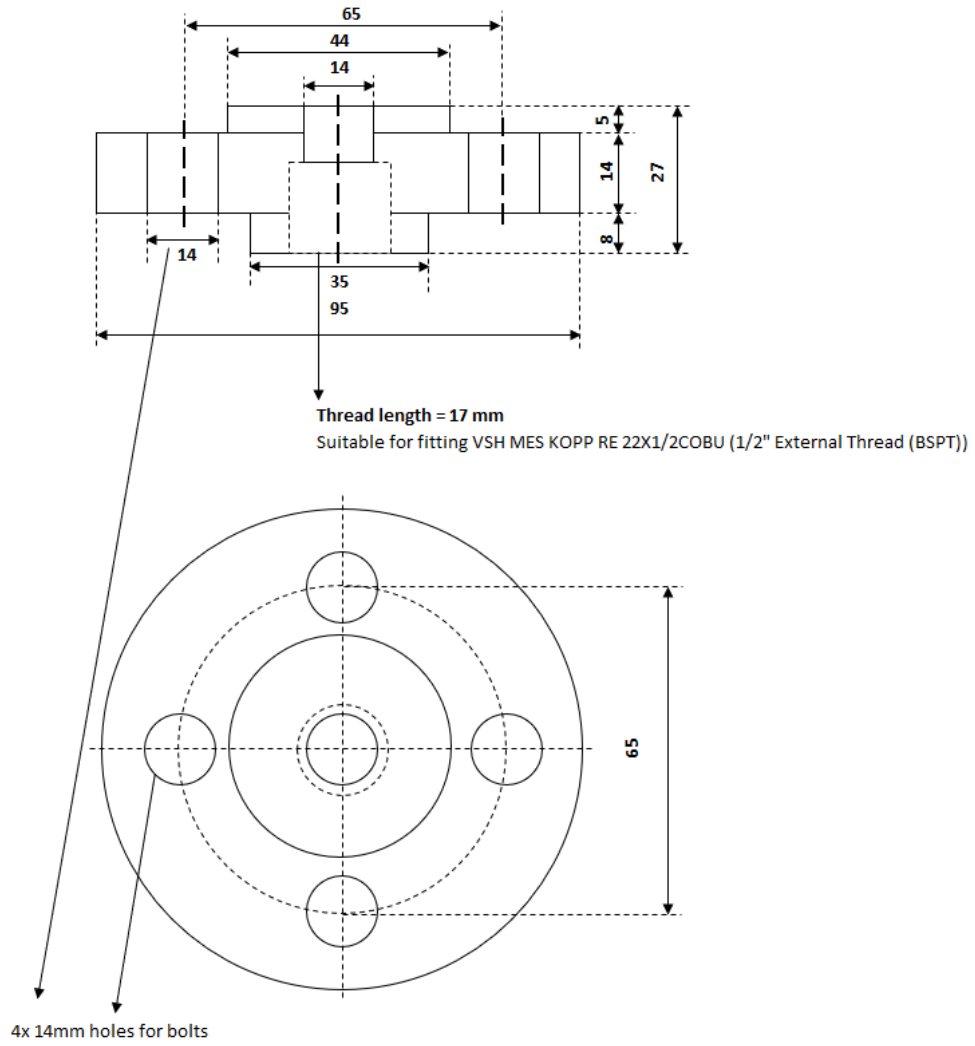


Figure H.5: Dimensions of the flanges of the flowmeters (4 in total).



Technical Data

	30 x 90	40 x 40SL	40 x 40L	40 x 40
Max. Length	5600mm	5600mm	5600mm	5600mm
Mass	2.19kg/m	1.3kg/m	1.4kg/m	1.7kg/m
Moment of Inertia (cm <sup>4</sup> )	I <sub>xx</sub> 64.1 I <sub>yy</sub> 8.5	I <sub>xx</sub> 7.8 I <sub>yy</sub> 7.8	I <sub>xx</sub> 8.4 I <sub>yy</sub> 8.4	I <sub>xx</sub> 10.2 I <sub>yy</sub> 10.2
Section Modulus (cm <sup>3</sup> )	W <sub>xx</sub> 14.2 W <sub>yy</sub> 5.7	W <sub>xx</sub> 3.9 W <sub>yy</sub> 3.9	W <sub>xx</sub> 4.2 W <sub>yy</sub> 4.2	W <sub>xx</sub> 5.1 W <sub>yy</sub> 5.1

Aanduiding materiaal: AlMgSi0.5F25  
 Materiaalnummer: A16063-T5  
 Minimum treksterkte: 250N/mm<sup>2</sup>  
 0.2% limietspanning: 160N/mm<sup>2</sup>  
 Rekbaarheid A<sub>g</sub>: 10%  
 Rekbaarheid A<sub>0.2</sub>: 8%  
 Elasticiteitsmodulus: 70 000N/mm<sup>2</sup>  
 Brinell-hardheid: 75 HB  
 Thermische uitzettingscoëfficiënt: (-50...+20°C) = 21.8 x 10<sup>-6</sup> 1/K  
 (+20...+100°C) = 23.8 x 10<sup>-6</sup> 1/K  
 Dwarscontractie: ν = 0.34  
 Anodiseerproces: EG/VI blank  
 Laagdikte: 10 µm  
 Hardheid: 300 HV

Opmerking: Deze doorbuigingsberekeningen kunnen worden vervangen door het hoofdstuk 'Kiezen van het juiste MCS profiel voor uw toepassing' (bladzijden 56 en 57) te raadplegen, hoewel grafisch verkregen resultaten nauwkeuriger zijn.

Doorbuiging van profiel onder statische puntbelasting:

$$d_1 = \frac{F \times L^3}{3E \times I \times 10^9}$$

$$d_2 = \frac{F \times L^3}{48E \times I \times 10^9}$$

$$d_3 = \frac{F \times L^3}{192E \times I \times 10^9}$$

1 Vrijdragend (een uiteinde vast)  
 2 Eenvoudig ondersteund  
 3 Beide uiteinden vast

Doorbuiging van profiel onder het eigen gewicht (zie de diagrammen boven):

$$d_1 = \frac{9.81 \times P \times L^4}{8E \times I \times 10^9}$$

$$d_2 = \frac{5 \times 9.81 \times P \times L^4}{384E \times I \times 10^9}$$

$$d_3 = \frac{9.81 \times P \times L^4}{384E \times I \times 10^9}$$

E = 70 000N/mm<sup>2</sup> (elasticiteitsmodulus)  
 L = Niet-ondersteunde lengte (mm)  
 F = Belasting (N)  
 I = Traagheidsmoment (cm<sup>4</sup>)  
 D = Doorbuiging van profiel (mm)  
 W = Profielmodulus (cm<sup>3</sup>)  
 P = Massa van profiel (kg/m)

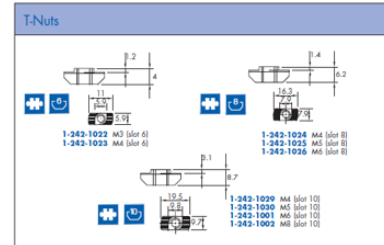
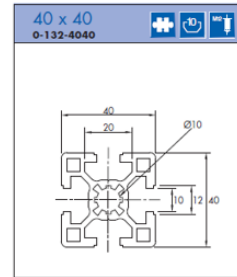
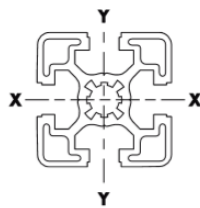
Maximum toegestane buigspanning (zie de diagrammen boven):

$$\sigma_{max} < 200N/mm^2$$

$$\sigma_1 = \frac{F \times L}{W \times 10^3}$$

$$\sigma_2 = \frac{F \times L}{4W \times 10^3}$$

$$\sigma_3 = \frac{F \times L}{8W \times 10^3}$$



Beugel 36x36		1800	60	10
--------------	--	------	----	----

Figure H.6: Technical data of the 40x40 Hepco profiles.

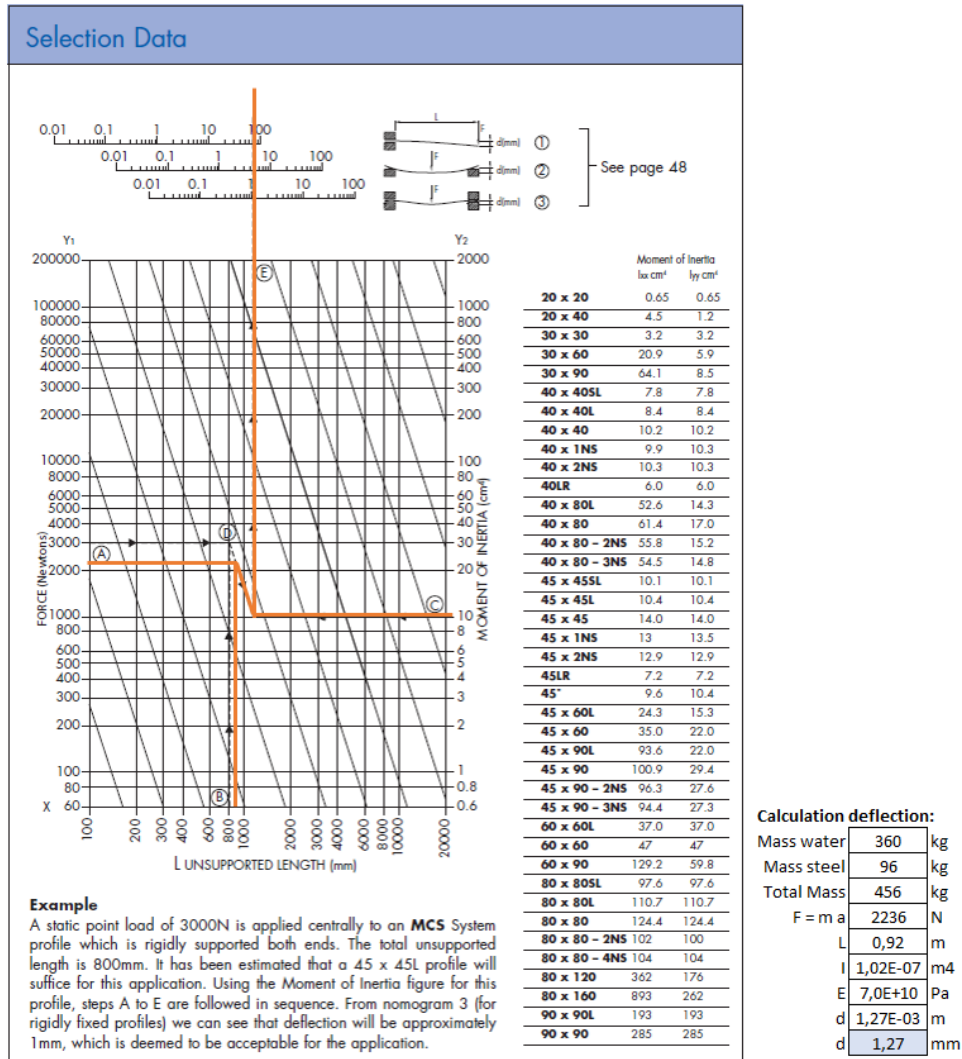


Figure H.7: Manual determination and theoretical calculation of the deflection of the critical beams.

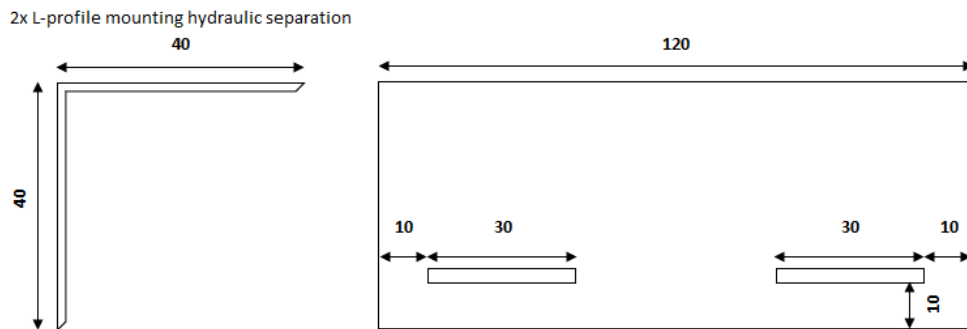


Figure H.8

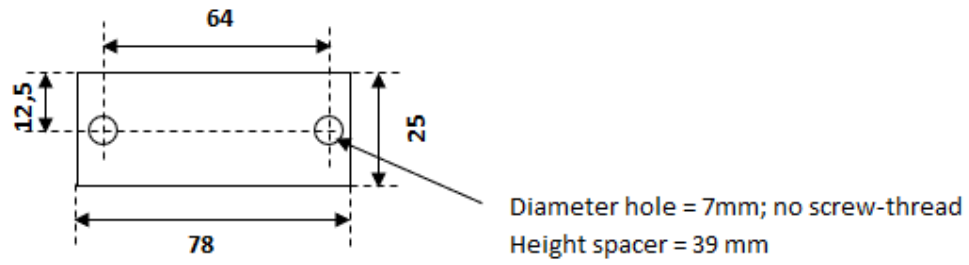


Figure H.9: Dimensions of the spacers between the wall and the piping.

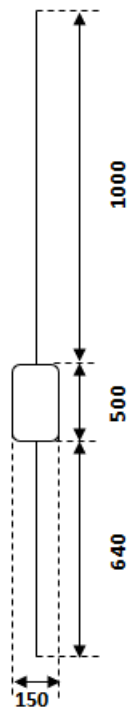


Figure H.10: Thermocouple construction inside the tank.

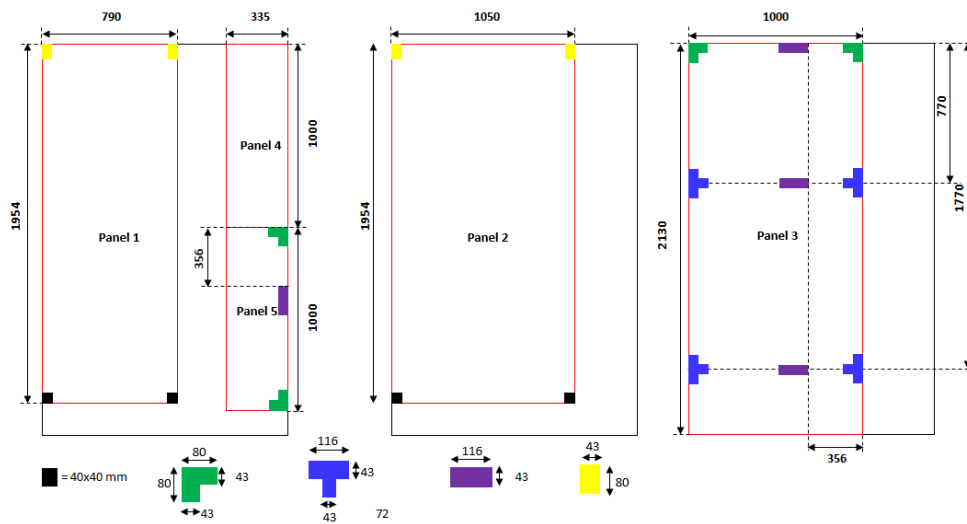


Figure H.11: The dimensions of Trespa panels used in the set-up are coloured in red. In total 3 panels were delivered by the supplier

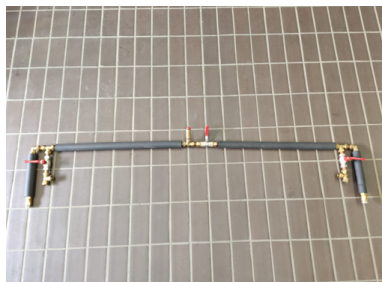
# Appendix I

## Additions to original set-up

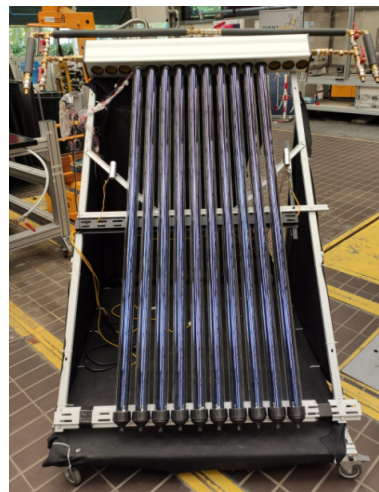
### I.1 Extra by-pass line to determine thermal effective capacity

An extra by-pass line is added to the original set-up, see figure I.1.

With this addition it might be possible to determine the effective thermal capacity in different operation conditions, in the future. This extra by-pass is currently dismantled to reduce disturbances from outside, but this can simply be added in the future. It is also not presented in the piping and instrument diagram in figure 3.5. With this by-pass it is possible to use determine the thermal effective capacity according to the procedure of equation (A.2). The measurement procedure can be briefly described as followed: First the entire tank should be heated to a certain condition  $t_{m2}$ . Then a constant inlet temperature of steady state condition 1  $t_{m1}$  can be supplied to the collector by the old set-up and when steady- state is achieved, 2 ball valves can be switched in order to supply  $t_{m2}$  to the collector.



(a) By-pass line dismantled



(b) By-pass line mounted

Figure I.1: Extra by-pass line to determine thermal effective capacity

## I.2 Connection with original set-up

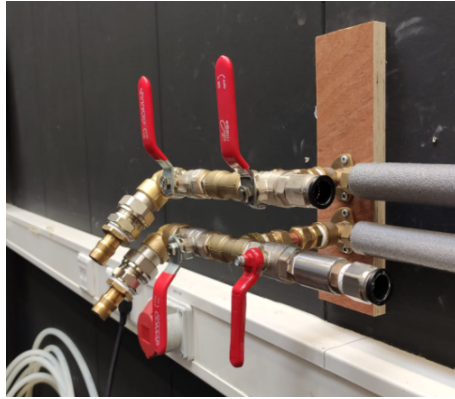


Figure I.2: Connection to original set-up

# Appendix J

## Instrumentation specifications

### J.1 Specifications OPTIFLUX 4100 - DN6

Table J.1: Specifications of the flowmeter: OPTIFLUX 4100 - DN6. These specifications are generated by software of KROHNE. The selection is performed at standard conditions: fluid temperature of 20°C at 3 bar.

<b>Flowrate</b>	<b>Velocity</b>	<b>Accuracy</b>	<b>Pressure drop</b>	<b>Reynolds</b>
[L/min]	[m/s]	[%]	[mbar]	[-]
0,0017	0,00	100,4	0,0	6
0,1263	0,07	1,74	0,1	446,6
0,2508	0,15	1,08	0,2	887,2
0,3	0,18	0,97	0,2	1061
0,3754	0,22	0,85	0,3	1328
0,5	0,29	0,74	0,4	1768
0,75	0,44	0,63	1	2653
1	0,59	0,57	2	3537
2	1,18	0,48	6	7074
4	2,36	0,44	20	14147
7	4,13	0,42	54	24757
10	5,90	0,42	100	35368
13	7,66	0,41	159	45978
16	9,43	0,41	228	56588
19	11,20	0,41	308	67199
20,35	12,00	0,41	348	72000

## J.2 Calibration Certificate Pyranometer



**OTT**  
HydroMet

**CALIBRATION CERTIFICATE**

Meteorology Division of OTT HydroMet



**KIPP & ZONEN**

---

Kipp & Zonen B.V. | Delftechpark 36 | 2628 XH Delft | The Netherlands | +31 15 2755 210 | info@kippzonen.com | www.kippzonen.com

<b>CERTIFICATE NUMBER</b>	019328976349
<b>PYRANOMETER MODEL</b>	CM 11
<b>SERIAL NUMBER</b>	976349
<b>SENSITIVITY</b>	4.99 $\mu\text{V}/\text{W}/\text{m}^2$ at normal incidence on horizontal pyranometer
<b>IMPEDANCE</b>	1093 $\Omega$
<b>REFERENCE PYRANOMETER</b>	Kipp & Zonen CM 11 sn 913550 active from 01 August 2018
<b>CALIBRATION DATE</b>	04 July 2019
<b>CLASSIFICATION</b>	ISO 9060, Class A (Sec. Standard)*

**Calibration procedure**  
 The indoor calibration procedure is based on a side-by-side comparison with a reference pyranometer under an artificial sun fed by an AC voltage stabiliser. It embodies a 150 W Metal-Halide high-pressure gas discharge lamp. Behind the lamp is a reflector with a diameter of 16.2 cm. The reflector is 1 m above the pyranometers producing a vertical beam. The reference and test pyranometers are mounted horizontally on a table, which can rotate. The irradiance at the pyranometers is approximately 500  $\text{W}/\text{m}^2$ . During the calibration procedure the reference and test pyranometer are interchanged to correct for any non-homogeneity of the beam. Temperature of calibration:  $22 \pm 2$   $^{\circ}\text{C}$ .

**Hierarchy of traceability**  
 The reference pyranometer was compared with the sun and sky radiation as source under clear sky conditions using the "alternating sun-and-shade method" ISO 9846 paragraph 5. The measurements were performed in Tabernas, Spain (latitude: 37.094°, longitude: -2.3547°, altitude: 503m above sea level). Dates of measurements: 8, 10-12 June 2018.  
 The receiver surface was pointed directly at the sun using a solar tracker. During the comparisons, the instrument received tilted global radiation intensities from 760 to 1194 with a mean of 1035  $\text{W}/\text{m}^2$  and tilted diffuse radiation intensities from 101 to 200 with a mean of 135  $\text{W}/\text{m}^2$ . The ambient temperature ranged from  $-22.8$  to  $+29.7$  with a mean of  $+27.3$   $^{\circ}\text{C}$ .  
 The direct radiation on the reference pyranometer as obtained with the alternating-sun-shade method was compared to the DNI measured by the absolute cavity pyrhemliometer PMO6 SN 103. The PMO6 is calibrated against the World Standard Group (WSG), maintained at the WRC Davos every international Pyrhemliometer Comparison (IPC). The PMO6 participates every IPC since 2005 and it participates in the yearly NPC hosted by NREL in Golden, Colorado to verify its stability. WRR factor of PMO6: 0.99789 (from the last IPC, IPC-2015).  
 This calibration proved that the reference pyranometer has been stable and that the original sensitivity  $4.66 \pm 0.06$   $\mu\text{V}/\text{W}/\text{m}^2$  is valid and will be applied (see PMOD calibration details). Observed sensitivity differences between the consecutive years are well within the calibration uncertainty.

**PMOD calibration details:** The reference pyranometer was compared with the sun and sky radiation as source under mainly clear sky conditions using the "continuous sun-and-shade method". The pyranometer was installed horizontally. During the comparisons, the global radiation ranged from 673 to 1033 with a mean of 898  $\text{W}/\text{m}^2$ . The solar zenith angle varied from 24.6 to 49.6 with a mean of 32.6 degrees. The ambient temperature ranged from  $+18.6$  to  $+24.9$  with a mean of  $+21.9$   $^{\circ}\text{C}$ . The sensitivity calculation is based on 531 individual measurements. The readings of the WSG are referred to the World Radiometric Reference (WRR). The estimated uncertainty of the WRR relative to SI is  $\pm 0.3\%$ . The obtained sensitivity value and its expanded uncertainty (95% level of confidence) are valid for similar conditions and are  $4.66 \pm 0.06$   $\mu\text{V}/\text{W}/\text{m}^2$ . The measurements were performed in Davos (latitude: 46.8143°, longitude: -9.8458°, altitude: 1558m above sea level). Dates of measurements: 10, 12, 15, 20, 21 July 2015.  
 Global radiation data were calculated from the direct solar radiation as measured with the absolute cavity pyrhemliometer PMO2 (member of the WSG, WRR-Factor: 0.998623, based on the last IPC-2010) and from the diffuse radiation as measured with a continuous disk shaded pyranometer Kipp & Zonen CM22 SN 020059 (ventilated with heated air).

**Justification of total instrument calibration uncertainty**  
 The combined uncertainty of the result of the calibration is the positive "root sum square" of two uncertainties.  
 1. The expanded uncertainty due to random effects and instrumental errors during the calibration of the reference CM 11 is  $\pm 0.06/4.66 = \pm 1.29\%$ . (See traceability text).  
 2. Based on experience, the expanded uncertainty of the transfer procedure (calibration by comparison) is estimated to be  $\pm 0.5\%$ .  
 The estimated combined expanded uncertainty is the positive "root sum square" of these two uncertainties:  $\sqrt{(1.29\% + 0.5\%)^2} = \pm 1.38\%$ .

**Notice**  
 The calibration certificate supplied with the instrument is valid at the date of first use. Even though the calibration certificate is dated relative to manufacture, or recalibration, the instrument does not undergo any sensitivity changes when kept in the original packing. From the moment the instrument is taken from its packaging and exposed to irradiance the sensitivity may deviate with time. See the 'non-stability' value (% change in sensitivity per year) given in the radiometer specifications.  
 \* From October 2018 the classification conforms to ISO 9060:2018. Instruments issued before that date conform to ISO 9060:1990.

Delft, The Netherlands, 04 July 2019



J. Mes  
(in charge of calibration facility)



V. Tromp  
(in charge of test)

Kipp & Zonen B.V.  
Trade name: OTT HydroMet  
Company registered in Delft

Trade register no.: 27239004  
VAT no.: NL0055.74.857.B.01  
Member of HMEI

EUR payments  
Deutsche Bank AG  
IBAN: NL70 DEUT 0265 2482 48  
BIC: DFUT33HAN

USD payments only  
Deutsche Bank AG  
IBAN: DE60100701000162416200  
BIC: DFUTDE33HAN

Figure J.1: Calibration certificate of the pyranometer



### J.3 Pump Curve

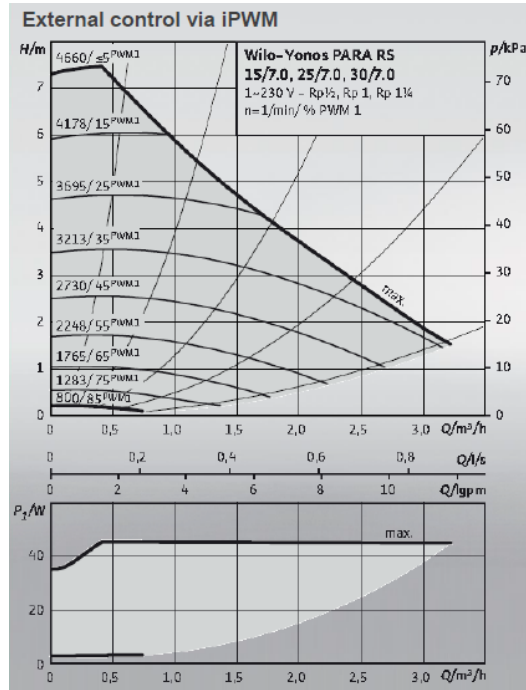


Figure J.2: Pump curve Wilo Yonos PARA ST15/7 PWM2

# Appendix K

## Difficulties experimental set-up

### K.1 Thermal efficiency vs. reduced temperature Multi-pass mode (Not Correct)

Figure K.1 shows the thermal efficiency vs. reduced temperature curve with 2 L/min, PV800,  $\Delta T_t = 35^\circ\text{C}$  and  $T_{low}$  of  $10^\circ\text{C}$ ,  $20^\circ\text{C}$ ,  $30^\circ\text{C}$  and  $40^\circ\text{C}$  respectively. However, during these measurements it turned out that 3 condensers were slid down out of the manifold, which means that these 3 condensers had minimum heat transfer to the manifold. This also explains why the measured efficiencies were considerably lower than expected.

After this was observed the condensers are placed in the manifold again, but now teflon tape is used in order to prevent that the condensor slides down into the evacuated tube. It is assumed that the teflon tape causes enough resistance to hold the condensor at its place. Figure K.2 shows how this is realized.

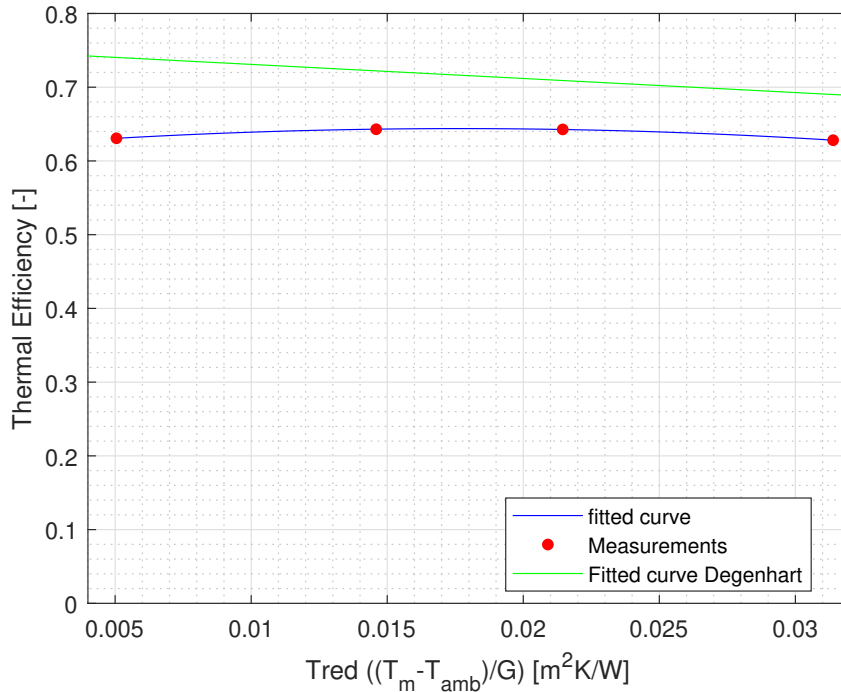


Figure K.1: Thermal efficiency vs. reduced temperature with 2 L/min, PV800,  $\Delta T_t = 35^\circ\text{C}$  and  $T_{low}$  of  $10^\circ\text{C}$ ,  $20^\circ\text{C}$ ,  $30^\circ\text{C}$  and  $40^\circ\text{C}$  respectively.



Figure K.2: Solution to prevent that the condenser slides down into the evacuated tube: teflon tape around cork.

It is highly recommended to use a tube stopper in the future, see figure K.3.

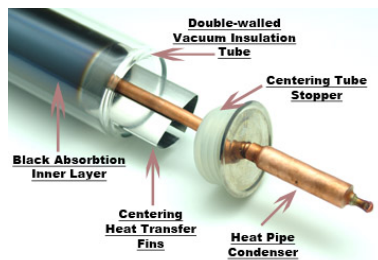


Figure K.3: Example of a tube stopper.

## K.2 End of lifetime lamps solar simulator

The solar simulator is operating for more than 8000 hours after this research. The lifetime of the lamps are approximately 8000 hours, and during this research 2 of them broke down, see appendix K.4 for the position of those lamps. Initially, it was assumed that this had minimum to zero effect on the thermal efficiency of the collector, because these lamps are not placed in the region of the solar collector.

The company Eternal Sun is already approached to do some maintenance and to calibrate the solar simulator on short term.

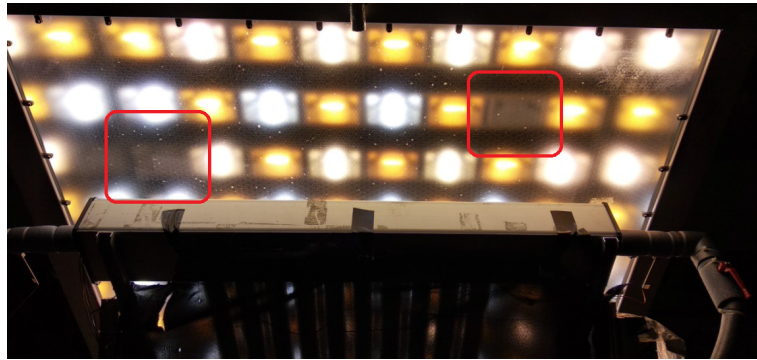


Figure K.4: Position of two lamps that broke down during this research

# Appendix L

## Data Acquisition with LabVIEW

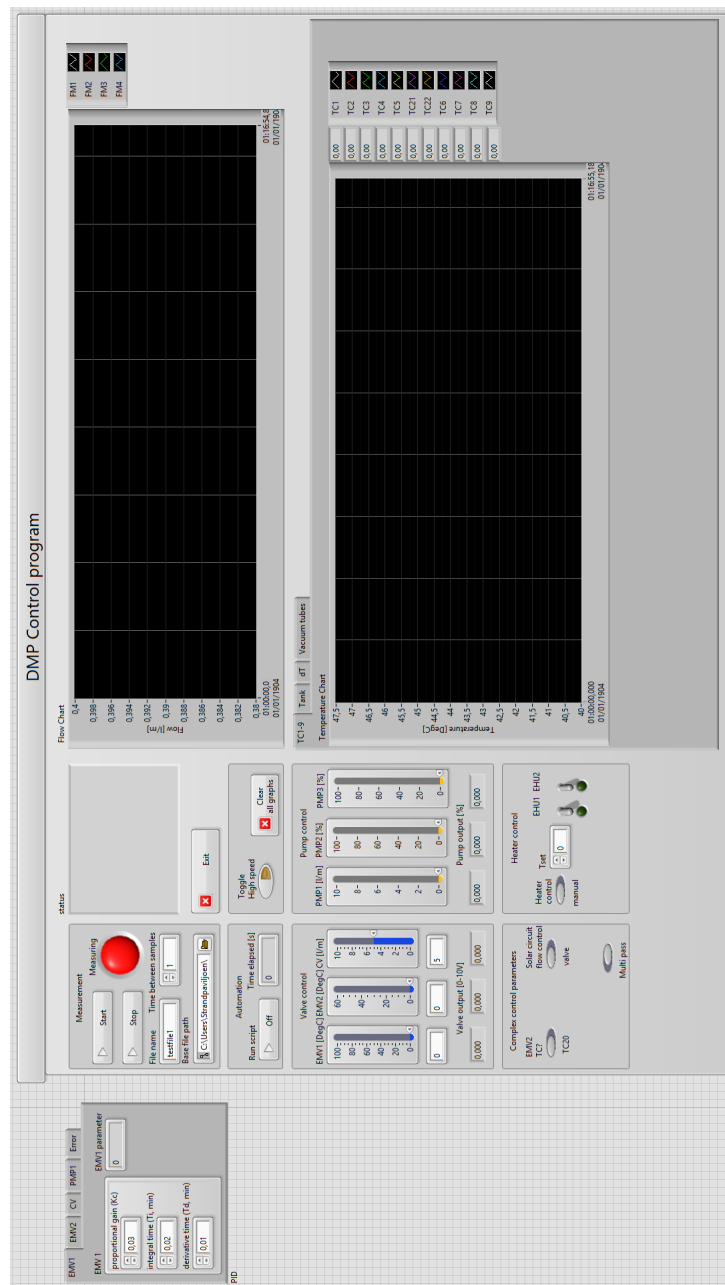


Figure L.1: Layout LabVIEW, data acquisition program. Process parameters can be monitored, controlled and logged. On the North-West side PID parameters can be set, in the middle all process parameters can be set and on the right hand side all process parameters can be monitored.

# Appendix M

## Bill of Materials

Component	Type	Bestelnummer / Art. Nr.	Stuks	Excl. BTW	Incl. 21% BTW	Tot. Prijs Excl. BTW	Tot. Prijs Incl. 21% BTW	Leverancier
Plaatmateriaal	Trespa platen 9m2		1	€ 459,13	€ 555,55	€ 459,13	€ 555,55	BMN
Vortex flow meter	Liquid view based 0,5-10 L/min: LVB-06-A (analog: 4-20mA)	LVB-06-A	1	€ 210,00	€ 254,10	€ 210,00	€ 254,10	Bronkhorst
Vortex flow meter	Liquid view based 2-40 L/min: LVB-10-A (analog: 4-20mA)	LVB-10-A	1	€ 210,00	€ 254,10	€ 210,00	€ 254,10	Bronkhorst
Pump	Wilo Yonos PARA ST15/7 PWM2	nvt	3	€ -	€ -	€ -	€ -	Conico
TDV	Thermo differential valve	nvt	1	€ -	€ -	€ -	€ -	Conico
Pakkingring pomp, rubber ring			10	€ 0	€ -	€ -	€ -	Conico
Schroefbus voor flowmeters	Schroefbus ontzinkingsbestendig (DZR) messing JG22 x 1/2	EF102214TL-AS	4	€ 11,25	€ 13,61	€ 45,00	€ 54,45	Easy-Fitt
Stalen staaf TC's	3 meter		1	€ 20,00	€ 24,20	€ 20,00	€ 24,20	EPC
Bevestigingsplaten voor wielen			8					EPC
EPC inschatting			1	€ 150,00	€ 181,50	€ 150,00	€ 181,50	EPC
Push koppeling	Rechte inschroefkoppeling met O-ring G 1/2" x 16	PC16-G04	2	€ 5,18	€ 6,27	€ 10,36	€ 12,54	FHT Perslucht
Knie push koppeling	Knie inschroefkoppeling met O-ring G 1/2" x 16	PL16-G04	1	€ 6,12	€ 7,41	€ 6,12	€ 7,41	FHT Perslucht
Verzonken boutjes voor plaat aan profiel			50					Grijpvoorraad Tue
Bouten en moeren connector aan plaat			120					Grijpvoorraad Tue
Bouten en moeren flens			32					Grijpvoorraad Tue
Boutenjes wielen aan plaat			60					Grijpvoorraad Tue
Bevestigingen CV leiding aan plaat	Buisklemmen - Lichte Bouwvorm DIN 3015 T1 22; FHT Perslucht	GR_322_LAPV	30					Grijpvoorraad Tue
4 flenzen voor flowmeter			4					Grijp Tue: EPC
Hepco profielen	Aluminium Profiel 40x40 (6x4m)		1	€ 471,12	€ 570,06	€ 471,12	€ 570,06	Hepco
Vracht hepc			1	€ 201,90	€ 244,30	€ 201,90	€ 244,30	Hepco
Hepco profielen	Aluminium Profiel 40x40 (6x4m)		1	€ -	€ -	€ -	€ -	Hepco
Hoeksteunen	MCS Beugel 36 X 36, 10 st.	1-242-3636-10	8	€ -	€ -	€ -	€ -	Hepco
Eind kap	MCS Eindkap 40 X 40, 10 st.	1-243-4041-10	1	€ -	€ -	€ -	€ -	Hepco
Flensmoer	MCS Flensmoer M8x12, 10 st.	1-242-1101-10	16	€ -	€ -	€ -	€ -	Hepco
T-bout	MCS T-bout M8x25L, 10 st.	1-242-1009-10	16	€ -	€ -	€ -	€ -	Hepco
T-moer voor platen en wielen	MCS T-moer M5 Slot 10, 10 st.	1-242-1030-10	5	€ -	€ -	€ -	€ -	Hepco
Wielen	MCS Wiel met rem	C80FB	8	€ -	€ -	€ -	€ -	Hepco
Flowmeter	OPTIFLUX4000	Zie quotation	2	€ 1.533,70	€ 1.855,78	€ 3.067,40	€ 3.711,55	KROHNE
Signal converter flowmeter	IFC 100		2	€ 669,20	€ 809,73	€ 1.338,40	€ 1.619,46	KROHNE
Digital out module for pump	Ni 9472 (DSUB-25)	779004-01	1	€ 117,00	€ 141,57	€ 117,00	€ 141,57	NI
DAQ TC Module (Utilizing TC)	Ni-9212: with 0,39 accuracy and With screw terminal	782975-01	1	€ 995,00	€ 1.203,95	€ 995,00	€ 1.203,95	NI
Ni 9214 Terminal block			1	€ 360,00	€ 435,60	€ 360,00	€ 435,60	NI
DIN Rail bevestiging voor qDAQ	Ni 9912 DIN Rail Mount Kit for 4-slotRIO-910x/911x/906x/90	779019-01	1	€ 35,00	€ 42,35	€ 35,00	€ 42,35	NI
Pijnpipen voor TC's vat	Pijnpipen 60mm	DPN11260RVS	1	€ 10,28	€ 12,44	€ 10,28	€ 12,44	Pneuparts
Pijnpipen voor TC's vat reserve	Pijnpipen 80mm	DPN11280RVS	1	€ 11,68	€ 14,13	€ 11,68	€ 14,13	Pneuparts
	Siemens, SITOP PSU100S DIN Rail Power Supply, 24V	776-7729	1	€ 137,70	€ 166,62	€ 137,70	€ 166,62	RS Components B.V.
	6 Pole Panel Mount Switch Disconnecter	103-8424	1	€ 54,21	€ 65,59	€ 54,21	€ 65,59	RS Components B.V.
	ABB 4 Pole Type AC Residual Current Circuit Breaker	537-7412	1	€ 86,14	€ 104,23	€ 86,14	€ 104,23	RS Components B.V.
	Kopp GREEN ELECTRIC MCB Mini Circuit Breaker	259-8313	2	€ 14,29	€ 17,29	€ 28,58	€ 34,58	RS Components B.V.
	Wago 221 Terminal Block Connector, 5 Way/Pole (zak van 1	883-7557	1	€ 8,22	€ 9,95	€ 8,22	€ 9,95	RS Components B.V.
	Phoenix Contact, ST 2.5-PE Series (Zak van 5)	388-4609	4	€ 11,50	€ 13,92	€ 46,00	€ 55,66	RS Components B.V.
	Altech Din Rail Top Hat, Slotted, 1m	899-0917	2	€ 2,99	€ 3,62	€ 5,98	€ 7,24	RS Components B.V.
	RS PRO Steel Wall Box	775-5823	1	€ 99,60	€ 120,52	€ 99,60	€ 120,52	RS Components B.V.
	chalflex CF211 data cable (rol 25m)	185-4838	1	€ 57,80	€ 69,94	€ 57,80	€ 69,94	RS Components B.V.
	Shield connection terminal block SK8	290-1208	10	€ 3,59	€ 4,34	€ 35,90	€ 43,44	RS Components B.V.
	Wago, Busbar, 2002 Series (1m)	758-1852	1	€ 9,42	€ 11,40	€ 9,42	€ 11,40	RS Components B.V.
	2 Core CY Control Cable 0.25 mm², 100m	445-1648	1	€ 78,95	€ 95,53	€ 78,95	€ 95,53	RS Components B.V.
	RS PRO Black No 3:1, Heat Shrink Tubing 6mm	700-4535	1	€ 16,45	€ 19,90	€ 16,45	€ 19,90	RS Components B.V.
	Amphenol Socapex C 091 A Series, 8 Pole Din Plug Plug	486-173	1	€ 10,43	€ 12,62	€ 10,43	€ 12,62	RS Components B.V.
	Amphenol Socapex C 091 A Series, 8 Pole Din Socket Socket	486-195	1	€ 9,09	€ 11,00	€ 9,09	€ 11,00	RS Components B.V.

Figure M.1: Bill of materials (Part 1)

APPENDIX M. BILL OF MATERIALS

Thermokoppels spiralen, type T	Type T, Ø 3,0 x 150mm lang; 2m kabel	Zie quotation	4	€ 27,20	€ 32,91	€ 108,80	€ 131,65	TC-direct
Thermokoppels verjongde tip, type T	Type T, special: Ø3,0 met 0,5mm tip; potseal, klasse 1, gea	Zie quotation	6	€ 63,50	€ 76,84	€ 381,00	€ 461,01	TC-direct
Thermokoppels, type T	Type TØ 3,0 ; lengte 0,5m; 2m kabel	Zie quotation	2	€ 31,40	€ 37,99	€ 62,80	€ 75,99	TC-direct
Thermokoppels, type T	Type TØ 3,0 ; lengte 1m; 2m kabel	Zie quotation	4	€ 29,80	€ 36,06	€ 119,20	€ 144,23	TC-direct
Thermokoppels, type T	Type TØ 3,0 ; lengte 1,5m; 2m kabel	Zie quotation	3	€ 34,80	€ 42,11	€ 104,40	€ 126,32	TC-direct
Thermokoppels, type T	Type TØ 3,0 ; lengte 2m; 2m kabel	Zie quotation	3	€ 36,50	€ 44,17	€ 109,50	€ 132,50	TC-direct
Knel verbinding met draad	3,0mm x 1/2" BSPT messing; 2m kabel	Zie quotation	10	€ 6,10	€ 7,38	€ 61,00	€ 73,81	TC-direct
Verzendkosten TC direct		Zie quotation				€ 15,00		TC-direct
Kabels thermokoppels			1	€ 60,00	€ 72,60	€ 60,00	€ 72,60	TC-Direct
Miniatuur connector TC			1	€ 30,00	€ 36,30	€ 30,00	€ 36,30	TC-Direct
Spectite TC Doorvoer (12 kanaals)			1	€ 163,00	€ 197,23	€ 163,00	€ 197,23	TC-Direct
bezorgkosten 2x			2	€ 15,00	€ 18,15	€ 30,00	€ 36,30	TC-Direct
Knel T-stuk met BSPT draad, TC	VSH MES T- 22X1/2X22 KXNB1 L	1121557	10	€ 8,03	€ 9,72	€ 80,33	€ 97,20	Technische Unie
Auto Ontluchter	SPIR SPIROVENT 22 MM RV2 C	4859864	1	€ 81,14	€ 98,18	€ 81,14	€ 98,18	Technische Unie
Expansievat	FLAM EXP VAT FLEXCON 35/1	1800101	1	€ 79,07	€ 95,67	€ 79,07	€ 95,67	Technische Unie
Watermeterkoppeling	RAM WATMTRKP 2DLG DN15 3/4X15	1960341	1	€ 3,75	€ 4,54	€ 3,75	€ 4,54	Technische Unie
Ball valve	CIMB KOGELKRAAN KNEEL 22MM	6736706	10	€ 12,26	€ 14,83	€ 122,60	€ 148,35	Technische Unie
Lucht-/vuilafscheider	FLAM VENT CLEAN SMART 22MM	4886222	1	€ 107,81	€ 130,45	€ 107,81	€ 130,45	Technische Unie
Drukmeter	EURO MANOMETER 63MM 1/4 ACHTER	855312	2	€ 8,45	€ 10,22	€ 16,90	€ 20,45	Technische Unie
Verloop Nippel Drukmeter	NEFT VERLOPPNG 1/2X1/4 ZW 341	6926083	2	€ 1,23	€ 1,49	€ 2,46	€ 2,98	Technische Unie
Manual control valve	TA STRREGELAFSL-V&A 1/2 STAD	5114566	1	€ 67,25	€ 81,37	€ 67,25	€ 81,37	Technische Unie
Electronic mixing valve	Siemens MXG461815-0-6	8911082	1	€ 644,76	€ 780,16	€ 644,76	€ 780,16	Technische Unie
Electronic mixing valve	Siemens MXG461815-1-5	8911089	1	€ 645,17	€ 780,66	€ 645,17	€ 780,66	Technische Unie
Control Valve	Siemens MXG461815-3	8911096	1	€ 643,14	€ 778,20	€ 643,14	€ 778,20	Technische Unie
Leiding 22mm	HME TECTUBE MED 22X1 LGS 1 7150639 - (totaal 12 meter no	4820817	3	€ 41,64	€ 50,38	€ 124,92	€ 151,15	Technische Unie
Isolatie leiding 22mm	ARST ARMAFLEX HT 10/22 LG2	6534176	7	€ 7,97	€ 9,64	€ 55,79	€ 67,51	Technische Unie
T-stukken	VSH MES T- 22X22X2 3KXN	1121219	14	€ 9,44	€ 11,42	€ 132,16	€ 159,91	Technische Unie
Hydraulic separation	Remeha DUO Open cv verdeler	7712227	1	€ 211,02	€ 255,33	€ 211,02	€ 255,33	Technische Unie
Bochtstukken	Bonfix knel knie messing 22x22 mm	1120740	10	€ 7,31	€ 8,85	€ 73,12	€ 88,48	Technische Unie
T-stuk groot	VIEG BRONS T-STUK 1 1/2" BIN	2558922	1	€ 22,85	€ 27,65	€ 22,85	€ 27,65	Technische Unie
Nippel vat	VSH DUBBELE NIPPEL 1 1/2" (BSPP)	789503	1	€ 14,08	€ 17,04	€ 14,08	€ 17,04	Technische Unie
Verloop hydraulische scheiding	SPRI RSOX VERL BIDR 2X1	7582590	2	€ -	€ -	€ -	€ -	Technische Unie
Draad naar knel fitting	VSH MES KOPP RE 22X1 COBU (BSPT, R) (5x vat; 6x hydr. Sep.;	1120302	17	€ -	€ -	€ -	€ -	Technische Unie
Dop hydr. Scheid.	VSH PLUG 1/2"	8628576	1	€ -	€ -	€ -	€ -	Technische Unie
Draad naar knel fitting (MCV)	VSH MES KOPP RE 22X1/2 BUJ (BSPP, G)	1120229	2	€ -	€ -	€ -	€ -	Technische Unie
Draad naar knel fitting (MCV) (2x STAD; 4x	VSH MES KOPP RE 22X1/2COBU	2599280	6	€ -	€ -	€ -	€ -	Technische Unie
Knel T-stuk DN15	VSH MES T- 15X15X15 3KXN	1121201	2	€ -	€ -	€ -	€ -	Technische Unie
Draad x knel DN15 fitting	VSH MES KOPP RE 15X1/2 COBU	1120211	1	€ -	€ -	€ -	€ -	Technische Unie
Kruisstuk DN20	VSH MES KRUIS 4X2 KN	1121714	1	€ -	€ -	€ -	€ -	Technische Unie
Watermeterkoppeling	RAM WATMTRKP 2DLG DN20 1X22 (6x pomp; 8x EMV)	1960311	14	€ -	€ -	€ -	€ -	Technische Unie
Verloopping voor drukmeter	SPRI 6KT VRL BU/BIDR 1/2X1/4	7581715	3	€ -	€ -	€ -	€ -	Technische Unie
Dop fitting CV	SPRI 6INDVAP 6-KNT BIDR 1	7581897	1	€ -	€ -	€ -	€ -	Technische Unie
T-stuk met draad voor PG en AV	VSH MES T- 22X1/2X22 KXNB1 L	1121557	4	€ -	€ -	€ -	€ -	Technische Unie
Sok Manifold	VSH SOK 1"	2594166	2	€ -	€ -	€ -	€ -	Technische Unie
4x puntstuk kogelkraan + 4x verloop FM	VSH MES KOPP RE 22X3/4 COBU	1120278	8	€ -	€ -	€ -	€ -	Technische Unie
4x verloop FM	SPRI RSOX VERL BIDR 3/4X1/2	7582464	4	€ -	€ -	€ -	€ -	Technische Unie
2x extra vlotter ontluchter	FLAM FLEXVENT VLOTONTL1/2" BU	1634419	2	€ 10,86	€ 13,14	€ 21,72	€ 26,28	Technische Unie
Overstort Ventiel + PG + vul/drain	FLAM PRESOCFILLER 1/2 (BSPP draad)	1800630	1	€ 31,27	€ 37,84	€ 31,27	€ 37,84	Technische Unie
Extra drukmeter na pomp	EURO MANOMETER 63MM 1/4 ACHTER	855312	1	€ 8,45	€ 10,22	€ 8,45	€ 10,22	Technische Unie
2 extra kogelkranen	CIMB KOGELKRAAN 3/4 C14	6736649	2	€ 7,87	€ 9,52	€ 15,74	€ 19,05	Technische Unie
Verloopstuk 22x15 Knel	VSH MES VERLOOPSTUK 22X15MM (2 stuks + 4 reserve)	2378933	6	€ 3,10	€ 3,75	€ 18,60	€ 22,51	Technische Unie
Pakking flowmeter	BEER FLNSAFD HD DN15 PN6 (4 + 6 reserve)	2054657	10	€ 0,29	€ 0,35	€ 2,90	€ 3,51	Technische Unie
Pakking flowmeter	BEER FLNSAFD HD DN15 PN10-40	2054065	10	€ 0,65	€ 0,79	€ 6,50	€ 7,87	Technische Unie

Figure M.2: Bill of materials (Part 2)

APPENDIX M. BILL OF MATERIALS

Pakking Pomp	BEER FLNSAFD HD DN10 PN6	2054255	10	€ 0,25	€ 0,30	€ 2,50	€ 3,03	Technische Unie
Aansluiting expansievat DN15 3/4X15	VSH MES KOPP RE 15X3/4 BI	1120492	1	€ 8,18	€ 9,90	€ 8,18	€ 9,90	Technische Unie
Verloop voor 1,5" T-stuk (1,5" naar 1")	SPRI NIPVERLBKT BUDR 1.1/2X1	7582905	1	€ 4,45	€ 5,38	€ 4,45	€ 5,38	Technische Unie
Draad 1" naar Knei koppeling	VSH MES KOPP RE 22X1 BI L	1120534	1	€ 8,09	€ 9,79	€ 8,09	€ 9,79	Technische Unie
Flexibele slang	REH RAUFILAM-E 19/3,5 RO25	9035605	1	€ 52,03	€ 62,96	€ 52,03	€ 62,96	Technische Unie
Isolatie flexibele slang	THFL ISOLATIE ECO 28X 9 LG2	1553924	13	€ 1,46	€ 1,77	€ 18,98	€ 22,97	Technische Unie
Knei naar binnendraad radiator koppeling	VSH MES KOPP RE 22X3/4 BI L	1120526	6	€ 6,36	€ 7,70	€ 38,16	€ 46,17	Technische Unie
Radiator koppeling	CMAF NIK RADKOPP 3/4 RE 3DLG	1773365	10	€ 6,09	€ 7,37	€ 60,90	€ 73,69	Technische Unie
Slangpijlaren	VSH SLANGPIJLAAR 3/4" BUI	6346464	10	€ 6,70	€ 8,11	€ 67,00	€ 81,07	Technische Unie
Slangklemmen	SLANGKLEM 19-28MM/9MM	3901956	20	€ 1,01	€ 1,22	€ 20,20	€ 24,44	Technische Unie
Reserve knelringen	VSH MES KNELRING 22MM	1122340	6	€ 1,33	€ 1,61	€ 7,98	€ 9,66	Technische Unie
Knei naar draad Prescofiller	VSH MES KOPP RE 15X1/2 BI	1120468	1	€ 3,89	€ 4,71	€ 3,89	€ 4,71	Technische Unie
Verloopring voor SPECTITE TC doorvoer	VSH VERLOOPRING 3/2" X1	2598316	1	€ 14,57	€ 17,63	€ 14,57	€ 17,63	Technische Unie
Verloopring voor SPECTITE TC doorvoer	VSH VERLOOPRING 1" X3/4" CHR	6927172	1	€ 5,90	€ 7,14	€ 5,90	€ 7,14	Technische Unie
Bocht knei - binnendraad, voor PG	VSH MES KNEIKOPP 22X1/2 BI L	1121045	1	€ 10,07	€ 12,18	€ 10,07	€ 12,18	Technische Unie
Bochtstuk 2x knei	VSH MES KNEIE 22X22 2XKN	1120740	6	€ 7,31	€ 8,85	€ 43,86	€ 53,07	Technische Unie
Knei - draad voor drain	VSH MES KOPP RE 22X1/2 BI L	1120484	1	€ 5,83	€ 7,05	€ 5,83	€ 7,05	Technische Unie
Sok 1/2" prescofiller	VSH DRAADFITZ SOK 1/2 DZR	1875313	1	€ 2,95	€ 3,57	€ 2,95	€ 3,57	Technische Unie
Verloop sok voor prescofiller	VSH VERLOOPSOK 3/4" X1/2"	6925309	1	€ 6,09	€ 7,37	€ 6,09	€ 7,37	Technische Unie
Verloopring voor SPECTITE TC doorvoer	VSH VERLOOPRING 1" X3/4"	6925408	1	€ 4,61	€ 5,58	€ 4,61	€ 5,58	Technische Unie
Verloopring voor SPECTITE TC doorvoer	VSH VERLOOPRING 3/2" X1	2598316	1	€ 14,57	€ 17,63	€ 14,57	€ 17,63	Technische Unie
T-stuk 3x binnendraad	VSH T-STUK 1/2"	6925044	2	€ 7,99	€ 9,67	€ 15,98	€ 19,34	Technische Unie
Kogelkraan 2x binnendraad 1/2"	CMAF KOGELKRAAN BIXBI 1/2" 640	4805723	2	€ 4,17	€ 5,05	€ 8,34	€ 10,09	Technische Unie
Dubbele nipple	VSH DUBBELE NIPPEL 1/2" DZR	1875369	2	€ 2,31	€ 2,80	€ 4,62	€ 5,59	Technische Unie
Verloopnippel	VSH VERLOOPNIPPEL 3/4" X1/2"	6924967	2	€ 3,81	€ 4,61	€ 7,62	€ 9,22	Technische Unie
Bocht 2x binnendraad	VSH KNEIE 3/4" BINXBIN	6925481	2	€ 9,16	€ 11,08	€ 18,32	€ 22,17	Technische Unie
T stuk DN15 met 1/2" BI draad	VSH MES T- 15X1/2X15 KXNB1 L	1121532	2	€ 7,36	€ 8,91	€ 14,72	€ 17,81	Technische Unie
vlotter ontzuchter, voor bypass solar collect	FLAM FLEXVENT VLOTONTL1/2" BU	1634419	1	€ 10,86	€ 13,14	€ 10,86	€ 13,14	Technische Unie
Verloopring	VSH VERLOOPRING 3/4" X1/2"	6925390	8	€ 2,49	€ 3,01	€ 19,92	€ 24,10	Technische Unie
Buisisolatie	ARST ARMAFLEX HT 10/35 LG2	6534192	2	€ 10,04	€ 12,15	€ 20,08	€ 24,30	Technische Unie
T-stuk isolatie	THFL PREF T-STUK 35MM	7328400	14	€ 1,71	€ 2,07	€ 23,94	€ 28,97	Technische Unie
Bocht isolatie	THFL PREF BOCHT90GR 4SEGM 35MM	7328393	1	€ 1,92	€ 2,32	€ 1,92	€ 2,32	Technische Unie
Bocht isolatie	THFL PREF BOCHT90GR 2SEGM 35MM	7328386	9	€ 1,21	€ 1,46	€ 10,89	€ 13,18	Technische Unie
Tank	PR-2 350st	PR-2 350st	1	€ 650,00	€ 773,50	€ 650,00	€ 773,50	TWL
Isolatie tank	Iso-B 350st	Iso-B 350st	1	€ 275,00	€ 327,25	€ 275,00	€ 327,25	TWL
Vracht vervoer	Vervoer incl toeslag Nederland	-	1	€ 87,00	€ 103,53	€ 87,00	€ 103,53	TWL
Heaters	EH3000 (3 kW; 230 V)	EH 3000	2	€ 98,00	€ 116,62	€ 196,00	€ 233,24	TWL
Isolatie hydraulie sep	?	-	1	€ -	€ -	€ -	€ -	Voorraad Tue
Uncertainty budget			1	€ 250,00	€ 302,50	€ 250,00	€ 302,50	
		Subtotaal				€ 14.882,08	€ 17.998,16	
		Totaal	774			€ 14.882,08	€ 17.998,16	
		Budget				€ 15.000,00	€ 18.000,00	

Figure M.3: Bill of materials (Part 3)



# Bibliography

- [1] Normcommissie 349010 'Zonnewarmte'. *Zonne-energie - Thermische zonnecollectoren - Beproevingsmethoden (ISO 9806:2017, IDT)*. Tech. rep. Koninklijk Nederlands Normalisatie-instituut, 2017.
- [2] Devanahalli G. Prabhanjan et al. "Natural convection heat transfer from helical coiled tubes". In: *International Journal of Thermal Sciences* 43 (2004), pp. 359–365.
- [3] E. Matehioulakis et al. "Assessment of uncertainty in solar collector modeling and testing". In: *Solar Energy* 66.5 (1999), pp. 337–347.
- [4] Fernández-Seara J et al. *Thermal analysis of a helically coiled tube in a domestic hot water storage tank*. 2007.
- [5] Kratzenberg et al. *Uncertainty calculations in pyranometer measurements and application*. 2006.
- [6] S. Fischer et al. "Collector test method under quasi-dynamic conditions according to the European Standard EN 12975-2". In: *Solar Energy* 76 (2004), pp. 117–123.
- [7] VDI-Gesellschaft Verfahrenstechnik und Chemieingenieurwesen. *VDI Heat Atlas*. Springer, 2010, p. 1057.
- [8] Dorota Chwieduk. *Solar Energy in Buildings: Thermal Balance for Efficient Heating and Cooling*. Elsevier Science, 2014.
- [9] R.B. Degenhart. *Optical efficiency of an Evacuated Tube Solar Collector under varying operating conditions*. 2020.
- [10] M.A. van Duijnhoven. *Solar combisystem with Thermo-Differential Valve*. 2018.
- [11] J.K. Nayak E.H. Amer. "Experimental and theoretical evaluation of dynamic test procedures for solar flat-plate collectors". In: *Solar Energy* 69 (2000), pp. 377–401.
- [12] J.K. Nayak et al. E.H. Amer. "A new dynamic method for testing solar flat-plate collectors under variable weather". In: *Energy Conversion and Management* 40 (1999), pp. 803–823.
- [13] *Evacuated Tube Solar Collectors*. [http://www.apricus.com/html/solar\\_collector.htm#.XR9qPegzaU1..](http://www.apricus.com/html/solar_collector.htm#.XR9qPegzaU1..) Accessed: 2019-07-05.
- [14] H. Abdib F. Jafarkazemia. "Evacuated tube solar heat pipe collector model and associated tests". In: *Renewable and Sustainable Energy* 4 (2012).
- [15] M.M.M.M. van den Heuvel. *Thermal and electric efficiency of PVT collectors*. 2018.
- [16] National Instruments. *Datasheet NI 9212 and TB-9212*. 2019.
- [17] A. C. Oliveira J. Facão. "Analysis of a plate heat pipe solar collector". In: *International Journal of Low-Carbon Technologies* 1 (2006), pp. 1–9.
- [18] W. Spirkel J. Muschaweck. "Dynamic solar collector performance testing". In: *Solar Energy Materials and Solar Cells* 30 (1993), pp. 95–105.
- [19] M. Jiang. *Simulation results in typical spring days*. 2020.
- [20] William A. Beckman John A. Duffie. *Solar Engineering of Thermal Processes*. John Wiley and Sons, 2013.
- [21] Soteris A. Kalogirou. *Solar Energy Engineering Processes and Systems*. Elsevier, 2014.
- [22] KROHNE. *IFC 100 Technical Datasheet*. 2020.
- [23] KROHNE. *OPTIFLUX 4000 Technical Datasheet*. 2014.
- [24] Zhifeng Wang et al. Li Xu. "A new dynamic test method for thermal performance of all-glass evacuated solar air collectors". In: *Solar Energy* 86 (2012), pp. 1222–1231.
- [25] Osama Elsamni Mahmoud B. Elsheniti Amr Kotb. "Thermal performance of a heat-pipe evacuated-tube solar collector at high inlet temperatures". In: *Applied Thermal Engineering* 154 (2019), pp. 315–325.
- [26] *Propagation of Errors—Basic Rules*. [https://courses.washington.edu/phys431/propagation\\_errors\\_UCh.pdf](https://courses.washington.edu/phys431/propagation_errors_UCh.pdf). Accessed: 2021-01-06.
- [27] Volker Quaschnig. *Understanding Renewable Energy Systems*. Routledge, 2016.

- [28] Nico van Ruth. *PPT Direct Multi-Pass Solar XL-system, using the Thermo-Differential Valve*. 2017.
- [29] W. Spirkel. “Dynamic solar domestic hot water testing”. In: *Journal of Solar Energy Engineering* 112 (1990).
- [30] *Type T Thermocouple Reference Table*. <https://www.thermocoupleinfo.com/type-t-thermocouple.htm>. Accessed: 2021-02-03.
- [31] Bengt Perers et al. Weiqiang Kong Zhifeng Wang. “Investigation of thermal performance of flat plate and evacuated tubular solar collectors according to a new dynamic test method”. In: *Energy Procedia* 30 (2012), pp. 152–161.
- [32] Xing Li et al. Weiqiang Kong Zhifeng Wang. “Thermal performance of a heat-pipe evacuated-tube solar collector at high inlet temperatures”. In: *Solar Energy* 86 (2012), pp. 398–406.
- [33] ISO Working group consisting of experts nominated by the BIPM IEC and OIML. *Guide to the expression of uncertainty in measurement (GUM:1995)*. 2008.
- [34] Kipp & Zonen. *Instruction manual CM11 and CM14 pyranometer / albedometer, version 0805*. 2021.

## Declaration concerning the TU/e Code of Scientific Conduct for the Master's thesis

I have read the TU/e Code of Scientific Conduct<sup>1</sup>.

I hereby declare that my Master's thesis has been carried out in accordance with the rules of the TU/e Code of Scientific Conduct

Date

26-02-2021


Name

Pim van Delft

ID-number

0819192

Signature



*Submit the signed declaration to the student administration of your department.*

<sup>1</sup> See: <https://www.tue.nl/en/our-university/about-the-university/organization/integrity/scientific-integrity/>

The Netherlands Code of Conduct for Scientific Integrity, endorsed by 6 umbrella organizations, including the VSNU, can be found here also. More information about scientific integrity is published on the websites of TU/e and VSNU